



저작자표시-비영리-변경금지 2.0 대한민국

이용자는 아래의 조건을 따르는 경우에 한하여 자유롭게

- 이 저작물을 복제, 배포, 전송, 전시, 공연 및 방송할 수 있습니다.

다음과 같은 조건을 따라야 합니다:



저작자표시. 귀하는 원저작자를 표시하여야 합니다.



비영리. 귀하는 이 저작물을 영리 목적으로 이용할 수 없습니다.



변경금지. 귀하는 이 저작물을 개작, 변형 또는 가공할 수 없습니다.

- 귀하는, 이 저작물의 재이용이나 배포의 경우, 이 저작물에 적용된 이용허락조건을 명확하게 나타내어야 합니다.
- 저작권자로부터 별도의 허가를 받으면 이러한 조건들은 적용되지 않습니다.

저작권법에 따른 이용자의 권리는 위의 내용에 의하여 영향을 받지 않습니다.

이것은 [이용허락규약\(Legal Code\)](#)을 이해하기 쉽게 요약한 것입니다.

[Disclaimer](#)

Ph.D. Dissertation of Engineering

**High-resolution Portable Microscope
for *in situ* Real-time Monitoring of
Stomata and other Biological & Non-
biological Applications**

**기공의 현장 실시간 모니터링과 기타 생물학적,
비생물학적 응용을 위한 고해상도 휴대용 현미경**

August 2019

**Graduate School of Engineering
Seoul National University
Mechanical and Aerospace Engineering**

Prashant Purwar

Abstract

High-resolution Portable Microscope for *in situ* Real-time Monitoring of Stomata and other Biological & Non- biological Applications

Prashant Purwar

Department of Mechanical and Aerospace Engineering

Seoul National University

Commercial high-resolution optical microscopes are essential for microscopy imaging; however, they are expensive and bulky, which limits their use in point-of-care devices, resource-limited areas, and real-time imaging of a sample in a large apparatus. In this study, we report a novel compact lightweight submicron-resolution reflected and inverted optical microscope at low cost. Our technique utilizes the proximity of the image sensor to a commercial microscope objective lens for compactness of the microscope. The use of an image sensor with a small pixel size helps to reduce the information loss, which provides high-resolution images. Moreover, our technique offers a freedom to tailor the design of microscope according to the required resolution, cost, and portability for specific applications, which makes it a suitable candidate for affordable point-of-care devices.

Unlike conventional reflected microscope, which consists of downward facing objective lens, our portable reflected microscope is designed with upward facing objective lens. Such configuration with high-resolution imaging capability and portability makes it suitable for imaging of abaxial (lower side) surface of a plant leaf. Stoma, functionally specialized micrometer-sized pores on the epidermis of leaves (mainly on the lower epidermis) were observed and analyzed. Since stomata control the flow of gases and water between the interior of the plant and atmosphere, real-time monitoring of stomatal dynamics can be used for predicting the plant hydraulics, photosensitivity, and gas exchanges effectively. To date, several techniques offer the direct or indirect measurement of stomatal dynamics, yet none offer real-time, long-term persistent measurement of multiple stomal apertures simultaneously of an intact leaf in a field under natural conditions. Our technique is capable of analyzing and quantifying the multiple lower epidermis stomal pore dynamics simultaneously and does not require any physical or chemical manipulation of a leaf. An upward facing objective lens in our portable microscope allows the imaging of lower epidermis stomatal opening of a leaf while upper epidermis being exposed to the natural environment. Small depth of field ($\sim 1.3 \mu\text{m}$) of a high-magnifying objection lens assists in focusing the stomatal plane in highly non-planar tomato leaf having a high density of trichome (hair-like structures). For long-term monitoring, the leaf is fixed mechanically by a novel designed leaf holder providing freedom to expose the upper epidermis to the sunlight and lower epidermis to the wind simultaneously. In our study, a direct relation between the stomatal opening and the intensity of sunlight illuminating on the

upper epidermis has been observed in real-time. In addition, real-time porosity of leaf (ratio between the areas of stomatal opening to the area of a leaf) and stomatal aspect ratio (ratio between the major axis and minor axis of stomatal opening) along with stomatal density have been quantified. Therefore, this portable and inexpensive microscopeic technique provides the essential functionalities of a bulky expensive high-performance microscope along with the specific applications at a lower cost. Images of several micron-to-submicron scale patterns and spherical beads are acquired to observe the resolution and quality of the images obtained using our microscope. In addition, we demonstrate the applications of our microscope in various fields such as recording of high-speed water microdroplet formation inside a microfluidic device, high-resolution live cell imaging inside an incubator, and real-time imaging of crack propagation in a sample under stretching by a material testing system (MTS).

Keywords: optical microscopy, portable high-resolution microscope, inverted microscope, reflected microscope, microfluidics, real-time imaging, cell imaging, stomata imaging.

Student Number: 2010-31319

Contents

Abstract	iii
Contents	vi
List of Tables	ix
List of Figures	x
Abbreviations	xiii
Chapter 1 Introduction	1
1.1 High-resolution portable microscope and in-situ real-time stomata imaging	1
1.2 Research objective and contributions	4
1.3 Research overview	6
Chapter 2 Development of high-resolution portable reflected optical microscope for in situ real-time stomata monitoring	8
2.1 Literature survey	8
2.2 Experimental setup and portable high-resolution microscope.....	20
2.3 Tomato plant cultivation.....	22
2.4 Measurement of light intensity.....	23
2.5 Imaging of micrometer-sized object by portable reflected microscope.....	24
2.6 Measurement of optical resolution	26

2.7	Tomato leaf surface profile.....	28
2.8	A need of reflected microscope with koehler illumination (vertical illumination) for in-situ stomata imaging	31
2.9	Leaf holder	35
2.9.1	Requirement of a leaf holder	35
2.9.2	Design and fabrication of leaf holder	36
2.10	Effect of tilted stomata on quantification of stomatal opening area (or, pore area); a cosine effect.....	42
2.11	Real-time in-situ stoma imaging, monitoring and effect of sunlight intensity	45
2.12	Stomata mapping of a plant.....	49
2.13	Quantification of stomatal density and changes in stomatal geometrical features in response to the sunlight intensity	52
	Bibliography	62

Chapter 3 Design and Development of High-resolution

Portable Inverted Optical Microscope.....67

3.1	Optical microscope	67
3.2	Literature survey	68
3.3	Portable inverted microscope	76
3.3.1	Design and development	76
3.3.2	Optical resolution	78
3.3.3	Imaging of a micrometer object and image enhancement	82
3.3.4	Effect of pixel size (of image sensor) on image quality and point spread function (PSF)	90

3.4 Applications of portable inverted microscope.....	92
3.4.1 Sub-micrometer scale imaging	92
3.4.2 High-speed microscopy: imaging of high-speed droplets generation	97
3.4.3 Live imaging of eukaryotic cells	100
3.4.4 Industrial applications: high-resolution real-time monitoring of a sample at a bulky apparatus	104
3.4.5 Industrial applications: optical inspection of micro patterns fabricated in a clean room.....	108
Bibliography	112
Chapter 4 Conclusion.....	115
Bibliography	120

List of Tables

Table 2-1 Comparison of stomata pore imaging and/or monitoring techniques.....	19
Table 3-1 Comparison of portable inverted microscopes.....	75
Table 3-2 Specifications of image sensors used in experiment.....	77
Table 3-3 Half-pitch spatial resolution (HSR), full-pitch spatial resolution (FSR) and field of view (FOV) of microscopic setup observed under various combinations of the image sensors, objective lens and light sources.....	81
Table 4-1 Comparison of stomata pore imaging and/or monitoring techniques.....	118
Table 4-2 Comparison of portable inverted microscopes.....	119

List of Figures

Fig. 2-1 Schematic of opening and closing of the stomata.....	10
Fig. 2-2 Indirect methods of measurement of stomatal aperture or sensing the opening and closing information.....	15
Fig. 2-3 Direct methods of measurement of stomatal aperture of a leaf	17
Fig. 2-4 Experimental setup of real-time in-situ stomata imaging and monitoring in a field.....	21
Fig. 2-5 Tomato plant cultivation in transparent vinyl film covered greenhouse situated at Gwanak district at Seoul.....	22
Fig. 2-6 Measurement of sunlight intensity.....	23
Fig. 2-7 Microscale imaging by portable reflected microscope.....	26
Fig. 2-8 Measurement of optical resolution of portable reflected microscope in term of half-pitch spatial resolution (HSR) value	27
Fig. 2-9 Surface profile measurement and electron microscopy of tomato and lily leaf.....	30
Fig. 2-10 Stomata imaging by compact transmitted and reflected microscopes in laboratory and field environment.....	33
Fig. 2-11 Different types of reflected light illumination sources such as 'Near-vertical illumination, tungsten illumination, oblique illumination and highly oblique illumination, diffuse illumination etc. used in reflected microscope.....	34
Fig. 2-12 Schematic of an upper (adaxial) and lower (abaxial) surface of a leaf and a commercial leaf holder.....	36
Fig. 2-13 Leaf holder: a device to hold and stabilize the leaf for long-term	

stomata imaging	39
Fig. 2-14 Designing and fabrication of lower leaf holder	41
Fig. 2-15 Effect of tilted stomata on quantification of stomatal opening area	44
Fig. 2-16 Real-time field monitoring of tomato stoma in sunlight.....	48
Fig. 2-17 Stomata mapping of leaves	51
Fig. 2-18 Quantification of stomatal density of four-week-old tomato plant intact leaf under sunlight in a field.....	53
Fig. 2-19 Stoma opening status and measurement of geometrical features of stomata	56
Fig. 2-20 Average stomatal opening, total stomatal opening and average aspect ratio of a leaf	57
Fig. 3-1 Conventional inverted microscope	70
Fig. 3-2 Lens-free-imaging-based portable microscopes	71
Fig. 3-3 Lens-based portable microscope.....	74
Fig. 3-4 Schematic, experimental setup, and dimension comparison of portable inverted microscope.	77
Fig. 3-5 Measurement of optical resolution and field of view (FOV) values for the microscopic setups.....	80
Fig. 3-6 Imaging of a microscale grid pattern. Comparison of the image qualities of portable microscope with a similar FOV of Nikon microscope.	83
Fig. 3-7 Multiple-images-fusion-based image enhancement	85
Fig. 3-8 Single-image-based image enhancement.....	89
Fig. 3-9 Effect of pixel size and point spread function	91
Fig. 3-10 Sub-micrometer scale imaging of polystyrene beads (920 nm,	

460 nm and 380 nm) by portable microscope	93
Fig. 3-11 Sub-micrometer scale imaging of nanoscale grooves on a PET film	95
Fig. 3-12 Sub-micrometer scale imaging of monolayer bacterial colony grown for a hour	97
Fig. 3-13 High-speed microscopy. microfluidic application: imaging of water droplet generation in oil	99
Fig. 3-14 Live cell imaging by portable microscope inside the incubator.	103
Fig. 3-15 Imaging of crack propagation in a sample on bulky apparatus by portable microscope	106
Fig. 3-16 Crack propagation analysis in the rGO film attached on PDMS	107
Fig. 3-17 Optical inspection of fabricated micro-patterns and slope measurement at edge by a portable microscope.....	110

Abbreviations

CAD	Computer-aided design
CI	Circularity index
CL	Cloud
DIW	Deionized water
DWT	Discrete wavelet transform
E. coli	Escherichia coli
FESEM	Field-emission scanning electron microscope
FOV	Field of view
FSR	Full-pitch spatial resolution
HSR	Half-pitch spatial resolution
ITO	Indium titanium oxide
LED	Light emitting diode
MTS	Material testing system
NA	Numerical aperture
OM	Optical Magnification
OR	Optical resolution
PDMS	Polydimethylsiloxane
PET	polyethylene terephthalate
PLA	Polylactic acid
PR	Photo resist
PS	Polystyrene particle
PSF	Point spread function
rGO	Reduced graphene oxide
SEM	Scanning electron microscope
SLI	Sunlight intensity

Chapter 1

Introduction

1.1. High-resolution portable microscopy and in-situ real-time stomata imaging

High-resolution optical imaging by complex optical microscopes is one of the essential techniques for experimental analyses without damaging the sample. These microscopes use visible light (400-780 nm) and a complex system of lenses to magnify images of small objects. Broadly, optical microscopes are categorized as transmitted and reflected microscopes. In transmitted microscope, light rays from the light source falls on the object and light transmitted from the object is captured by image sensor or photographic plate after magnification through the complex system of optical lens. Hence, for transparent object, transmitted microscope are suitable. On the other hand, in reflected microscope the light rays from the light source falls on the object and light reflected from the object is captured by image sensor or photographic plate after magnification through the complex system of optical. Hence, for opaque or semi-transparent objects, reflected microscopes are suitable. Moreover, reflected microscopes provide the

surface information of an object.

High-performance standard optical microscopes can be used to obtain high-quality images; however, these microscopes are expensive, bulky, and limited by the small field of view. Moreover, owing to portability and cost issues, these microscopes are not suitable for several applications such as point-of-care devices, direct imaging of a sample in a large apparatus, remote location applications, resource limited areas, etc. In recent years, there has been a progress in the development of cost-effective and portable microscopes; however, most of these methods are limited by the sample conditions, requirement of a complex computation to obtain the final image of an object, expensive optical system, sample cleanliness, specific uses, technology to fabricate the device, conventional design, portability and cost. Digital in-line holography, contact imaging microscopy, and optofluidic microscopy, origami-based paper microscope and smartphone-based microscope are good examples of these lens-free-imaging and lens-based portable transmitted and reflected microscopes.

In addition to high-resolution microscopy in laboratory environment, a microscopy of living being such as plants or plant tissue/cells in natural environment is a challenging task. Stomata,

functional pores at the epidermis of the leaf, are one of the important plant tissue, which regulate the gaseous exchange during growth processes by controlling the aperture of stomatal opening. To date, several techniques offer the direct or indirect measurement of stomatal aperture or opening/closing information of stomatal pores. Porometer, plasmolysis technique, electro-mechanical sensor, infrared thermography, mold impression are examples of direct or indirect technique for stomata observation, yet, none offer real-time, long-term persistent measurement of multiple stomal apertures simultaneously of an intact leaf in a field under natural conditions.

In this study, we demonstrate a novel simple technique for a cost-effective compact portable customizable submicron-resolution transmitted and reflected light microscope and its applications in various fields. This technique can be customized for specific applications such as *in situ* real-time field imaging and monitoring of stomata at a single stoma level analysis, high-speed microscopic imaging, live cell monitoring inside an incubator, real-time monitoring of the effect of physical forces on a sample in a large apparatus, micro-to-nanoscale measurement and inspection of a sample at industrial processes etc. In case of *in situ* real-time field imaging of stomata, our

technique does not require any physical or chemical manipulation of a leaf. A novel leaf holder has been designed and fabricated to hold the leaf for long-term monitoring of stomata. Leaf holder allows exposing the upper epidermis to the sunlight and lower epidermis to the wind simultaneously, two major factors of stomatal conductance.

1.2 Research objectives and contributions

The primary objective of this study is to develop the high-resolution, portable, cost-effective and simple microscopes capable of imaging the objects under different conditions with high-resolution where conventional/other microscopic technique have several limitations. In this study, we have shown the development of simple, submicrometer-resolution (488 nm) transmitted and reflected microscopes.

Our microscopic technique utilizes the proximity of the image sensor to a commercial microscope objective lens for compactness of the microscope and does not use tube lens. Removal of tube lens in both type of microscopes brings down the size, weight, optical components and cost of the microscope. Moreover, the reduction of optical components reduces the optical attenuation of light reaching to the image sensor, which results in to a bright and contrast image of an object. To reduce the information loss and enhance the resolution of an object image, an image sensor with a small pixel size was used. Removal of tube lens and proximity of the image sensor to a commercial microscope objective lens

adds optical distortion in the final image of an object. Hence, multiple-image-fusion-based and single-image-based, image enhancement techniques are implemented to enhance the final image. The combinations of objective lens with various pixel-size-image-sensors were experimented for maximum possible field-of-view with high-resolution.

Unlike conventional reflected microscope, which consists of downward facing objective lens, we developed the portable reflected microscope having upward facing objective lens. Such configuration makes our microscope suitable for imaging of abaxial (lower side) stomata of a plant leaf. For long-term monitoring of stomata in field, the imaging area of leaf should be stable and parallel to the focus plane of the microscope. Hence, a novel leaf holder was designed to stabilize the leaf surface and to expose the upper epidermis of a leaf to the sunlight and lower epidermis to the wind simultaneously. In our study, a direct relation between the stomatal opening and the intensity of sunlight illuminating on the upper epidermis has been observed in real-time. In addition, real-time porosity of leaf (ratio between the areas of stomatal opening to the area of a leaf) and stomatal aspect ratio (ratio between the major axis and minor axis of stomatal opening) along with stomatal density have been quantified.

Further, the application of transmitted microscope in live cell imaging in controlled environment, high-speed imaging, submicrometer-scale imaging and industrial imaging has been studied. Together with

microscopy in closed environment, an application of reflected microscope in real-time plant imaging under natural environment in the field has been explored. We studied the in-situ stomata (micrometer pores on surface of a leaf) imaging and monitoring under natural condition which has not been possible until now due to unfavorable setup of conventional optical microscopes.

1.3 Research overview

The thesis is organized as follows. First, the present techniques of portable microscopy has been presented with their limitations. Next, a portable reflected microscope with upward facing objective lens has been developed for in-situ plant imaging. Real-time imaging and monitoring of stomata has been presented. A novel leaf-holder and deigned for long-term monitoring of stomata. Finally, a relation between on the sunlight-intensity falling on the leaf and stomata opening has been established.

Further, development of a transmitted microscopy has been proposed followed by experimental setup, image quality obtained by our microscope, optical resolution and image enhancement. Multiple-image-fusion-based and single-image based image enhancement were studied only in case of transmitted microscope. Due to the small field of view, the image enhancement was not required for reflected microscope. Applications of transmitted microscope has been explored in the field of

submicrometer-sized particles microscopy, live cell imaging, high-speed microscopy and industrial microscopy.

Chapter 2

Development of high-resolution portable reflected optical microscope for in situ real-time stomata monitoring

Contents

- 2.1 Introduction and literature survey
- 2.2 Experimental setup
- 2.3 Tomato plant cultivation
- 2.4 Measurement of sunlight intensity
- 2.5 Imaging of micrometer-sized object
- 2.6 Measurement of optical resolution
- 2.7 Tomato leaf surface profile
- 2.8 A need of reflected microscope with Koehler illumination (vertical illumination) for in-situ stomata imaging
- 2.9 Leaf holder
 - 2.9.1 Requirement of a leaf holder
 - 2.9.2 Design and fabrication of novel leaf holder
- 2.10 Real-time in situ stoma monitoring and effect of sunlight intensity
- 2.11 Stomata mapping of a plant
- 2.12 Quantification of stomatal density and changes in stomatal geometrical features in response to the sunlight intensity

2.1 Introduction and literature survey

Evolution and natural growth of plant life are based on the continuous spectrum of the sunlight (Chandrasekhar and Münch 1946, Hessen 2008, Hogewoning, Douwstra et al. 2010). Major plant growth processes such as transpiration, photosynthesis and respiration require a controlled gaseous

exchange between the interior of the plant and atmosphere. Stomata, functional pores found at the epidermis of the leaf, regulate this gaseous exchange during growth processes by controlling the aperture of stomatal opening (Hetherington and Woodward 2003). Stomatal opening is predominantly affected by sunlight intensity (SLI) falling on the upper epidermis of a leaf (Wild and Wolf 1980, Hogewoning, Douwstra et al. 2010). In favorable conditions of stomatal opening (e.g., high light intensity and high humidity), a proton pump drives protons (H^+) from the guard cells. This results the electrical potential of guard cells to be negative. Further, the negative potential of guard cells triggers the uptake of potassium ions (K^+) occurs. This increase in solute concentration lowers the water potential inside the cell, which results in the diffusion of water into the cell through osmosis. This increases the cell's volume and turgor pressure. Then, because of rings of cellulose microfibrils prevent the width of the guard cells from swelling, and thus only allow the extra turgor pressure to elongate the guard cells, whose ends are held firmly in place by surrounding epidermal, the two guard cells lengthen by bowing apart from one another, creating an open pore through which gas can move. (Gray and Peirce 1919, Hunt 2003, Meckel, Gall et al. 2007). A schematic of Guard cells swelling (stomal opening) and shrinking (Stomal closing) are shown in Fig. 2-1.

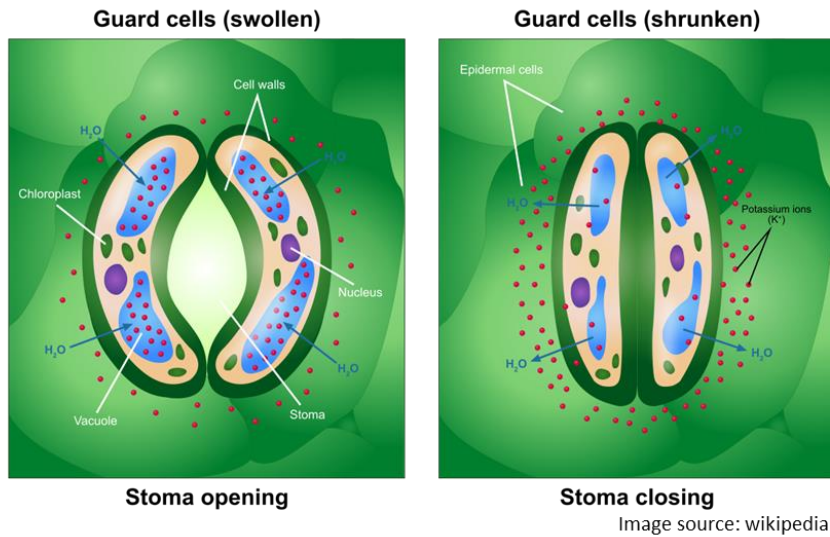


Fig 2-1. Schematic of opening and closing of the stomata

Changes in the status of stomatal aperture are determined by two major approaches: directly by measurement of the stomatal apertures and indirectly by measurement of leaf transpiration. To date, several techniques offer the direct or indirect measurement of stomatal aperture or opening/closing information of stomatal pores, yet none offer real-time, long-term persistent measurement of multiple stomatal apertures simultaneously of an intact leaf in a field under natural conditions (refer Fig. 2-2 and Fig. 2-3). Porometer, an instrument to measure the stomatal resistance (or conductance) against the gaseous exchange only provides the mean pore size of stomata (if stomatal density is known) and not suitable for long-term persistent stomatal monitoring since opaque leaf clips of a porometer restrict the exposure of

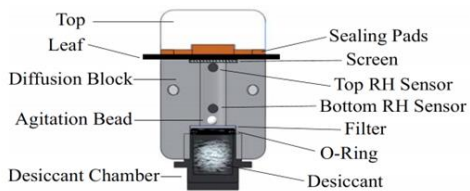
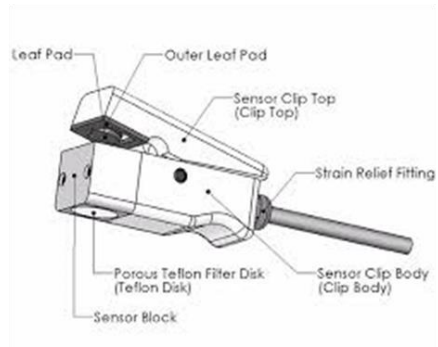
sunlight on upper epidermis of a leaf (Meidner and Mansfield 1968). Plasmolysis technique where an osmotic potential of guard cells indicates the open or closed status of stomata does not provide the true value of osmotic pressure of guard cells (Willmer and Beattie 1978). Electro-mechanical sensor based real-time monitoring of the stomatal function requires complicated fabrication of electrically conductive ink across a stoma under a microscope. Further, the fabrication of ink is difficult on highly non-planar leaves such as tomato leaf having a high density of hair-like structures. Moreover, the technique only provides the open or closed status information of a stoma (Koman, Lew et al. 2017). The use of infrared thermography for monitoring of stomatal conductance under natural environmental conditions are limited to the bulk analysis of stomata behavior and suffers for multiple limitations such as accuracy, thermal drift of imager, unreliable references for thermal indices etc. (Jones, Stoll et al. 2002, Grant, Chaves et al. 2006, Leinonen, Grant et al. 2006, Craparo, Steppe et al. 2017).

On the other hand, direct measurement mainly utilizes microscopic images of a detached leaf or imprints of an intact leaf, which often requires invasive manipulations (physical or chemical) of a leaf (Omasa and Onoe 1984, Pathan, Bond et al. 2010, Jayakody, Liu et al. 2017, Wu, Huang et al. 2017). Optical microscopy of abaxial stomata of an intact leaf by a conventional bulky reflected microscope requires 180 degrees folding of a leaf

to face the abaxial side towards the objective lens. Such folding often damages the leaf and restrict the upper epidermis exposing to the light source (Koman, Lew et al. 2017). Hence, conventional microscopes are not suitable for persistent field monitoring of stomata. Mold impression technique, which utilizes the permanent impression of stomata on silicon rubber, does not provide the accurate measurement of stomata and limited to the large size stomatal measurement (Smith, Weyers et al. 1989, Weyers and Meidner 1990, Willmer and Fricker 1996, Lawson, James et al. 1998). Fluorometric measurement of individual stomatal activity utilizes water-responsive UV treated polymer coating on the abaxial surface of the leaf. However, polymerization of a water-responsive polymer may damage the leaf. In addition, quantification of stomatal opening requires expensive optical and fluorescence microscopes (Higaki 2015, Eisele, Fäßler et al. 2016, Seo, Park et al. 2016).

Indirect methods of measurement of stomal aperture

Leaf Porometer



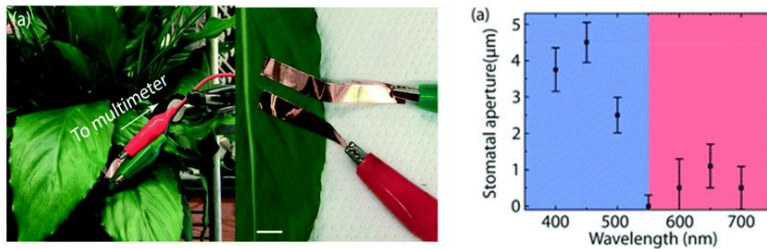
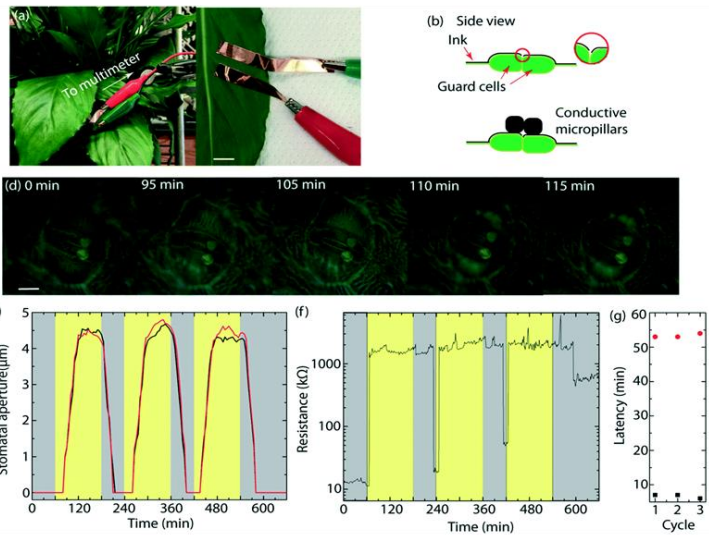
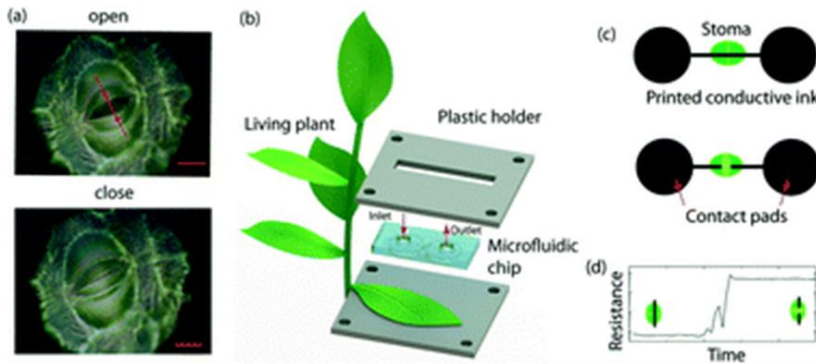
Sensor block and desiccant chamber components



DECAGON DEVICES, INC

Indirect methods of measurement of stomal aperture

Electro-mechanical sensor



Koman, Volodymyr B. et. al Lab on chip 2017

Indirect methods of measurement of stomal aperture

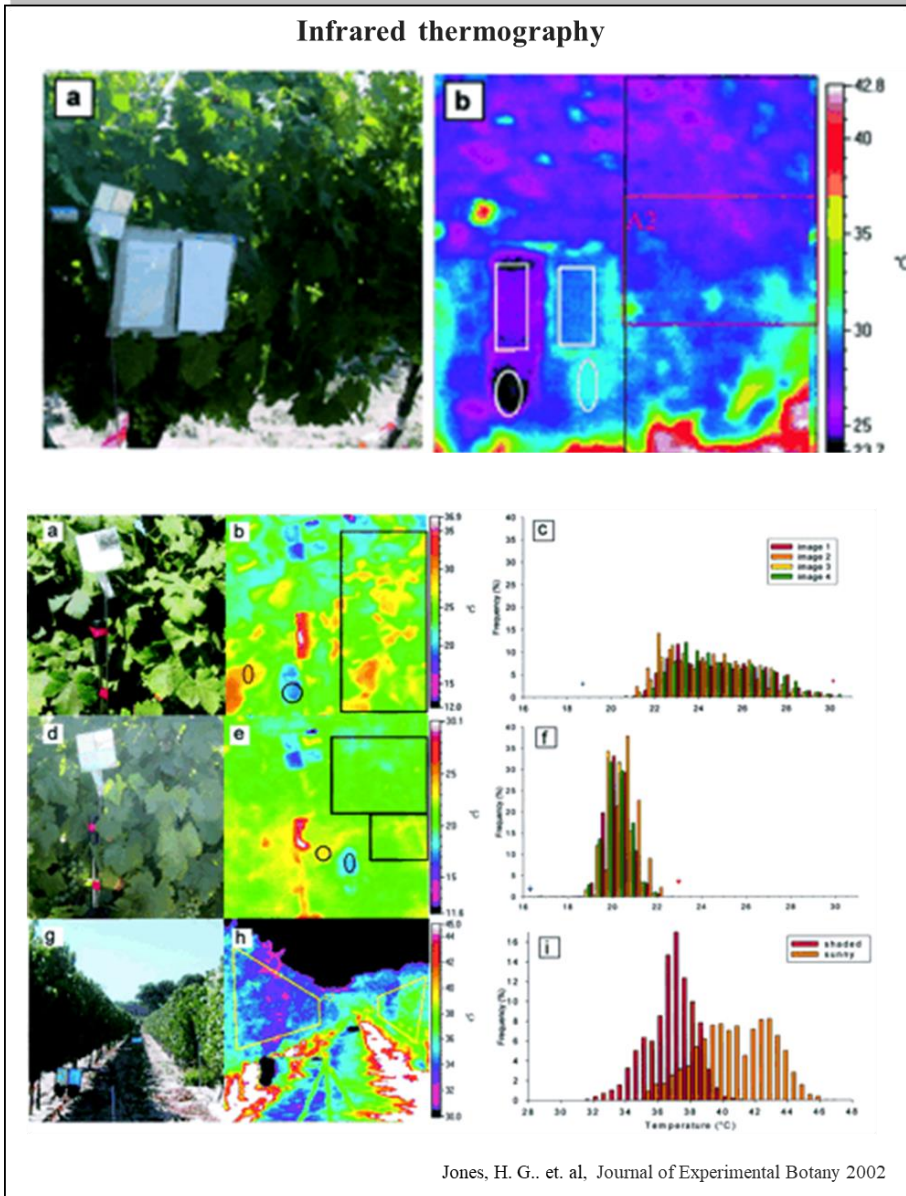
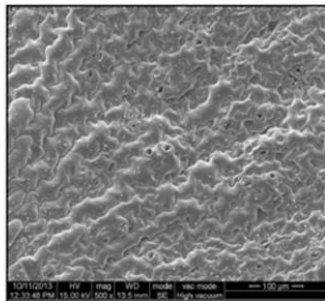
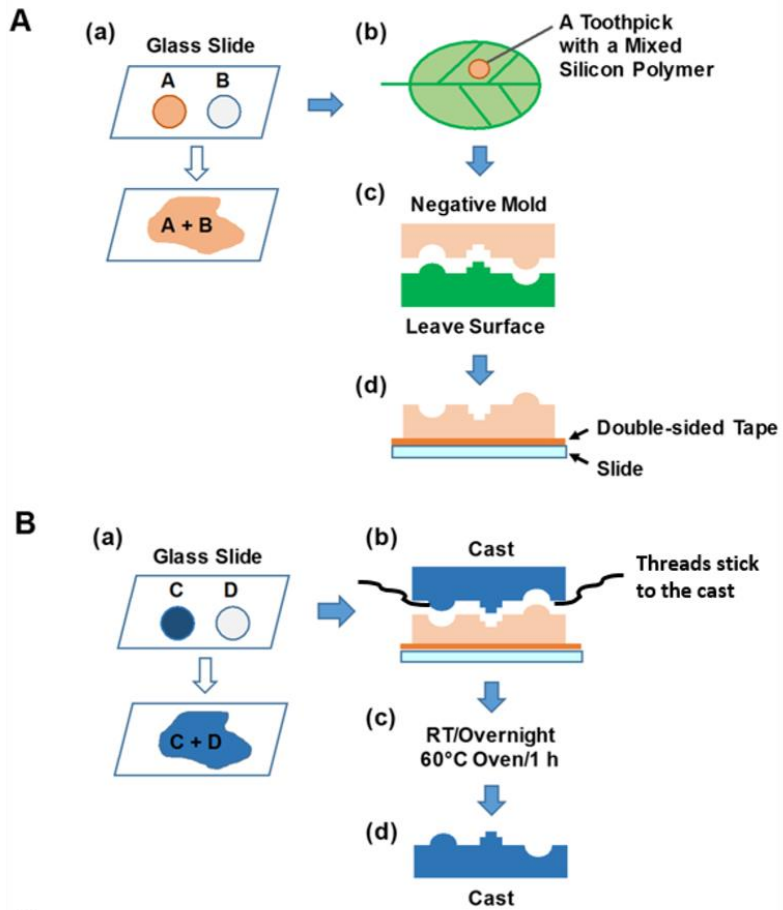


Fig. 2-2. Indirect methods of measurement of stomatal aperture or sensing the opening and closing information.

Direct methods of measurement of stomal aperture

Mod impression technique



Wu, Hui-Chen et. al, Bio protocol, 2017

Direct methods of measurement of stomatal aperture

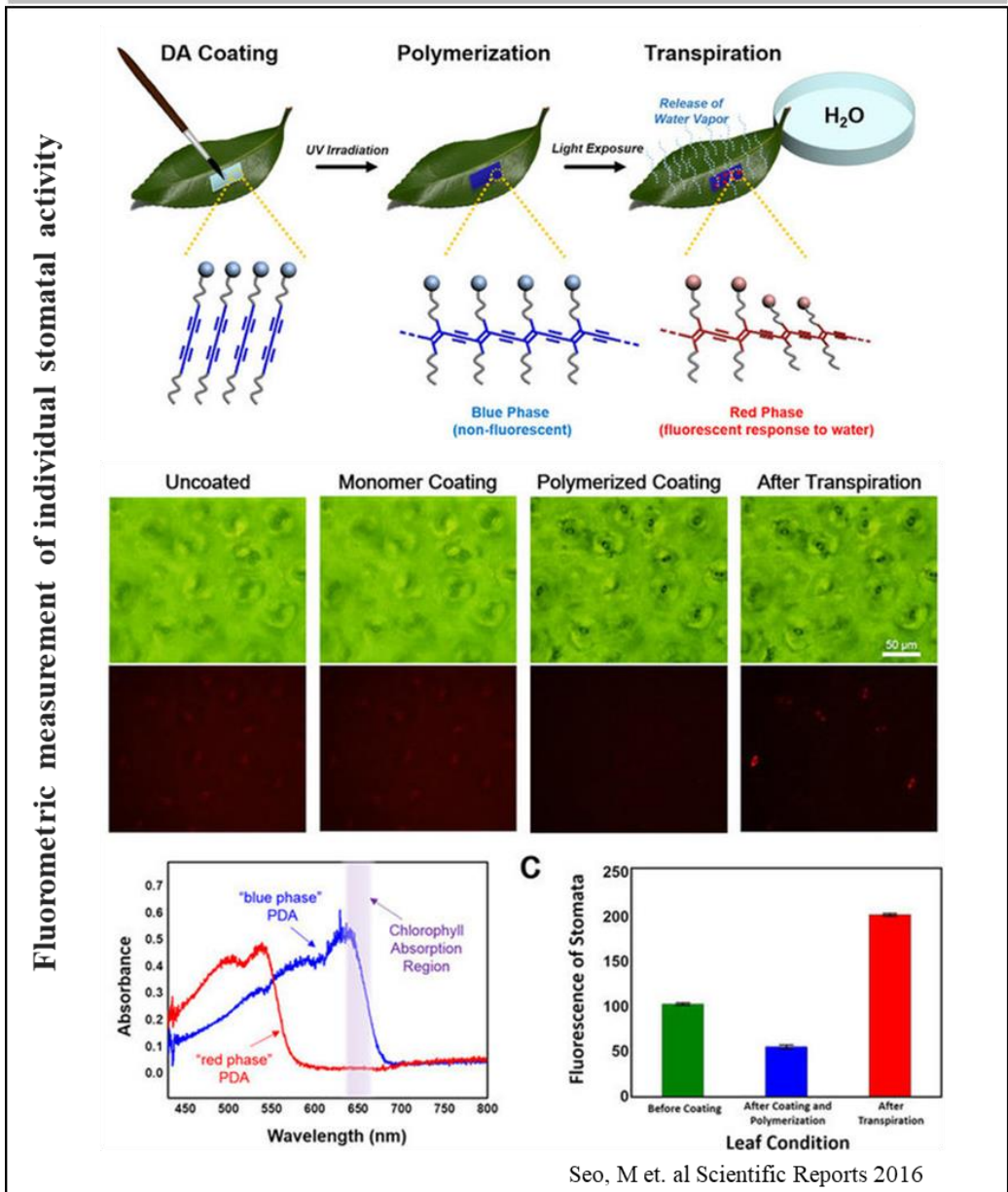


Fig. 2-3. Direct methods of measurement of stomatal aperture of a leaf.

Herein, we developed a portable high-resolution microscopy-based technique for *in situ* real-time field imaging and monitoring of stomata at a single stoma level analysis. Our technique is capable of analyzing and quantifying the multiple stomal pore dynamics simultaneously and does not require any manipulation of a leaf. An upward facing objective lens in our microscopic setup allows observing the lower epidermis of an intact leaf in its natural condition while exposing the upper epidermis to the sunlight. A novel leaf holder has been designed and fabricated to hold the leaf for long-term monitoring of stomata. Leaf holder allows exposing the upper epidermis to the sunlight and lower epidermis to the wind simultaneously, two major factors of stomatal conductance. Therefore, it is possible to have *in situ* direct real-time imaging and monitoring of stomata dynamics in plant leaf at field under natural conditions. A comparison of techniques used in the measurement of stomatal pore imaging/monitoring is mentioned in table 2-1.

Table 2-1 Comparison of techniques used in the measuring of stomatal pore dynamics

Methods to monitor the stomatal opening	Method type	Manipulation of a leaf	Real-time monitoring	Long-term monitoring	In-field imaging	Direct measurement of stomatal pore dynamics	Accuracy
Mold Impression method	Direct method	Physical & Chemical	×	×	×	×	Less accurate
Fluorimetric measurement of stomatal activity	Direct method	Chemical	○	○	×	○	Less accurate
Porometer	Indirect method	Not required	○	×	○	×	Less accurate
Electro-mechanical sensor	Indirect method	Physical & Chemical	○	○	Only for movable plants	×	Not possible
Infrared-thermography	Indirect	Not required	○	○	○	×	Less accurate
Portable microscope based method	Direct method	Not required	○	○	○	○	Highly accurate

‘○’ possible; ‘×’ not possible

2.2 Experimental setup and portable high-resolution microscope

Experimental setup broadly consists of a high-resolution portable reflected microscope for real-time monitoring of stomata and a leaf holder attached to x-y-z stage to stabilize the leaf (mainly the area of imaging) as shown in Fig. 2-4. Our microscope has an upward facing commercial 40× magnification finite microscope objective lens (NA 0.6), an image sensor (1600 × 1200 pixels, pixel size 3 μm × 3 μm, Eyecam), a plate type beam splitter (BS, 25 mm in diameter, 30R/70T, Edmund Optics) and light-emitting diode (LED) based Koehler illumination source. The light source consists of a two-watt surface-mounted white LED and an aspherical condenser lens (Ø: 25 mm, focal length: 20 mm, NA 0.6). The image sensor was placed close to the objective lens for compactness of the setup (Fig. 2-4A and 2-4B) and tube lens was not used. Microscopic components were optically aligned with the help of 3D printed structures (Fig. 2-4B). To hold the leaf surface parallel to the microscope-imaging plane, a leaf holder has been designed and fabricated. To avoid the reflection of light from the internal walls of lens holder, all cavities of lens holder were lined with black color velvet paper from inside. The whole microscope was covered by aluminum foil to ensure that ambient light should not interfere with the microscopic optical system in sunlight.

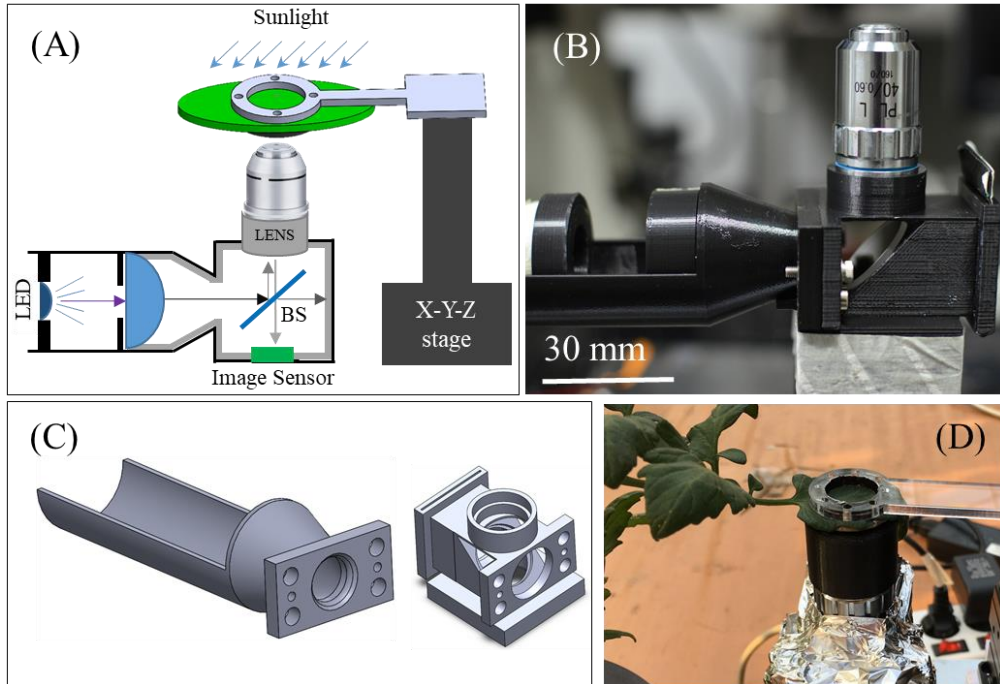


Fig. 2-4. Experimental setup of real-time in-situ stomata imaging and monitoring in a field (A) Schematic of the portable reflected type microscope having upward facing objective lens and novel leaf holder attached to a x-y-z stage. (B) Customized compact reflected microscope consists of a commercial finite 40 \times objective lens, BS and LED-based light source in 3D printed support frame (light source holder and lens holder). (C) Computer-aided design (CAD) of light source holder and lens holder. All the cavities of lens holder were lined with black color velvet paper from inside to reduce the reflection of light from walls of cavities. The whole microscope was covered by aluminum foil to ensure that ambient light should not interfere with the microscopic optical system in sunlight (D) Direct real-time imaging of lower epidermis stomata in field.

2.3 Tomato plant cultivation

Stomata imaging of tomato leaf was conducted in a transparent vinyl film covered greenhouse (Gwanak-gu, Seoul) under natural environment as shown in Fig. 2-5. Experiments were conducted on two ways grew tomato plants, one having controlled irrigation of nutrients based on solar radiation and another having the irrigation of nutrients on a daily basis. Tomato plants were planted in Rockwool cubes ($10 \times 10 \times 6.5$ cm, UR Rockwool, Korea) and sufficiently saturated with the standard nutrient solution for tomato plants (Glasshouse Crops Research and Experiment Station at Naaldwijk, Netherlands). Nutrient solution was supplied with the help of a proportional control method of integrated solar radiation using a drip irrigation system (Netajet, Netafim Korea, Korea). Experiments were conducted on six weeks old tomato plants. During the experiment, wind velocity was negligible.



Fig. 2-5. Tomato plant cultivation in transparent vinyl film covered greenhouse situated at Gwanak district at Seoul

2.4 Measurement of light intensity

The intensity of sunlight was measured with the help of a light-meter (Lutron LX-1108 Taiwan) in unit 'Lux'. The light meter measures the SLI in range of 40-400,000 Lux. To measure the maximum SLI inside the greenhouse, the sensor of the light-meter was faced towards the sun and the maximum value was recorded. On the other hand, SLI value on the leaf surface was estimated by placing the sensor of light-meter close and parallel to the leaf surface as shown in Fig 2-6.



Fig. 2-6. Measurement of maximum light source intensity at experimental place and parallel to the leaf (A) light-meter (Lutron LX-1108 Taiwan) (B) maximum intensity of light source (C) intensity of light source parallel to the leaf surface

2.5 Imaging of micrometer-sized object by portable reflected microscope

Microscale imaging of rectangular grid patterns ($50\ \mu\text{m} \times 50\ \mu\text{m} \times 5\ \mu\text{m}$) of negative photoresist SU-8 on a silicon wafer (opaque background) is performed by our microscope and compared with the Nikon eclipse microscope as shown in Fig. 2-7.

Fabrication of SU-8 rectangular grid patterns on silicon wafer

Rectangular grid patterns of photoresist, SU-8 3005 (Microchem USA) was fabricated on a 4-inch silicon wafer by a single-mask photolithography process. First, photoresist SU-8 was spin-coated on a clean silicon wafer at 500 RPM and 4000 RPM speed for 30 seconds and 60 seconds respectively, followed by a soft bake process at 65°C for 180 sec. Next, the wafer was exposed to $150\ \text{mJ}/\text{cm}^2$ UV (365 nm) source followed by a post-exposure bake at 95°C for 60 seconds. Further, the sample was immersed in MicroChem's SU-8 developer for 120 seconds to develop the photoresist and rinsed with deionized water thoroughly. Finally, the sample was hard bake at 150° for 60 seconds for good adhesion of developed SU-8 grid pattern on a silicon wafer.

Imaging of rectangular grid patterns

The image quality taken by our microscope was compared with the image of a Nikon eclipse reflected microscope ($20\times$ objective lens, NA 0.45) using of

rectangular grid patterns. Image quality obtained by both microscopes were comparable and no distortion has been observed in the image obtained by our microscope. However, FOV ($350\ \mu\text{m} \times 262\ \mu\text{m}$) of our microscope was smaller than the FOV ($670\ \mu\text{m} \times 500\ \mu\text{m}$) provided by a Nikon microscope (20 \times objective lens, NA 0.45). Still, the imaging area of $350\ \mu\text{m} \times 262\ \mu\text{m}$ was enough to monitor 20-30 stomata simultaneously in the abaxial layer of the tomato leaf. For compactness of the microscope, the image sensor was placed close to an objective lens without using the tube lens between an objective lens and image sensor. This further reduces the optical attenuation in the image formation owing to the optical systems of the tube lens, which helps to obtain a sharp image of an object. Without tube lens, the image of an object should be distorted in large FOV, however, in small FOV ($350\ \mu\text{m} \times 262\ \mu\text{m}$) of our microscope, no distortion has been observed in the image of rectangular grid patterns as shown in Fig. 2-7.

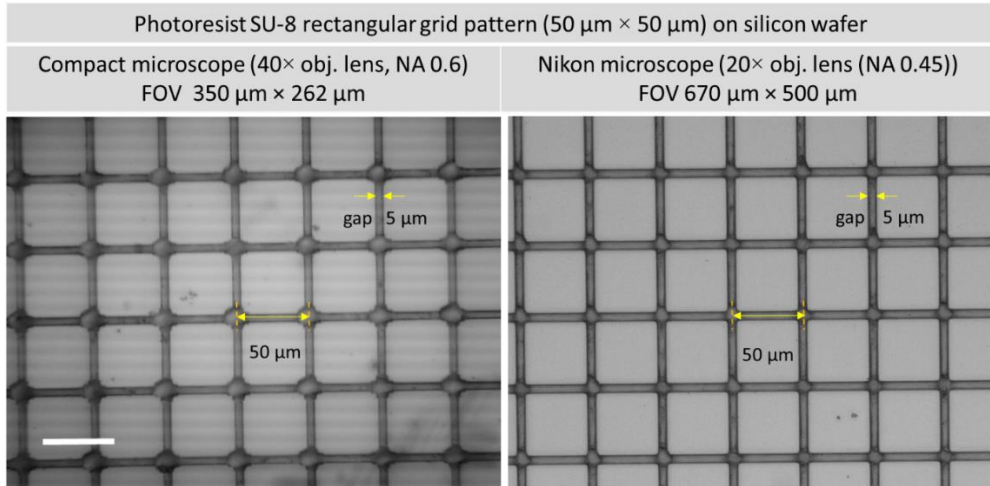


Fig. 2-7. Microscale imaging by portable reflected microscope (A) Imaging of microscale rectangular grid patterns ($50\ \mu\text{m} \times 20\ \mu\text{m} \times 5\ \mu\text{m}$) of photoresist SU-8 on a silicon wafer. Image quality obtained by compact microscopic setup is comparable to the standard Nikon reflected microscope. Band noise (horizontal lines) in the image obtained by our microscope was due to overexposure of image sensor. Scale bar $50\ \mu\text{m}$

2.6 Measurement of optical resolution

An optical resolution of the portable microscope was measured in term of half-pitch spatial resolution (HSR) by an extreme microscope resolution target, 1951 USAF (Amazon.com). Microscope resolution target has the smallest HSR value of $0.137\ \mu\text{m}$. Resolution target contains $100\ \text{nm}$ thick three equidistant vertical and horizontal direction chrome bars of different HSR values increasing in width by $\sim 12.4\%$ of the previous value (HSR value: $0.137\ \mu\text{m}$ to $31.250\ \mu\text{m}$) plated on quartz background. An optical resolution of a

microscope (with a 40× objective lens, NA 0.6) was determined after distinguishing the three vertical and/or horizontal parallel bars of minimum HSR value.

As shown in Fig. 2-8, at HSR value of 0.548 μm (FOV 350 μm \times 262 μm), both direction lines (vertical and horizontal) were clearly distinguishable. However, a lower HSR value (0.488 μm) was obtained when only one-direction lines were distinguishable. We believe that the background vibrations was one of the reason not to clearly visualize both direction lines at HSR value of 0.488 nm. Overexposing the image sensor by a LED-based vertical light source produced the band noise (horizontal lines) in the image obtained by our microscope (Fig. 2-7).

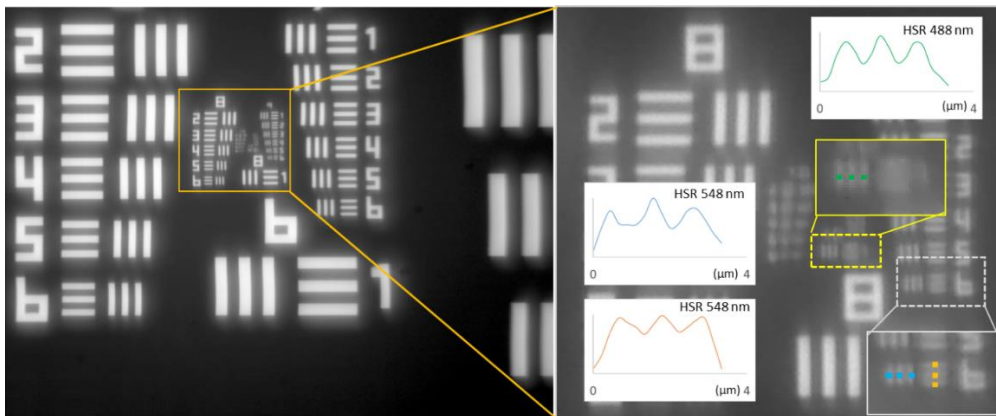


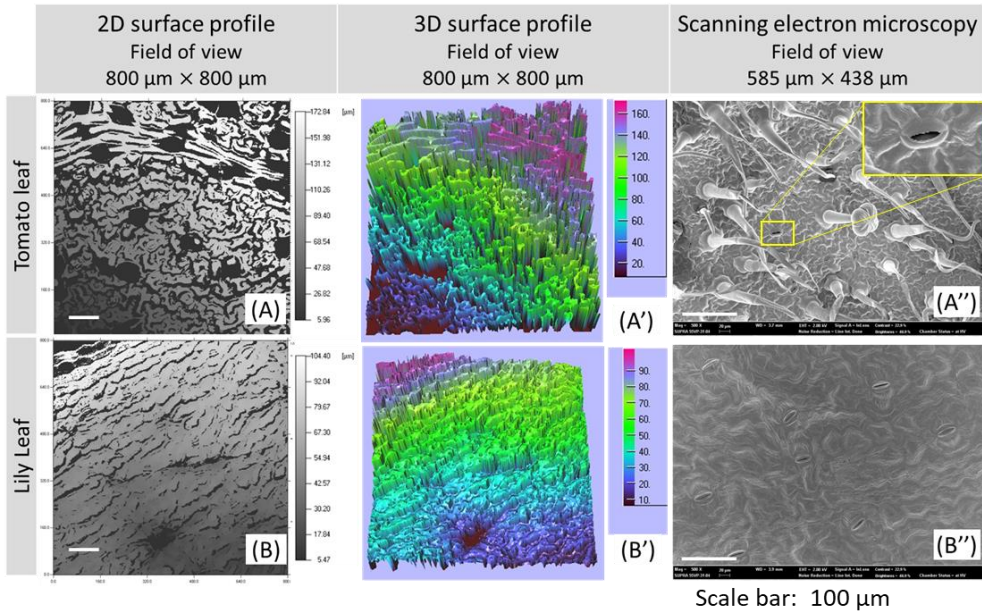
Fig. 2-8. Measurement of optical resolution of portable reflected microscope in term of half-pitch spatial resolution (HSR) value. HSR value was 0.548 μm (FOV 350 μm \times 262 μm) when vertical and horizontal both direction lines were clearly distinguishable and 0.488 μm when one-direction lines were distinguishable. We

believe that the background vibrations, smaller distance lens and image sensor were the reasons not clearly visualize both direction lines at HSR value of 0.488 nm.

2.7 Tomato leaf surface profile

Understanding the surface texture of a leaf is important for the optical microscopy of stomata. Surface profile measurement and high-resolution imaging of tomato leaf and lilly were conducted by 3D surface profiler (Nanofocus μ surf, 176 \times optical magnification) and field-emission scanning electron microscope (FESEM, Carl Zeiss SUPRA Germany, 500 \times magnification) respectively (Fig. 2-9). 3D surface profiler is an optical microscope, capable of scanning the area of 800 μ m \times 800 μ m with maximum vertical measurement range of 300 μ m at 176 \times optical magnification. Leaf samples were scanned by 3D surface profiler without any physical or chemical manipulation. To prepare the leaf sample for FESEM imaging, a fresh detached leaf was cut into the 2 mm \times 2 mm pieces and submerged immediately into a Karnovsky fixative media for 2 hours at room temperature. After primary fixation, leaf pieces were washed thoroughly in 0.05M sodium cacodylate buffer 3 times followed by in distilled water 2 times. To dehydrate the sample, the sample was washed in graded ethanol (30%, 50%, 70%, 80%, 90% and 100% (3 times)) each for 10 min. Finally, the leaf samples were dried in Critical Point Dryer (EM CPD300, LEICA) before electron microscopy.

Results obtained by the 3D surface profiler and FESEM showed a highly non-planar surface of tomato leaf with an height profile of 172 μm (FOV 800 $\mu\text{m} \times 800 \mu\text{m}$) compared to the lily leaf where maximum height profile of 104 μm (FOV 800 $\mu\text{m} \times 800 \mu\text{m}$) has been observed . In addition, FESEM images revealed a dense population of trichome, a hair and granular like structures on the surface of a tomato leaf. However, trichome were absent in a lily leaf. Non-planar surface of the tomato leaf limits focusing the stomata in large FOV. Hence, multiple images focusing at the different stomatal plane in given FOV were captured to analyze the stomatal opening and stomatal density. Moreover, the presence of high-density trichome on leaf surface further hinders in obtaining the high contrast images of stomata. However, the use of a 40 \times microscopic objective lens having a small depth of field ($\sim 1.3 \mu\text{m}$) helps to focus on the stomatal plane even if in the presence of high-density trichome (refer Fig. 2-10D and Fig. 2-10D').



(D)



Tomato leaf sample

(E)



Lily leaf sample

Leaf sample size: 5 mm \times 5 mm

Fig. 2-9. Surface profile measurement and electron microscopy of tomato and lily leaf. (A and A') 2D and 3D surface profile measurement by 3D surface profiler of tomato leaf at 176 \times optical magnification. A height profile map demonstrates higher non-planarity of tomato leaf of 172 μm (FOV of 800 μm \times 800 μm). Scale bar: 100 μm . (A'') FESEM image of the lower epidermis of a tomato leaf at 500 \times magnification showing highly dense population of trichome. Trichome are hair like structures, which makes the surface further difficult for imaging. Scale bar: 100 μm

(C) 3D surface profiler (Nanofocus μ surf) (D) & (E) Tomato and lily leaf sample respectively.

2.8 A need of reflected microscope with Koehler illumination (vertical illumination) for *in-situ* stomata imaging

An interaction of ambient light with the optical system of a microscope may result in poor imaging of an object. A comparative study of lower epidermis stomata imaging of a tomato leaf (leaf thickness 150 μ m-250 μ m, excluding leaf veins) by a portable transmitted and reflected microscopes in dark (inside laboratory) and bright (inside the greenhouse during daytime) environment is shown in Fig. 2-10. A reflected microscope provides high-quality images of abaxial stomata in the laboratory as well as in the field environment. Both microscopes consist of 40 \times finite objective lens; an image sensor and white LED-based imaging source. Details of a portable transmitted microscope are mentioned in our previous work(Purwar, Han et al. 2019). In case of the transmitted microscopy, imaging of the lower epidermis without any interaction between ambient light and a microscopic optical system is difficult while exposing the upper epidermis to the ambient light in the field. Moreover, the use of a high-intensity light source to counter the effect of ambient light may damage the leaf and affect the working of stomata. In addition, imaging of lower epidermis stomata by a transmitted microscope should also have

footprints of several upper and intermediate layers of the leaf, which will produce a poor contrast image of lower epidermis stomata (Fig. 2-10C). As a result, a transmitted microscope is not suitable for stomata imaging. Hence, a reflected microscope capable of lower surface imaging of a leaf should be used for stomata imaging.

Unlike commercial reflected microscopes, our portable microscope consists of an upward facing objective lens and microscope can be placed under the leaf surface easily. Use of side illumination (specular illumination, diffuse illumination, near vertical illumination etc.) can produce shadows on the rough surface of a leaf (refer Fig. 2-11). Hence, a vertical Kohler illumination source was used to obtain a clear and contrast image of stomatal aperture. Moreover, vertical Kohler illumination requires a low power light source (3 watts LED is used) and illuminates only the imaging area of the leaf (~ 1 mm in diameter). Further, a vertical illumination limited to the imaging area of the leaf does not interfere with the stomata functions (Koman, Lew et al. 2017). Importantly, it is possible to expose the upper epidermis of the leaf to the sunlight during stomata imaging. In the field, a leaf was fixed mechanically by a leaf holder and a leaf cap was used to restrict the ambient sunlight during imaging (Fig. 2-10D and 2-10D’).

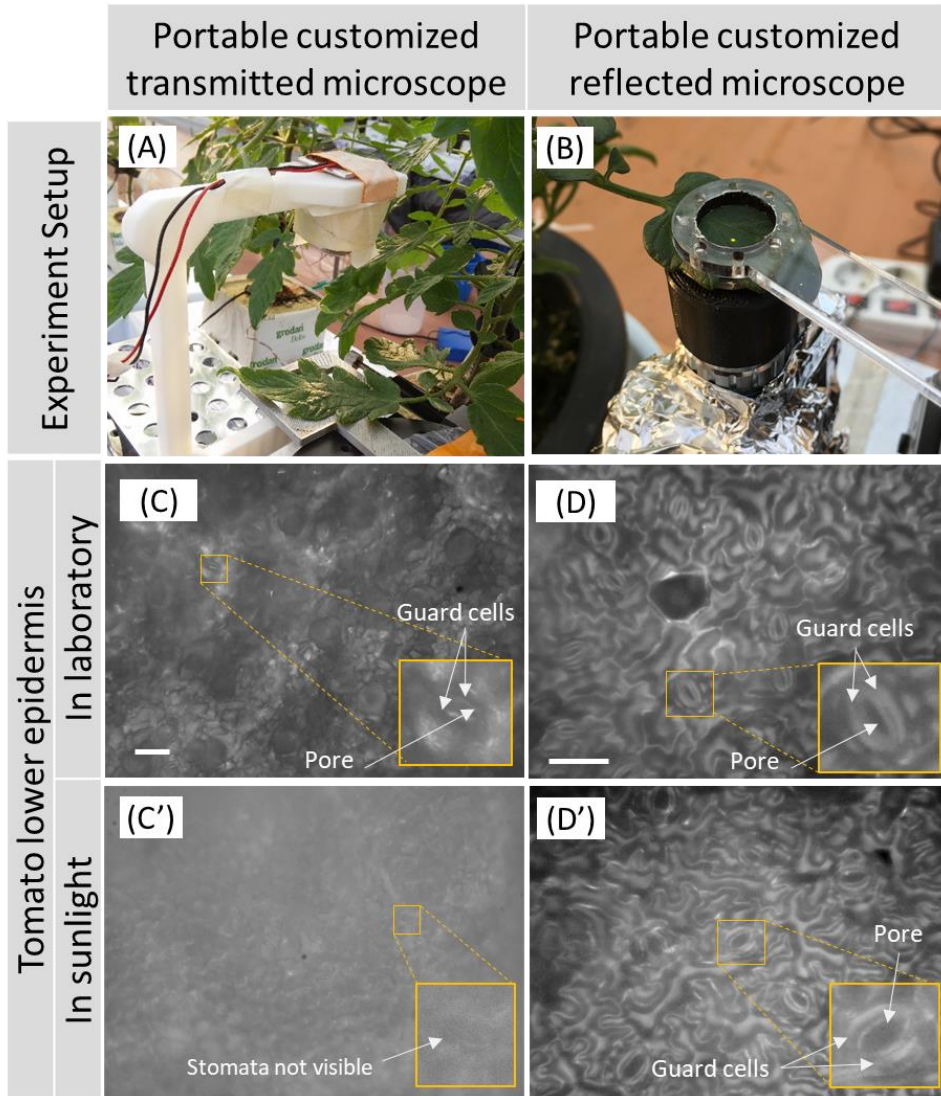


Fig. 2-10. Stomata imaging by compact transmitted and reflected microscopes in laboratory and field environment. Experimental setup for stomata imaging by (A) a portable transmitted type microscope (B) a portable reflected type microscope. Observation of tomato stomata of lower epidermis when imaged in the laboratory environment by (C) transmitted microscope. Scale bar: 100 μm (D) reflected microscope. Scale bar: 50 μm and in the field by (C') transmitted microscope (D') reflected microscope. In case of a transmitted microscope, stomata observation was only possible in a laboratory environment since ambient light in field interfere with

the optical system of a microscope. The image quality of stomata imaging was comparable when observed by reflected microscope in a laboratory as well as field environment. Stomata and guard cells, both, were clearly visible.

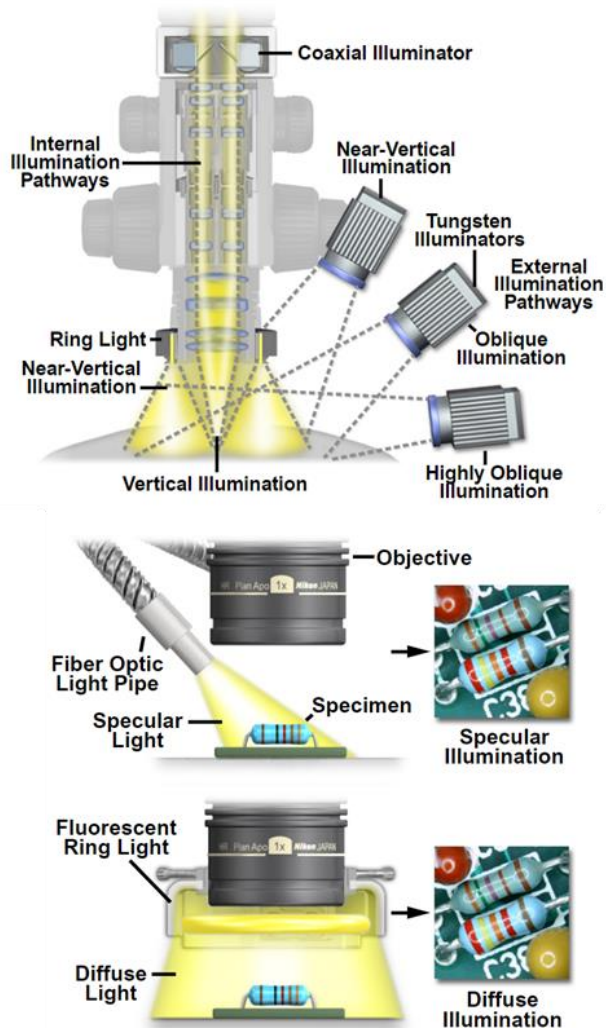


Image source: www.microscopyu.com

Fig. 2-11. Different types of reflected light illumination sources such as ‘Near-vertical illumination, tungsten illumination, oblique illumination and highly oblique illumination, diffuse illumination etc. used in reflected microscope

2.9 Leaf holder

2.9.1 Requirement of a leaf holder

For continuous monitoring of lower epidermis stomata, it is essential to hold the leaf surface parallel to the microscope-imaging plane. Leaf holder should hold the leaf enough tightly so that wind or other disturbance should not change the imaging area. On the other hand, it should not apply a large force to damage the leaf surface. Leaf clip holders used in the measurement of leaf parameters such as chlorophyll contents (Heinz Walz GmbH, Germany) and electrical capacitance block the lower epidermis layer of a leaf (refer Fig. 2-12) (Afzal, Duiker et al. 2017). Hence, these leaf clip holders are not suitable for continuous imaging of abaxial stomata. Therefore, a novel leaf holder has been designed and fabricated. Leaf holder allows the upper surface (adaxial surface) of a leaf open to the sunlight and the lower surface (abaxial surface) of the leaf to the wind simultaneously. Thick transparent acryl sheet of upper leaf holder holds the leaf in a position and allows the sunlight on the upper epidermis of a leaf, a predominant stimulus affecting the stomatal aperture (Gray and Peirce 1919).

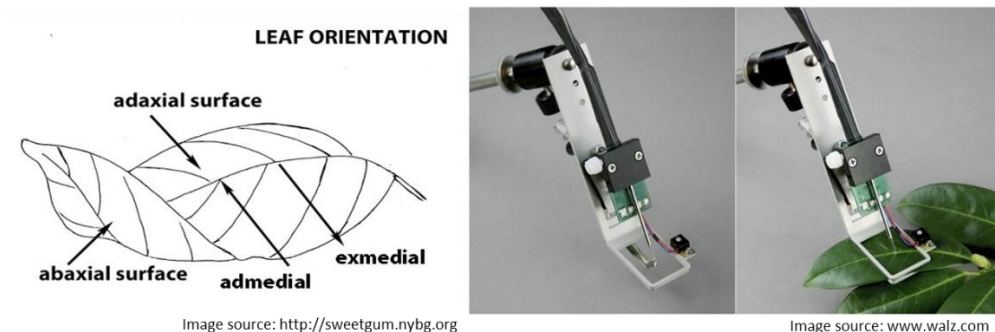


Fig. 2-12. Schematic of an upper (adaxial) and lower (abaxial) surface of a leaf and a commercial leaf holder. Stomata are found prominently on the lower surface of a leaf. A leaf holder developed by Heinz Walz GmbH, Germany for measurement of leaf's parameter such as chlorophyll contents, temperature and humidity.

2.9.2 Design and fabrication of leaf holder

A novel leaf holder has been designed and fabricated with the help of a laser cutter (Universal Laser System USA) and 3D printer (DP200, Sindoh Korea) as shown in Fig. 2-13. Leaf holder consists of four parts; named as upper leaf holder, lower leaf holder, leaf cap and a lens cap (Fig. 2-13A and 2-13B). Upper leaf holder is made of 3 mm thick transparent biocompatible polymethylmethacrylate (acryl) sheet and allows a 15 mm diameter area of the leaf for microscopy (Hollick, Spalton et al. 1998, Gautam, Singh et al. 2012). The upper leaf holder is attached to an x-y-z stage to focus the leaf surface for microscopic imaging. A lower leaf holder of thickness 1.5 mm is fabricated with a black color biocompatible polylactic acid (PLA) material to restrict the

ambient light reaching to the sample from backside (Tsoua, Kao et al. 2015, Savaris, Braga et al. 2017). The thickness of the lower leaf holder was determined after considering the distance between the leaf surface and an objective lens (~2.5 mm) when the lower epidermis was in focus. To avoid the interference of ambient light reflected from lens surface with the optical system of the microscope, the lens was also covered with a black color lens cap made of PLA material.

During transpiration, there is a diffusion of gases from environment to plant body and excretion of water in vapor phase. The use of a lower leaf holder together with a lens cap forms an opaque cavity and restrict the wind to pass through the lower epidermis surface. In addition, stomatal water vapor is unable to diffuse into the environment. Combination of both events affect the stomatal conductance and result in a deposition of water droplets on lower epidermis. Further, deposited water vapor affects the stomata functions as well as microscopy of stomata as shown in Fig. 2-14C (left leaf). Therefore, to allow the wind at abaxial side of the leaf, 2 mm wide V-shape notches were patterned on lower leaf holder (refer Fig. 2-14). V-shape notches allow the wind and restrict the ambient sunlight pass through the abaxial side of a leaf. The sample (leaf) was anchored in between the upper and lower leaf holders with the help of four small permanent neodymium magnets embedded in the upper ($\text{\O} 2$ mm, thickness 1.5 mm) and lower ($\text{\O} 3$ mm, thickness 1.5 mm)

leaf holders. During microscopy, upper leaf surface was closed by leaf cap to restrict the interference of ambient sunlight with the optical system of the microscope as shown in Fig. 2-13C and Fig. 2-13C'. Small neodymium magnets embedded in upper and lower leaf holders, does not affect the sunlight intensity reaching the leaf epidermis. In addition, no visible physical damage on the leaf surfaces has been observed when the leaf was sandwiched between upper and lower leaf holder for more than 24-hours (refer Fig. 2-14C (right)). During microscopy, the upper surface of the leaf was closed by leaf cap to restrict the interference of ambient sunlight with the optical system of the microscope (Fig. 2-13C and 2-13C'). In such a way, the leaf was exposed to the ambient light throughout the experiment and high-quality images of stomata were obtained at regular interval by using lens cap without damaging the leaf.

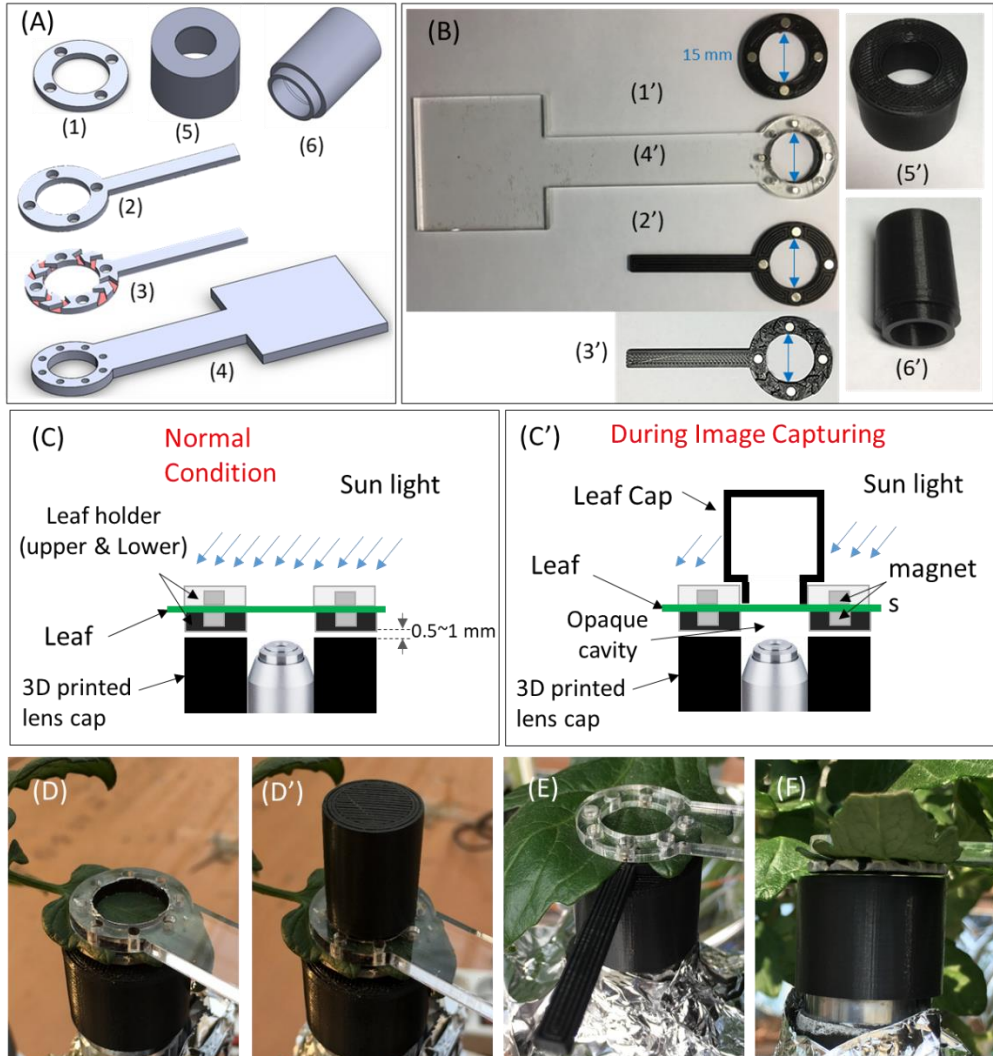
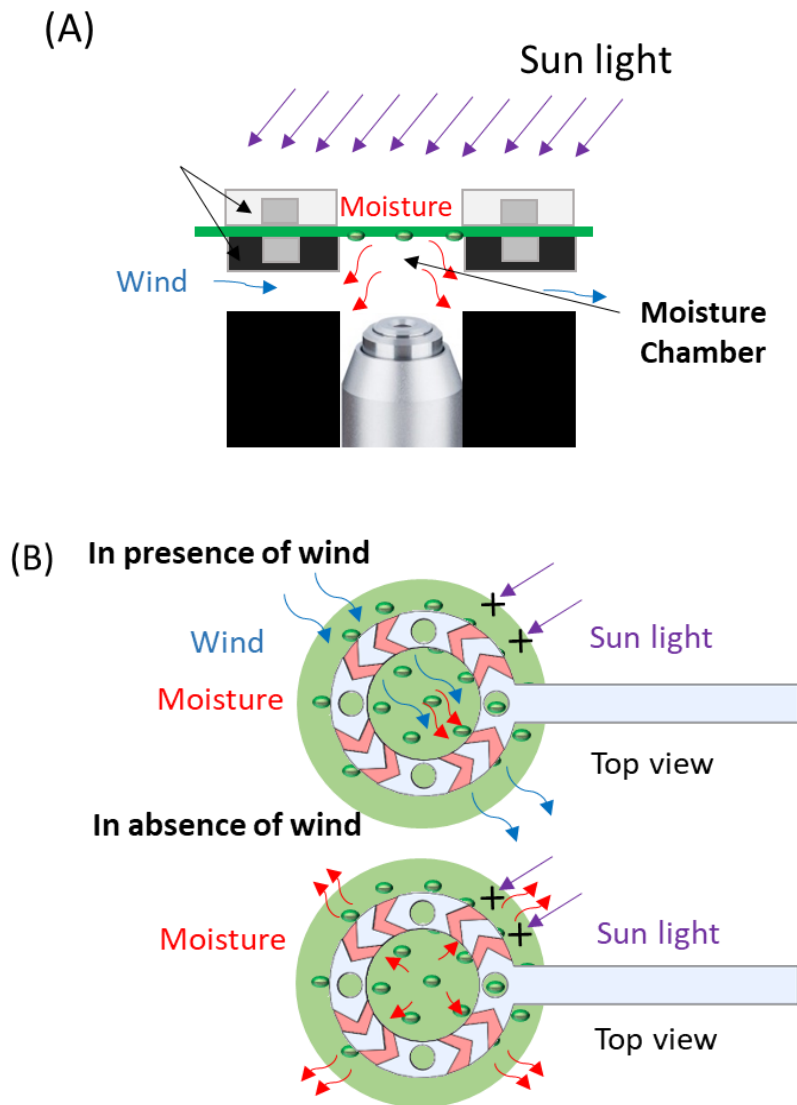
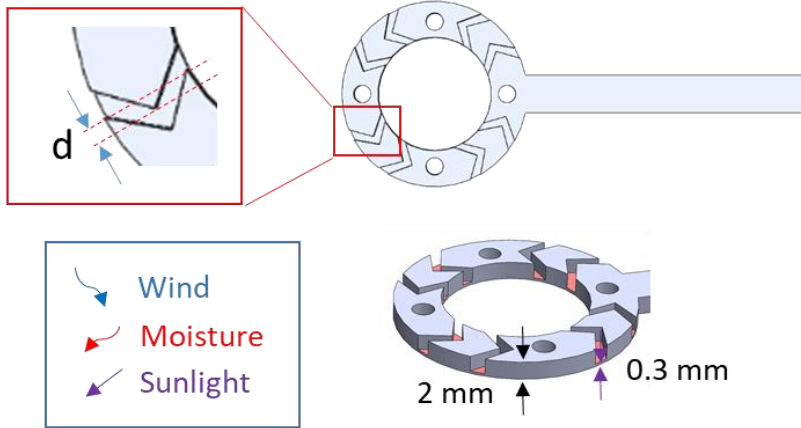


Fig. 2-13. Leaf holder: a device to hold and stabilize the leaf for long-term stomata imaging. (A) CAD design of leaf holder components. Upper leaf holder (4) is made of 3 mm thick transparent acryl sheet to allow continuous monitoring of stomata while the upper surface of the leaf exposed to the sunlight. Lower leaf holder (1, 2 or 3) is 1.5 mm thick and fabricates using a 3D printer in black color. V-shaped notches of width 2 mm have been designed in lower leaf holder (3) to allow the wind blow and restrict the ambient light at the abaxial layer of the leaf. Small permanent neodymium magnets embedded in the upper and lower leaf holder helps to hold the

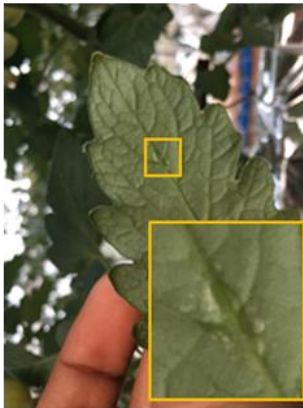
leaf even if during the wind blow. (B) 3D-printed structures of leaf holder (C and D) Leaf holder in normal condition (C' and D') Use of lens cap to avoid ambient sunlight during microscopy. (E) Lower leaf holder with handle. Handle helps to attach the lower leaf holder to the upper part without damaging the biological structures of the lower epidermis of the leaf. (F) A gap of 0.5~1 mm between the lens cap and lower leaf holder to move the sample freely for stomata imaging.



To restrict the light, $d \geq 0$



(C) **Lower leaf holder without grooves**



Deposition of water droplets after long term monitoring

Lower leaf holder with grooves



No water droplets deposition after long term monitoring

Fig. 2-14. Designing and fabrication of lower leaf holder (A) Schematic presentation of V-shaped notches allowing the wind blow and moisture across the leaf area under investigation and restricting the sunlight for the same area. (B) Water vapors accumulation in the night when lower leaf holder '2' (left leaf) vs leaf holder '3' (right leaf) was used. No physical damage was observed by leaf holder after continuous monitoring.

2.10 Effect of tilted stomata on quantification of stomatal opening area (or, pore area); a cosine effect

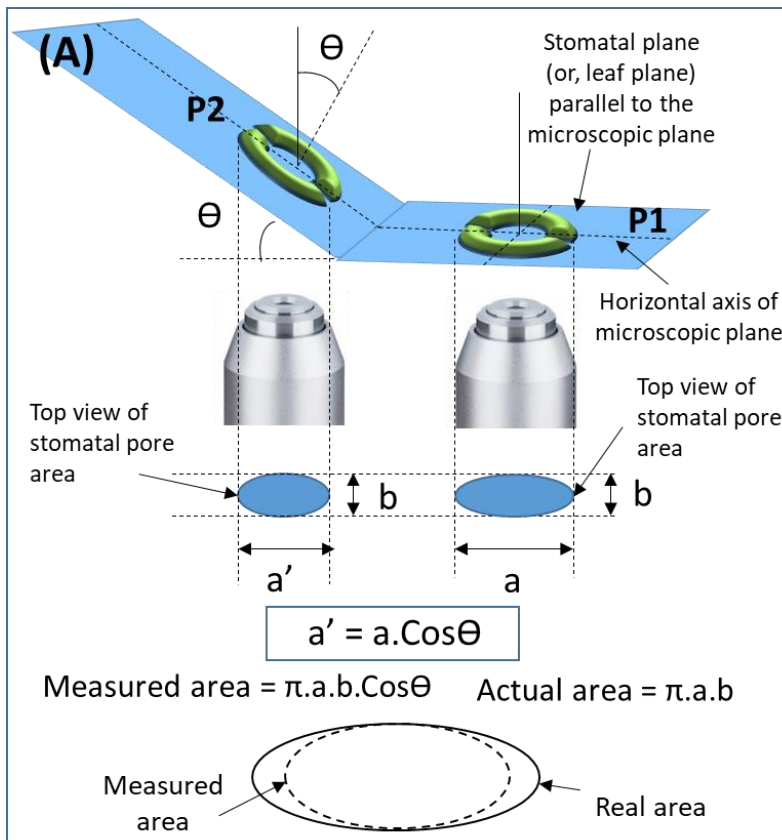
Due to the non-planar surface of the leaf, the leaf plane may not be parallel to the focal plane of the microscope. This may result in an error in stomatal pore area measurement. Schematic of measurement of stomatal pore area when stomatal plane is parallel and at an inclination angle ' Θ ' to the microscopic focal plane is shown in Fig. 2-15A. When the stomatal plane is at an angle ' Θ ', there should be a cosine effect in measurement of stomatal pore area. In ideal condition, when major axis of the stomatal pore area is parallel to the horizontal axis of microscopic plane, the major axis of the stomatal opening should be $a \cdot \cos\Theta$, where 'a' is the major axis of stomatal opening in elliptical shape. However, there should be any error in measurement of minor axis (b) of stomatal pore. Assuming a perfect elliptical shape of stomatal opening,

$$\text{Real area of stomatal opening} = \pi \cdot a \cdot b$$

$$\text{Measured area of stomatal opening} = \pi \cdot (a \cdot \cos\Theta) \cdot b = \pi \cdot a \cdot b \cdot \cos\Theta$$

Hence, the real area of stomatal opening = Measured area of stomatal opening / $\cos\Theta$. Θ is the angle of inclination of leaf plane to the microscopic focal plane. Inclination angle ' Θ ' can be measured in two ways. In first method, vertical distance 'd' can be measured through focusing the top (focus '1') and bottom (focus '2') edge of a stomata (refer Fig. 2-15B). However this method will suffer from accuracy since it is difficult to focus the top and bottom edge

of a stomata due to the small size of stomata. This approach will require a highly precise Z-axis movement of sample through the attached X-Y-Z stage and small depth of field of objective lens. Alternatively, if we assume the leaf surface is flat and at an inclination angle ' Θ ' to the microscopic plane, the inclination angle ' Θ ' can be measured with the help of distance ' D ' and one dimension (horizontal or vertical) of microscopic field of view as shown in Fig. 2-15 C.



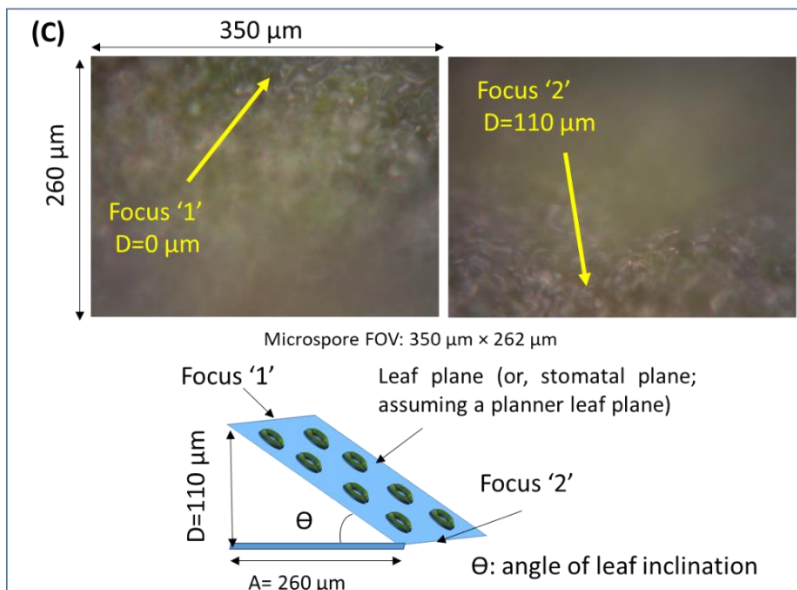
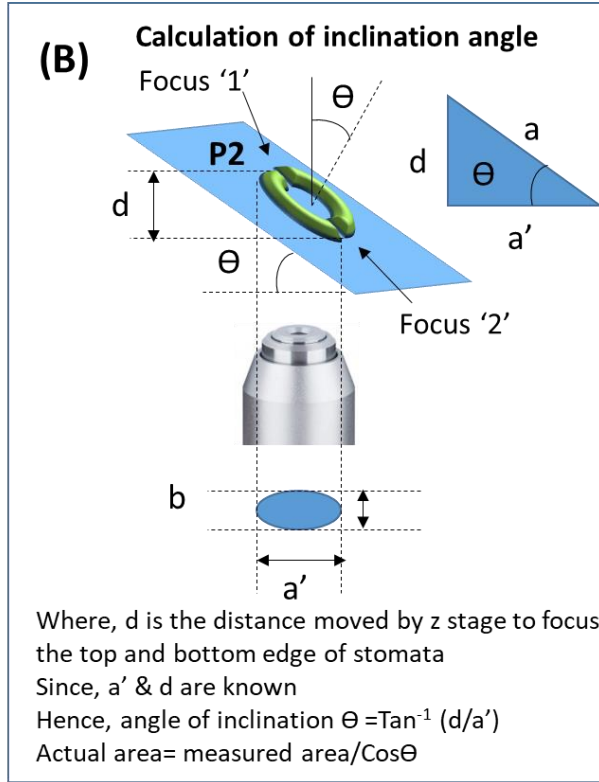


Fig. 2-15 Effect of tilted stomata on quantification of stomatal opening area. (A) schematic representation to show the effect on area and how to calculate the real area

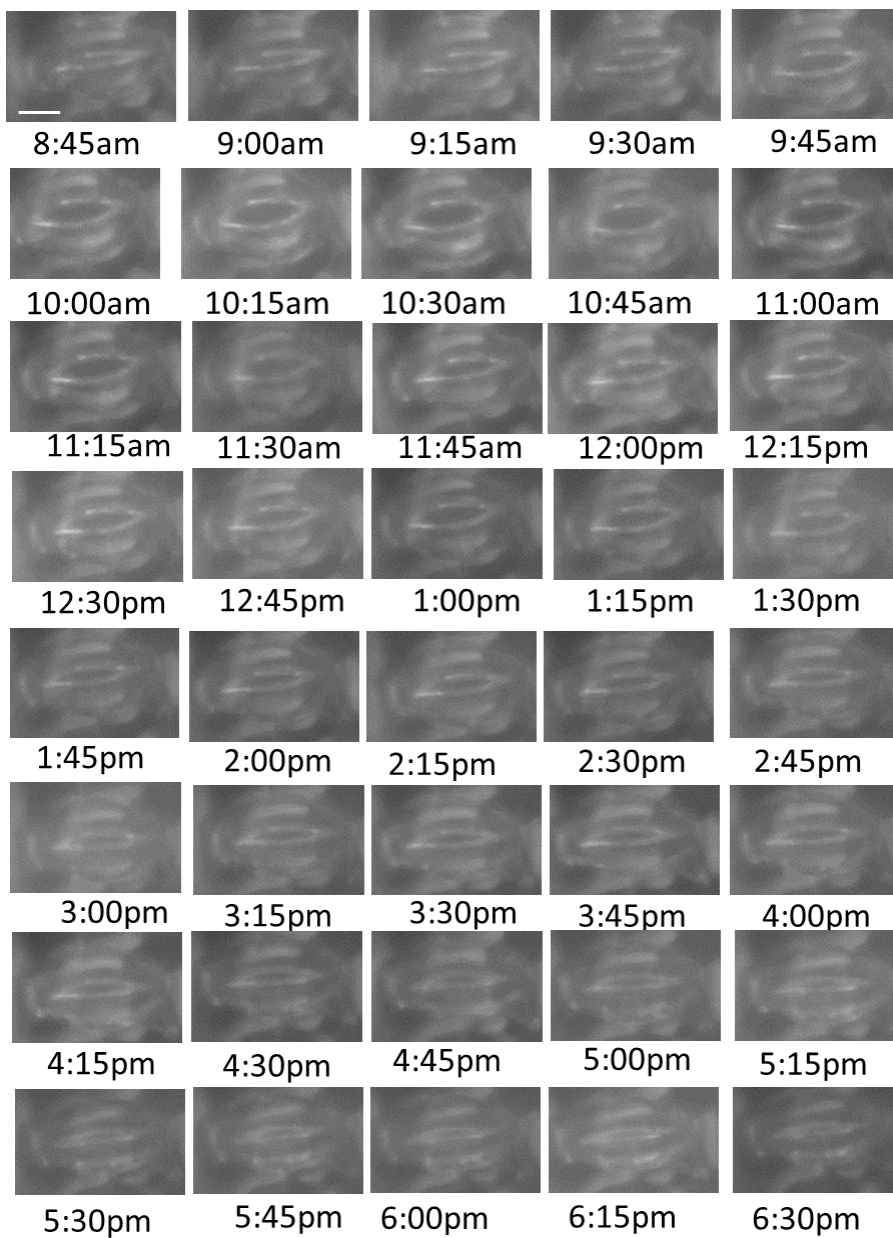
if measured area and angle of inclination is known (B) measurement of inclination angle with the help of a single stomata. However, this method may have a large error and requires precise measurement (C) measurement of inclination angle with the help of focusing the leaf at opposite sides of horizontal/vertical field of view of microscopic plane

2.11 Real-time *in situ* stoma imaging, monitoring and effect of sunlight intensity

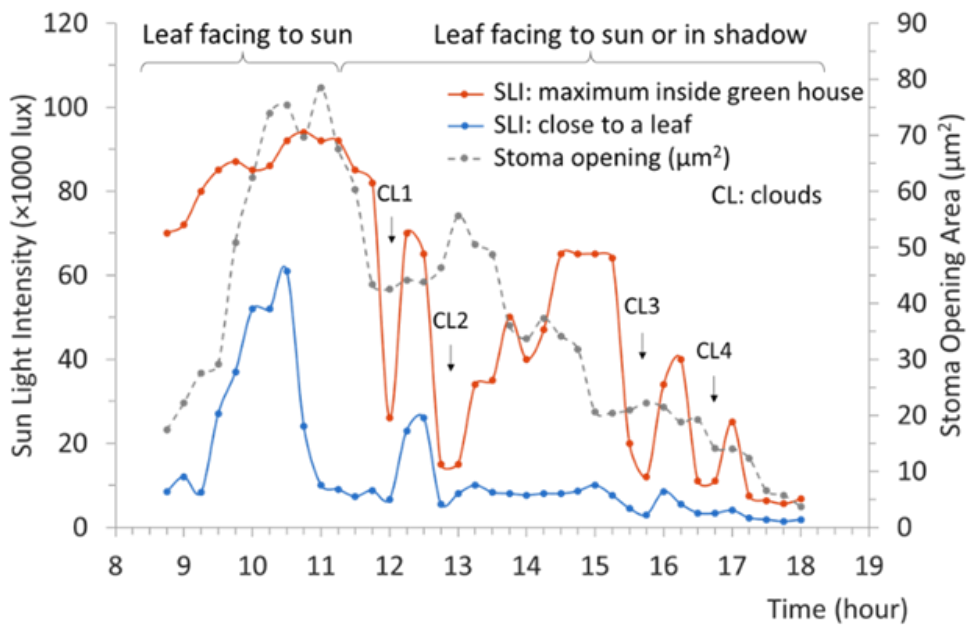
Real-time observation of stomatal functions is relevant to understand the optimization of plant physiological processes over million years of evolution (Raven 2002, Hogewoning, Douwstra et al. 2010, Koman, Lew et al. 2017). Changes in the stomatal aperture through external stimuli such as intensity of sunlight, temperature and humidity of surrounding environment and wind speed, is a result of the bidirectional flow of ions across the plasma and tonoplast membranes (Andrés, Pérez-Hormaeche et al. 2014). However, existing techniques are unable to quantify the changes in the stomatal aperture associated with environmental factors in a real-time manner under natural conditions. To understand the effect of sunlight intensity on stomatal aperture, real-time monitoring of abaxial stoma was performed under sunlight in a field at the interval of 15 minutes. Prior to stomatal imaging, the leaf has been anchored by a customized leaf holder. Leaf holder attached with a XYZ translation stage holds the leaf surface parallel to the imaging plane of the

microscope and reduce the leaf movement in the windy environment throughout the experiment. Wind speed was negligible since the experiment was performed inside the greenhouse. A leaf, facing in the direction of sunrise, was selected to monitor the dynamics of stomatal aperture. However, in afternoon and evening, the leaf was under the shadow of other leaves and/or nearby tomato plants. Weather was clear and cloudy at the day of the experiment. Changes in the size of the stomatal opening (in μm^2) in response to the variation in the sunlight intensity is shown in Fig. 2-16. It has been observed that the size of stoma opening is a function of the sunlight intensity falling on the leaf compared to the maximum sunlight intensity near about. The intensity of sunlight less than 5,000 lux triggers the opening of stomata and further, higher intensity of light actuates the opening of stomata. The presence of clouds (CL) blocking the sun affects the ambient sunlight intensity as well as the intensity of light close to the leaf (refer clouds (CL) 1, 2, 3 and 4 in Fig. 2-16B.). If the clouds block the sunlight for a long duration, such an event affects the stoma opening, (refer CL 2 in Fig. 2-16B). However, a latency between change in sunlight intensity and resulted change in the stomatal opening has been observed. If the leaf of the interest is in shadow during the clouds blocking the sun, the intensity of sunlight close to the leaf does not vary significantly, and stomata opening gets unaffected. Maximum stomata opening of $80.3 \mu\text{m}^2$ has been measured.

(A) Real-time monitoring of stomatal pore dynamics



(B) Sunlight Intensity (SLI) vs Tomato Stoma Pore Opening



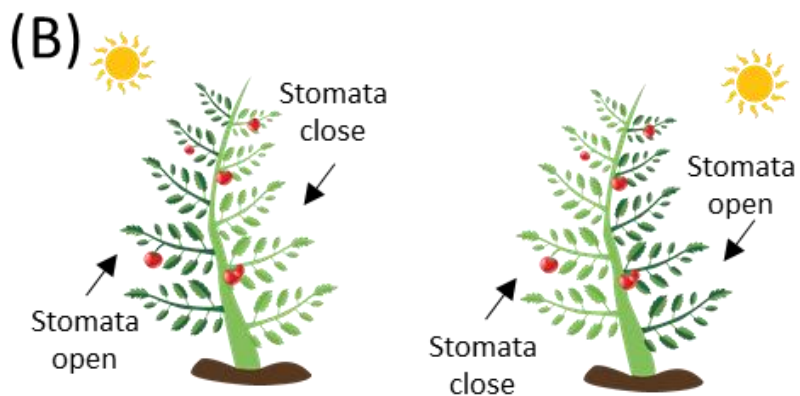
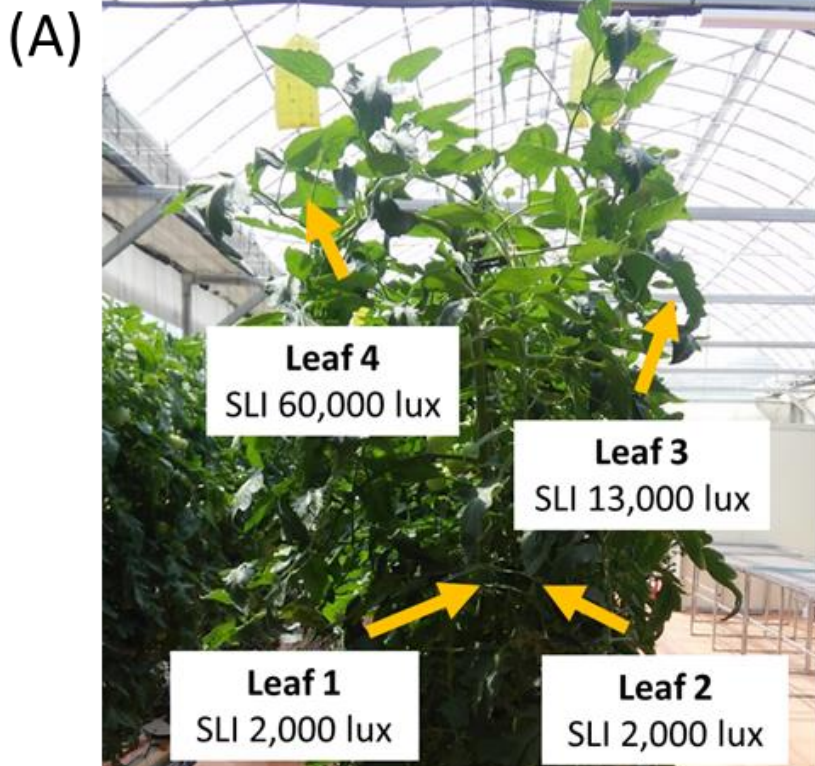
- Experimental month: July
- Time interval: 15 min
- Max stomatal opening area: 80.3 μm²
- Analysis tool: ImageJ
- Relative humidity condition: 40 -60%
- Wind speed: ~ 0 m/sec

Fig. 2-16. Real-time field monitoring of tomato stoma in sunlight (A) Imaging of stomal opening at an interval of 15 minutes. Scale bar: 10 μm (B) Stomal opening as a function of sunlight intensity. Stoma was responsive to the sunlight intensity falling on the upper epidermis compared to the maximum sunlight intensity of ambience inside the green house. The leaf under investigation was facing to sun in morning hours. However, during afternoon and evening it was under shadow of other leaves of the plant. The maximum stomatal opening of 80.3 μm² has been observed after maximum sunlight intensity recorded parallel and close to the leaf surface.

2.12 Stomata mapping of a plant

Plant leaves coordinate stomatal opening/closure in response to light stress by sending and receiving rapid systemic signals (Devireddy, Zandalinas et al. 2018). Stomata mapping of four leaves exposed to the different intensities of sunlight at a time were conducted in six-week-old well-watered tomato plant as shown in Fig. 2-17. Leaves were detached from the plant at 1 pm and microscopic imaging of stomata was performed immediately. Leaf 1 and 2 were in shadow. However, leaf 3 and 4 were facing the sun partially and completely. The intensity of sunlight parallel and close to leaf surface was 2000 lux in case of leaf 1 & 2 and 13,000 lux & 60,000 lux for leaf 3 and 4 respectively. It has been observed that most of the stomata in leaf 1 and 2 were closed due to the low intensity of sunlight. However, for leaf 3 where the intensity of sunlight was 13,000 lux, stomata were partially open. Moreover, leaf 4, which has a maximum intensity of sunlight of 60,000 lux, stomata, were wide open. Results implied that, stomatal opening is a direct function of sunlight intensity falling on the leaf and dependent on the location of a leaf in respect to the light source including other factors such as wavelength of light source, stomatal density, leaf age, wind velocity etc. (Gray and Peirce 1919, Wild and Wolf 1980, Renard and Demessemacker 1983, Assmann 1988). Hence, it can be concluded that the contribution of a leaf for photosynthesis and transpiration depends on its location in respect to the sun especially for a

plant having a high density of leaves. In addition, the plant porosity (total area of stomatal opening/ leaf area) changes continuously throughout of the day according to the geographical location of the plant in different weathers.



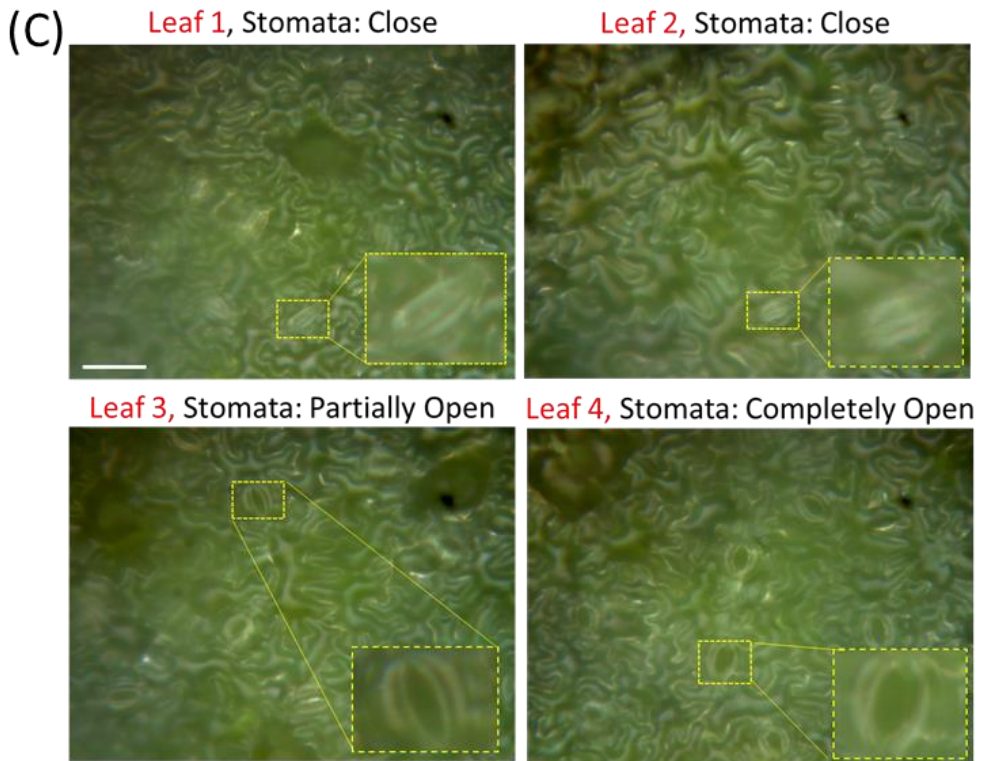


Fig. 2-17. Stomata mapping of leaves. Leaves were detached from the plant and microscopy was performed immediately. (A) Location of Leaf 1, 2, 3 and 4 with respect to sun location. Leaf 1, 2, 3 and 4 were exposed to the sunlight intensity of values 2,000 lux, 2000 lux, 13,000 lux and 60,000 lux respectively. (B) A schematic of opening and closing status of stomata with respect to the position of sun. (C) Stomata were found to be close In case of leaf 1 and 2. Both leaves were in shadow and exposed to the low intensity of sunlight (2,000 lux). However, stomata in leaf 3 and 4 were either partially or completely open since both leaves were exposed to moderate and high sunlight intensity (13,000 lux and 60,000 lux). Scale bar: 50 μ m

2.13 Quantification of stomatal density and changes in stomatal geometrical features in response to the sunlight intensity

Quantification of Stomatal Density

Static and dynamic stomatal properties control the stomatal conductance and determine the rate of transpiration and photosynthesis (Royer 2001, Xu and Zhou 2008, Orsini, Alnayef et al. 2012). Real-time quantification of stomatal static property (stomatal density) and dynamic property (stomatal opening) in response to the sunlight intensity has been performed. An experiment was conducted on a terminal leaf of the fourth petiole of a six-week-old tomato plant. To distinguish the stomatal complex from other epidermis structures, stomatal counting was performed when stomata were widely opened. Microscopic images of stomata were captured by a portable microscope and analyzed in 'ImageJ' software. Stomatal density (stomatal number per unit leaf area) was calculated by averaging the number of stomata observed at five different parts of a leaf (lower epidermis). To distinguish the stomatal complex from other epidermis structures, stomatal counting was performed when stomata were widely open (refer Fig. 2-18). Stomatal density was 27 ± 2.15 (n=5) in $350 \mu\text{m} \times 262 \mu\text{m}$ FOV or 282 stomata per mm^2 .

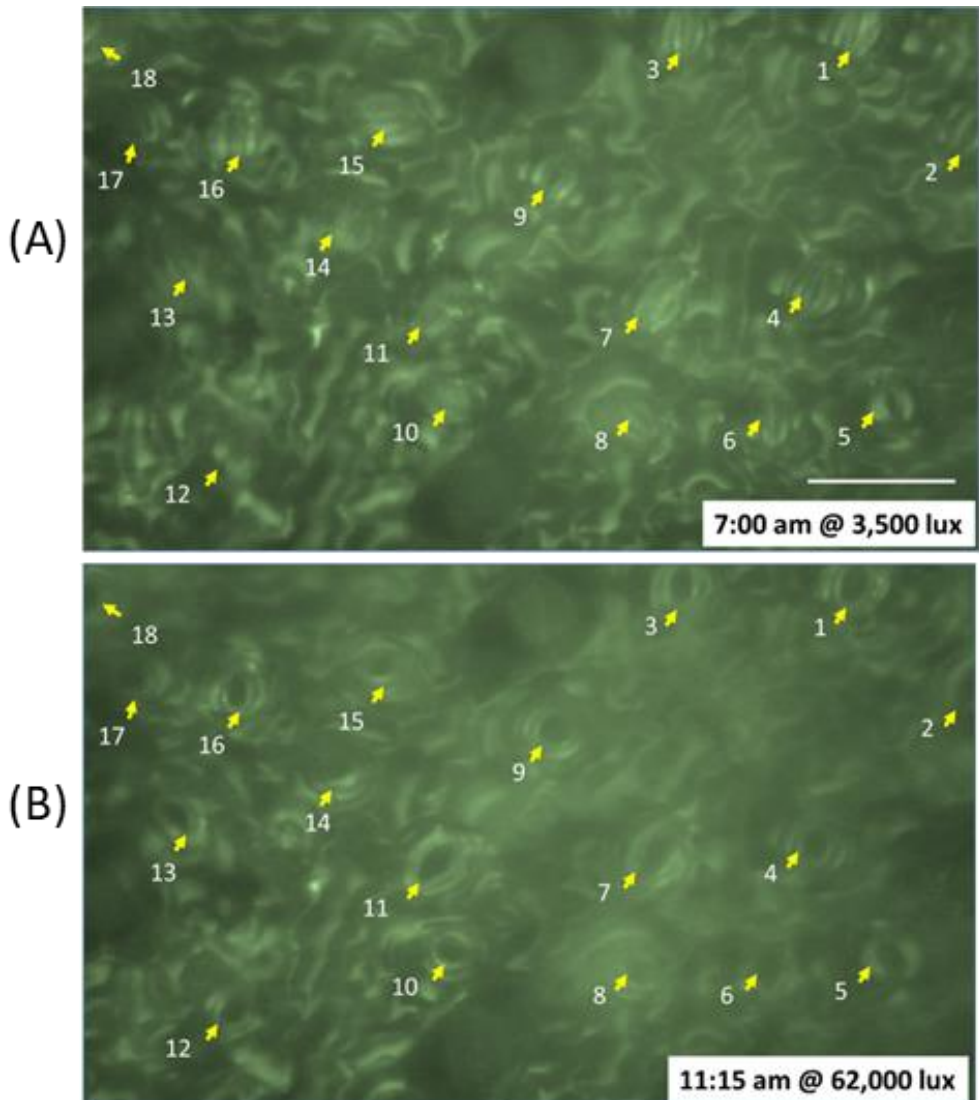


Fig. 2-18. Quantification of stomatal density of four-week-old tomato plant intact leaf under sunlight in a field. Status of the stomatal opening of an intact tomato leaf at 7:00 am (A) and 11:15 am (B) when the intensity of light close and parallel to the leaf surface was 3,500 lux and 62,000 lux respectively. Most of the stomata were close at 7 am, however, at 11:15 am; due to the high intensity of light all stomata were opened. To distinguish the stomatal complex from other structures of the epidermis, stomatal density was quantified when stomata were open. Scale bar 50 μ m.

Changes in Stomatal Geometrical Features in Response to the Sunlight Intensity

Stomatal dynamic properties such as aspect ratio, circularity index and area of stomatal aperture were analyzed using multiple microscopic images in a given FOV (Fig. 2-19 and Fig. 2-20). Since, tomato leaf has a non-planar surface, the use of multiple microscopic images focused at different parts of the leaf in a given FOV provided an accurate result of stomatal dynamic properties. Status of lower epidermis stomata at 7:00 am and 11:30 am when the intensity of sunlight was 3,500 lux and 62,000 lux respectively are shown in Fig. 2-19. When SLI on the leaf was low, stomata had a sub-micrometre opening. However, at high SLI, stomata were wide open. Observation of stomatal opening at regular intervals was conducted throughout the day and stomatal dynamic properties were quantified after measurement of stomatal opening. Since, stomatal opening is a function of the SLI falling on the leaf instead of ambient SLI, average stomatal opening (n=26) did not reach its maximum value ($\sim 71 \mu\text{m}^2$) till 11:00 am even though ambient SLI (66,000 lux) was enough for maximum opening of stomata (Fig. 2-19B). A value of SLI on a leaf close to 15,000 lux was enough to have a wide opening of stomata. SLI higher than $\sim 15,000$ lux did not change stomata opening significantly although a fluctuation on stomatal opening has been observed at higher SLI on the leaf. However, latency has been observed in the change of stomatal opening in

response to a change in SLI. Factors other than SLI such as type of plant, plant and leaf age, location of the leaf, ambient temperature, wind speed, atmospheric carbon dioxide etc., which also affect the stomatal opening, are not discussed here. CL1, CL2 and CL3 represent the clouds at different times, responsible for the reduction in maximum SLI inside greenhouse and SLI falling on the leaf. Further, an average aspect ratio of the stomatal opening (a ratio between the major axis and minor axis) together with the average stomatal opening was studied (Fig. 2-20B). It was observed that the aspect ratio of the stomatal opening decreases with increasing the stomatal opening area and vice versa (Fig. 2-20C). Only open stomata were considered for statistical analysis of aspect ratio since for closed stomata, aspect ratio will be a non-defined (0/0) mathematical expression. In addition to the aspect ratio, circularity index (CI, 4π (area/perimeter²), a measurement of roundness was also quantified. A maximum value 1.0 of CI represents the perfect circle; however, minimum value 0.0 represents the infinitely elongated object. During daytime shape of the stomatal opening was close to a circular shape however, in morning and evening when stomata start to open/close, CI index had a minimum value.

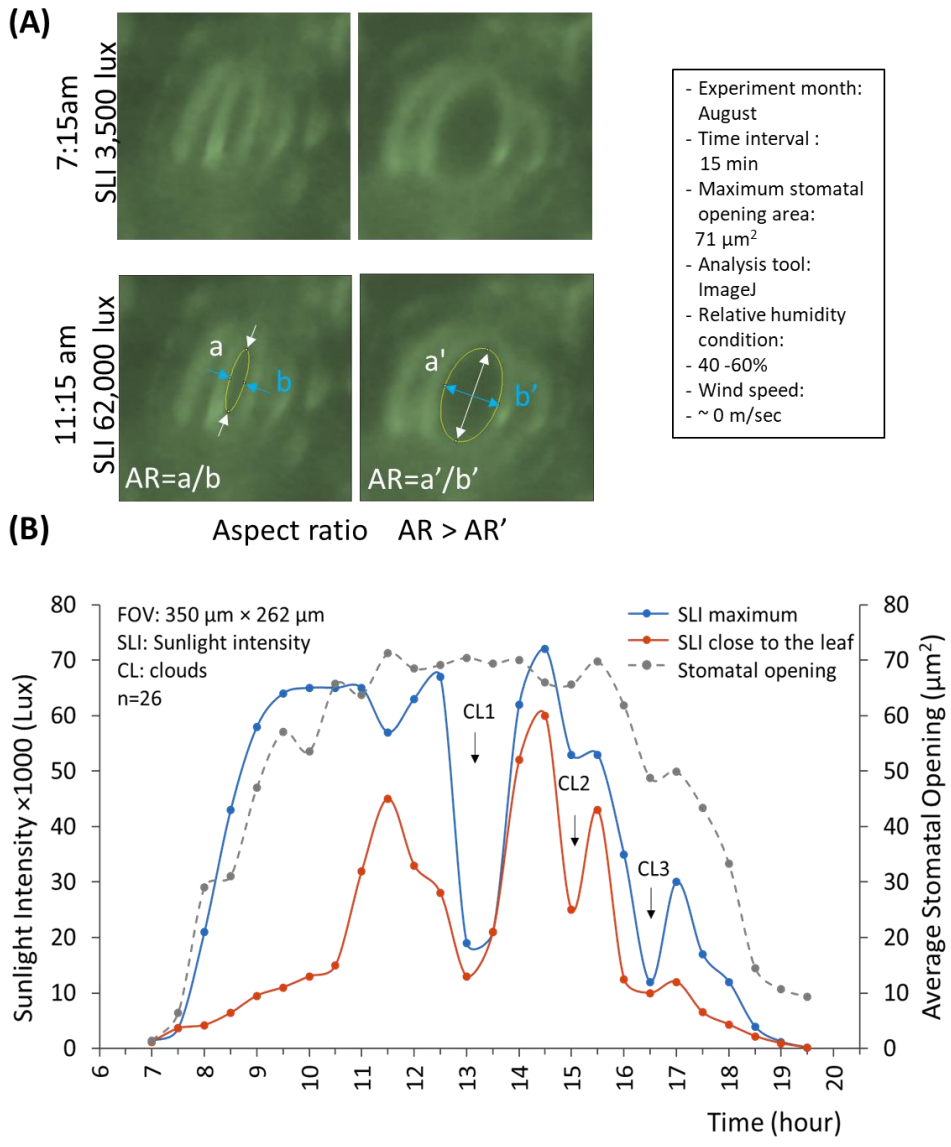
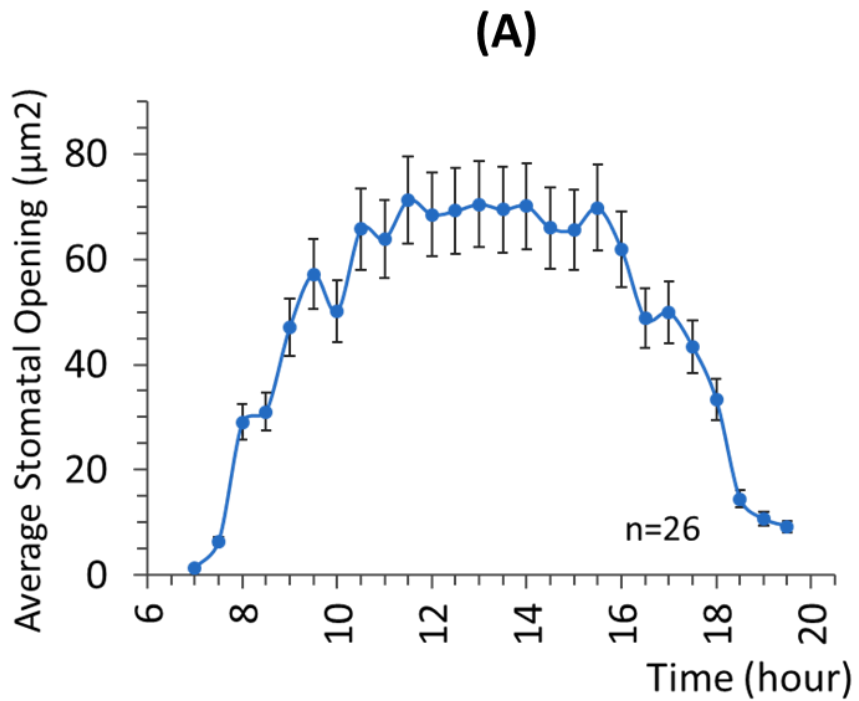
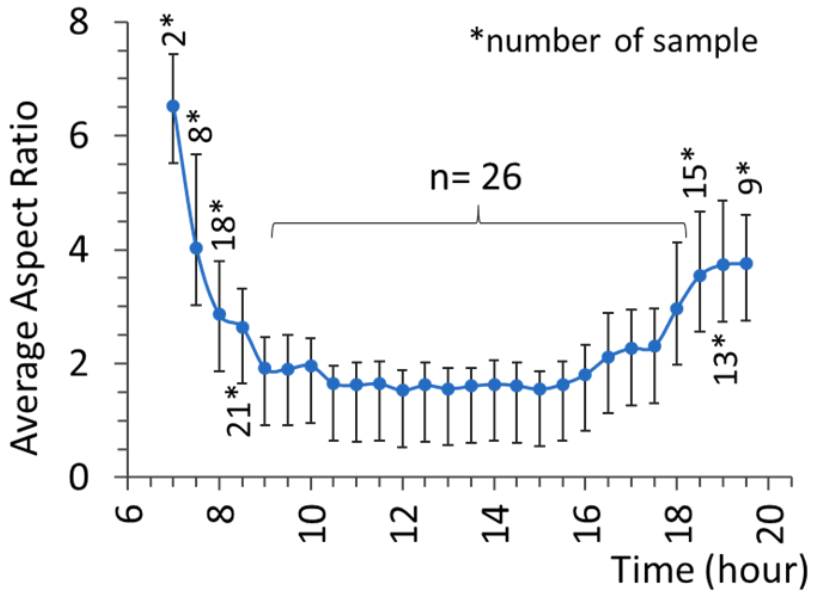


Fig. 2-19. Stoma opening status and measurement of geometrical features of stomata. (A) microscopic images at 7:30 am (partially open) and 11:30 am (completely open) when SLI on the leaf was 4,600 lux and 45,000 lux respectively. (B) Time wise mapping of stomatal opening/closing as a function of SLI on a sunny/cloudy day. Stomatal opening reached close to the maximum when SLI on a leaf was more than ~15,000 lux. The average opening area remained to be similar through the day until SLI value on a leaf was more than ~15,000 lux. Time wise, average stomatal opening

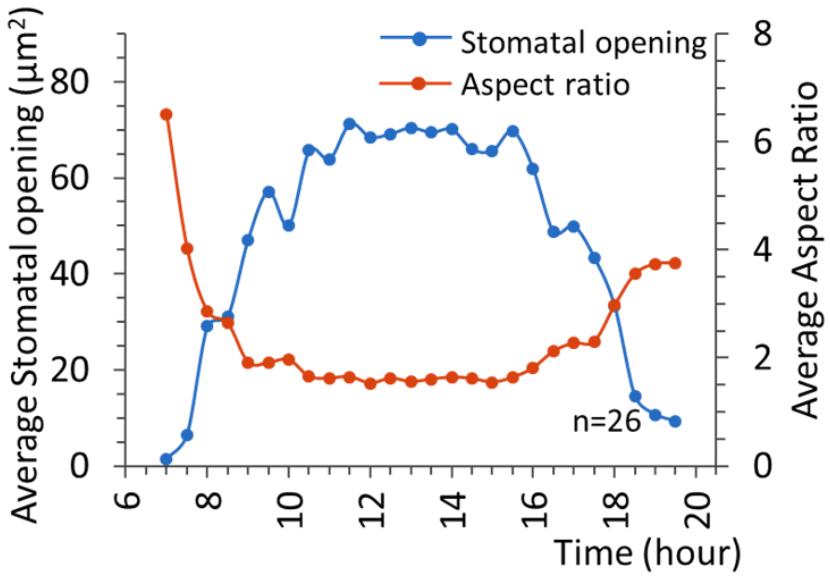
measurement. All stomata (n=26) in microscopic FOV (350 $\mu\text{m} \times 262 \mu\text{m}$) were considered. For closed stomata, zero opening area was used for calculation of average stomatal area and standard deviation.



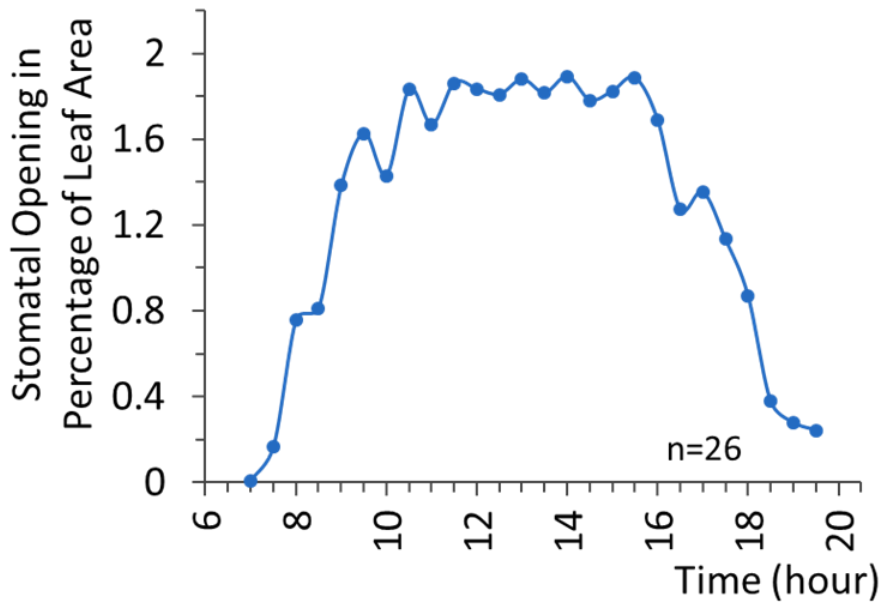
(B)



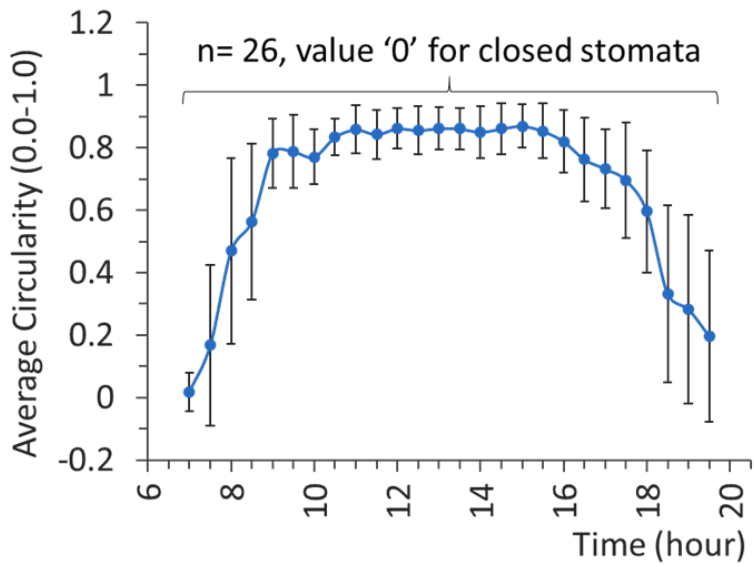
(C)

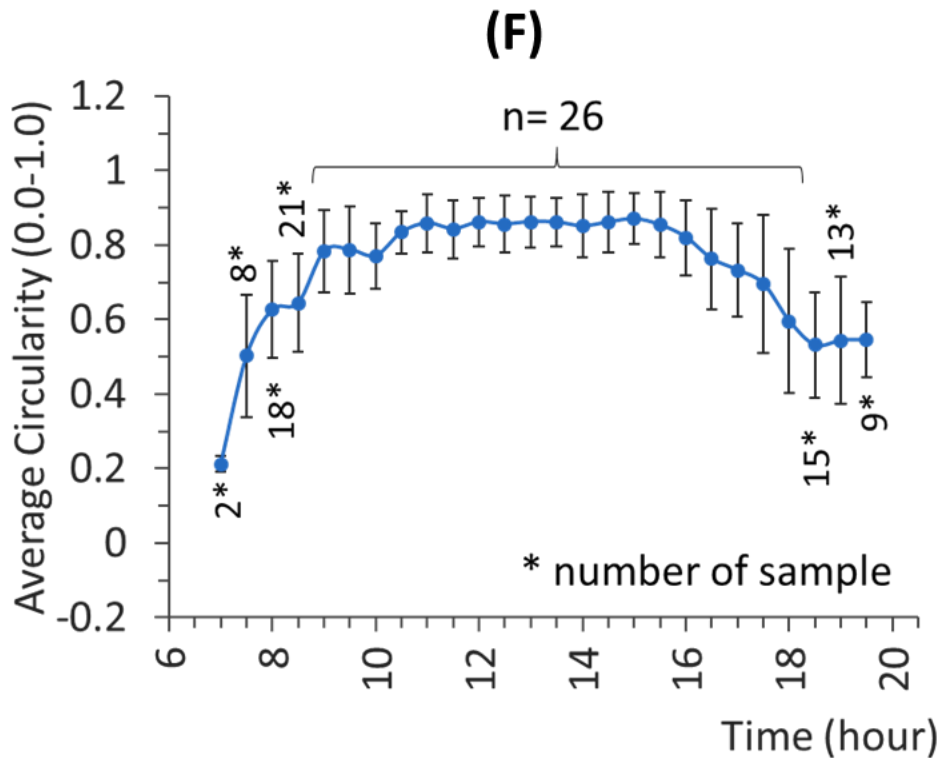


(D)



(E)





Aspect ratio= major axis/minor axis
 Circularity = 4π (area/perimeter²); 1.0 for a circle and 0.0 for infinitely elongated shape

Note: Large deviations in morning and evening hours as shown in Figure 2-19 E, indicate the asynchronous opening and closing of stomata in respective time. All open and closed stomata were taken into the consideration during statistical analysis. A value '0' is used for closed stomata in the analysis of average circularity of stomatal opening

Fig. 2-20. Average stomatal opening, total stomatal opening and average aspect ratio of a leaf (A) Average stomatal opening and total stomatal opening in the percentage of leaf area. Stomata start to open before the sunlight intensity reaches 10,000 lux. 20,000 lux SLI is sufficient to open the stomata completely. On average maximum stomatal opening area was $\sim 75 \mu\text{m}^2$. However, the stomatal opening area may change according to the leaf and plant age. Total stomatal opening area was $\sim 2\%$ to the leaf area. (B) Timewise measurement of average aspect ratio. Only open stomata were considered at the time of quantification. A declining and increasing trend in the value of aspect ratio was observed during opening and closing of stomata respectively. (C)

Simultaneous representation of average stomata opening and aspect ratio. (D) Real-time monitoring of total stomatal opening in the percentage of leaf area. Circularity measurement of stomata (E) when all stomata (n=26) were considered for statistical analysis (zero value for closed stomata) (F) and only open stomata were considered.

Bibliography

Afzal, A., S. W. Duiker, J. E. Watson and D. Luthe (2017). "Leaf thickness and electrical capacitance as measures of plant water status." Transactions of the ASABE **60**(4): 1063-1074.

Andrés, Z., J. Pérez-Hormaeche, E. O. Leidi, K. Schlücking, L. Steinhorst, D. H. McLachlan, K. Schumacher, A. M. Hetherington, J. Kudla, B. Cubero and J. M. Pardo (2014). "Control of vacuolar dynamics and regulation of stomatal aperture by tonoplast potassium uptake." Proceeding of the National Academy of Sciences **111**(17): E1806-E1814.

Assmann, S. M. (1988). "Enhancement of the stomatal response to blue light by red light, reduced intercellular concentrations of CO₂, and low vapor pressure differences." Plant Physiology **87**(1): 226-231.

Chandrasekhar, S. and G. Münch (1946). "The continuous spectrum of the sun and the stars." Astrophysical Journal **104**: 12.

Craparo, A. C. W., K. Steppe, P. J. A. Van Asten, P. Läderach, L. T. P. Jassogne and S. W. Grab (2017). "Application of thermography for monitoring stomatal conductance of Coffea arabica under different shading systems." Science of The Total Environment **609**: 755-763.

Devireddy, A. R., S. I. Zandalinas, A. Gómez-Cadenas, E. Blumwald and R. Mittler (2018). "Coordinating the overall stomatal response of plants: Rapid leaf-to-leaf communication during light stress." Science Signaling **11**(518): eaam9514.

Eisele, J. F., F. Fäßler, P. F. Bürgel and C. Chaban (2016). "A rapid and simple method for microscopy-based stomata analyses." PLOS ONE **11**(10): e0164576.

Gautam, R., R. D. Singh, V. P. Sharma, R. Siddhartha, P. Chand and R. Kumar (2012). "Biocompatibility of polymethylmethacrylate resins used in dentistry." Journal of Biomedical Materials Research **100B**(5): 1444-1450.

Grant, O. M., M. M. Chaves and H. G. Jones (2006). "Optimizing thermal imaging as a technique for detecting stomatal closure induced by drought stress under greenhouse conditions." Physiologia Plantarum **127**(3): 507-518.

Gray, J. and G. J. Peirce (1919). "The influence of light upon the action of stomata and its relation to the transpiration of certain grains." American Journal of Botany **6**(4): 131-155.

Gray, J. and G. J. Peirce (1919). "The influence of light upon the action of stomata and its relation to the transpiration of certain grains." American Journal of Botany **6**(4): 25.

Hessen, D. O. (2008). "Solar radiation and the evolution of life " The Norwegian Academy of Science and Letters: 14.

Hetherington, A. M. and F. I. Woodward (2003). "The role of stomata in sensing and driving environmental change." Nature **424**: 901.

Higaki, T. (2015). "Real-time imaging of plant cell surface dynamics with variable-angle epifluorescence microscopy." Journal of Visualized Experiments : JoVE(106): e53437-e53437.

Hogewoning, S. W., P. Douwstra, G. Trouwborst, W. van Ieperen and J. Harbinson (2010). "An artificial solar spectrum substantially alters plant development compared with usual climate room irradiance spectra." Journal of Experimental Botany **61**(5): 1267-1276.

Hollick, E. J., D. J. Spalton, P. G. Ursell and M. V. Pande (1998). "Biocompatibility of poly(methyl methacrylate), silicone, and AcrySof intraocular lenses: Randomized comparison of the cellular reaction on the anterior lens surface." Journal of Cataract & Refractive Surgery **24**(3): 361-366.

Hunt, S. (2003). "Measurements of photosynthesis and respiration in plants." Physiologia Plantarum **117**(3): 314-325.

Jayakody, H., S. Liu, M. Whitty and P. J. P. M. Petrie (2017). "Microscope image based fully automated stomata detection and pore measurement method for grapevines." Plant Methods **13**(1): 94.

Jones, H. G., M. Stoll, T. Santos, C. de Sousa, M. M. Chaves and O. M. Grant (2002). "Use of infrared thermography for monitoring stomatal closure in the field: application to grapevine." Journal of Experimental Botany **53**(378): 2249-2260.

Koman, V. B., T. T. S. Lew, M. H. Wong, S.-Y. Kwak, J. P. Giraldo and M. S. Strano (2017). "Persistent drought monitoring using a microfluidic-printed electro-mechanical sensor of stomata in planta." Lab on a Chip **17**(23): 4015-4024.

Lawson, T., W. James and J. Weyers (1998). "A surrogate measure of stomatal aperture." Journal of Experimental Botany **49**(325): 1397-1403.

Leinonen, I., O. M. Grant, C. P. P. Tagliavia, M. M. Chaves and H. G. Jones (2006). "Estimating stomatal conductance with thermal imagery." Plant, Cell and Environment **29**(8): 1508-1518.

Meckel, T., L. Gall, S. Semrau, U. Homann and G. Thiel (2007). "Guard cells elongate: relationship of volume and surface area during stomatal movement." Biophysical journal **92**(3): 1072-1080.

Meidner, H. and T. A. Mansfield (1968). Physiology of stomata, McGraw-Hill.

Omasa, K. and M. Onoe (1984). "Measurement of stomatal aperture by digital image processing." Plant and Cell Physiology **25**(8): 1379-1388.

Orsini, F., M. Alnayef, S. Bona, A. Maggio and G. Gianquinto (2012). "Low stomatal density and reduced transpiration facilitate strawberry adaptation to salinity." Environmental and Experimental Botany **81**: 1-10.

Pathan, A. K., J. Bond and R. E. Gaskin (2010). "Sample preparation for SEM of plant surfaces." Materials Today **12**: 32-43.

Purwar, P., S. Han, Y. Lee, B. Saha, T. Sandhan and J. Lee (2019). "High-resolution cost-effective compact portable inverted light microscope." Journal of Microscopy **273**(3): 199-209.

Raven, J. A. (2002). "Selection pressures on stomatal evolution." **153**(3): 371-386.

Renard, C. and W. Demessemacker (1983). "Effects of wind velocity on stomatal conductance and consequences of leaf rolling on water uptake in tall fescue." Biologia Plantarum **25**(6): 408-411.

Royer, D. L. (2001). "Stomatal density and stomatal index as indicators of paleoatmospheric CO₂ concentration." Review of Palaeobotany and Palynology **114**(1): 1-28.

Savaris, M., G. L. Braga, V. dos Santos, G. A. Carvalho, A. Falavigna, D. C. Machado, C. Viezzer and R. N. Brandalise (2017). "Biocompatibility assessment of poly(lactic acid) films after sterilization with ethylene oxide in histological study in vivo with wistar rats and cellular adhesion of fibroblasts in vitro." International Journal of Polymer Science **2017**: 9.

Seo, M., D.-H. Park, C. W. Lee, J. Jaworski and J.-M. Kim (2016). "Fluorometric measurement of individual stomata activity and transpiration via a "brush-on", water-responsive polymer." Scientific Reports **6**: 32394.

Smith, S., J. D. B. Weyers and W. G. Berry (1989). "Variation in stomatal characteristics over the lower surface of *Commelina communis* leaves." Plant, Cell and Environment **12**(6): 653-659.

Tsoua, C.-H., B.-J. Kao, M.-C. Yang, M.-C. Suen, Y.-H. Lee, J.-C. Chen, W.-H. Yao, S.-M. Lin, C.-Y. Tsou, S.-H. Huang, M. D. Guzman and W.-S. Hungb (2015). "Biocompatibility and characterization of polylactic acid/styrene-ethylene-butylstyrene composites." Bio-Medical Materias and Engineering **26**: 8.

Weyers, J. D. B. and H. Meidner (1990). Methods in stomatal research, Longman Scientific & Technical.

Wild, A. and G. Wolf (1980). "The effect of different light intensities on the frequency and size of stomata, the size of cells, the number, size and chlorophyll content of chloroplasts in the mesophyll and the guard cells during the ontogeny of primary leaves of *Sinapis alba*." Zeitschrift für Pflanzenphysiologie **97**(4): 325-342.

Willmer, C. and M. Fricker (1996). Stomata, Chapman & Hall.

Willmer, C. M. and L. N. J. P. Beattie (1978). "Cellular osmotic phenomena during stomatal movements of *Commelina communis*." Protoplasma **95**(4): 321-332.

Wu, H.-C., Y.-C. Huang, C.-H. Liu and T.-L. Jinn (2017). "Using Silicon Polymer Impression Technique and Scanning Electron Microscopy to Measure Stomatal Aperture, Morphology, and Density." Bio-protocol **7**(16): e2449.

Xu, Z. and G. Zhou (2008). "Responses of leaf stomatal density to water status and its relationship with photosynthesis in a grass." Journal of Experimental Botany **59**(12): 3317-3325.

Chapter 3

Design and development of high-resolution portable transmitted optical microscope

Contents

- 3.1 Optical microscope
- 3.2 Literature survey
- 3.3 Compact transmitted optical microscope
 - 3.3.1 Design and development
 - 3.3.2 Optical resolution and field of view
 - 3.3.3 Imaging of a micrometer object and image enhancement
- 3.4 Applications of portable inverted microscope
 - 3.4.1 Sub-micrometer scale imaging
 - 3.4.2 High-speed microscopy: Imaging of high-speed droplets generation
 - 3.4.3 Live imaging of eukaryotic cells
 - 3.4.4 Industrial applications: high-resolution real-time monitoring of a sample at a bulky apparatus
 - 3.4.5 Industrial applications: optical inspection of micropatterns fabricated in a clean room

Bibliography

3.1 Optical microscope

The optical microscope, often referred to as the light microscope, is a type of microscope that commonly uses visible light (400 -700 nm) and a system of lenses to magnify images of small objects. Optical microscopes are the oldest

design of microscope and were possibly invented in their present compound form in the 17th century. System of optical microscopes contain simple optical element to complex optical elements based on the required resolution, contrast, cost, applications etc. However, the optical resolution of these microscopes are limited by diffraction of the light. An optical resolution close to 200 nm can be obtained by optical microscopes without post processing of the image obtained by these microscopes.

3.2 Literature survey

High-performance standard optical microscopes can be used to obtain high-quality images; however, these microscopes are expensive, bulky, and limited by the small field of view (FOV) (Thorn 2016) (refer Fig. 3-1). Moreover, owing to portability and cost issues, these microscopes are not suitable for several applications such as point-of-care devices, direct imaging of a sample in a large apparatus, remote location applications, resource limited areas, etc. In recent years, there has been a progress in the development of cost-effective and portable microscopes; however, most of these methods are limited by the sample conditions and/or requirement of a complex computation to obtain the final image of an object. Digital in-line holography (Gabor 1948, Xu, Jericho et al. 2001, Kanka, Riesenber et al. 2011), contact imaging microscopy (Zheng, Lee et al. 2011, Greenbaum, Luo et al. 2012, Kim, Bae et al. 2012), and optofluidic microscopy (Heng, Erickson et al. 2006) are examples of lens-

free-imaging-based cost-effective portable microscopic techniques (refer Fig. 3-2). In digital in-line holography, an interference pattern of the scattered wave (from an object) and reference wave (from a coherent light source) is recorded and further processed to reconstruct the image of an object. However, this method requires expensive hardware to process the data in real-time, and it is not suitable for confluent samples. Contact lens-free-imaging-based microscopes provide portability and large FOV with a submicron-level resolution. However, this technology requires complex computations to reconstruct the image from diffraction patterns. Furthermore, it is limited by the sample cleanliness, close proximity of the sample to the image sensor, and low-speed imaging. With an optofluidic microscope, only suspended samples translating at a known velocity without rotation can be imaged. This technique is not suitable for stationary objects such as biological samples on a glass slide and suspended rotating samples. Moreover, the sample preparation requires a nanoscale precise fabrication.



Image source: www.nikon.com

Fig. 3-1. Conventional inverted microscope (Nikon Ti Eclipse)

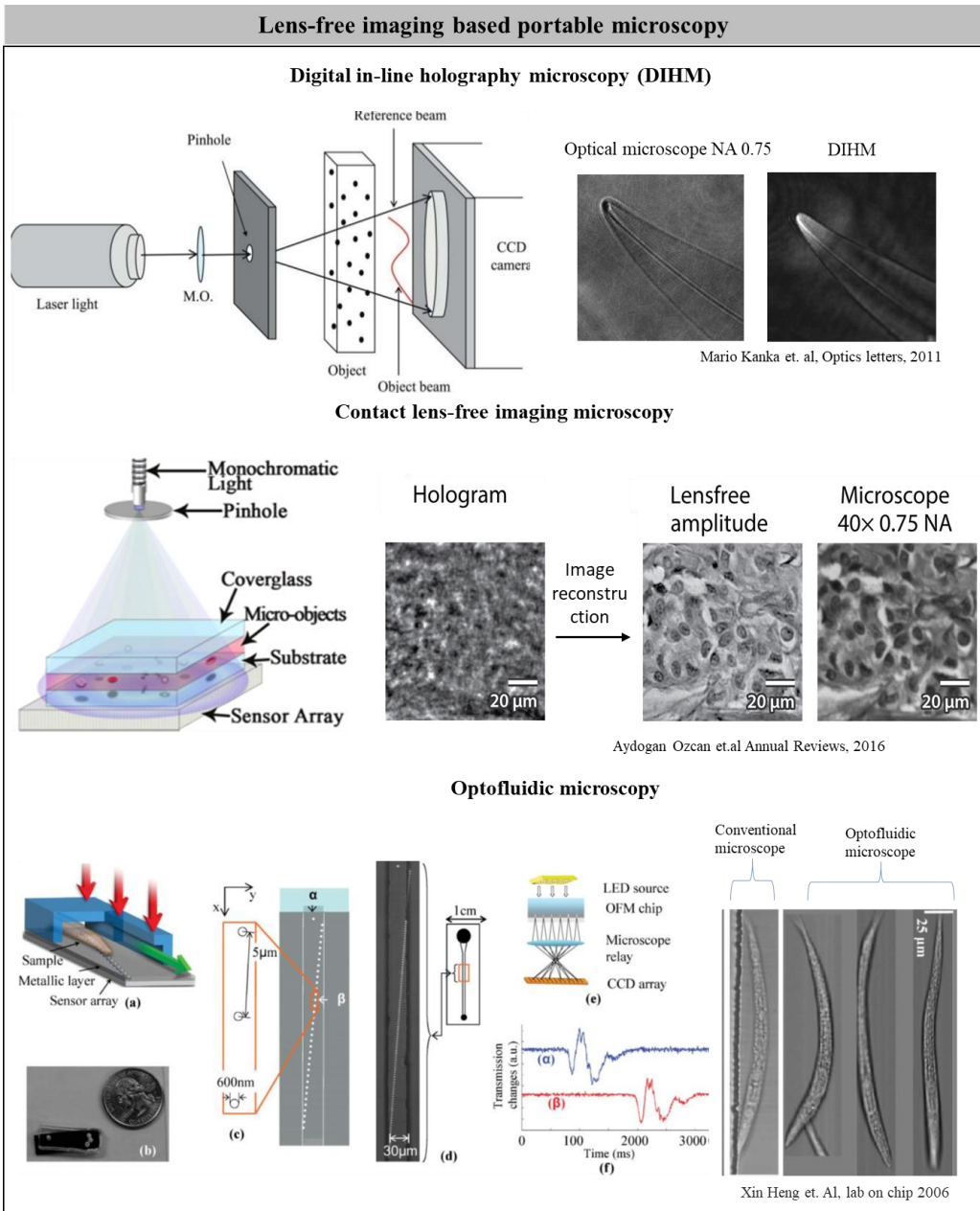


Fig. 3-2. Lens-free-imaging-based portable microscopes

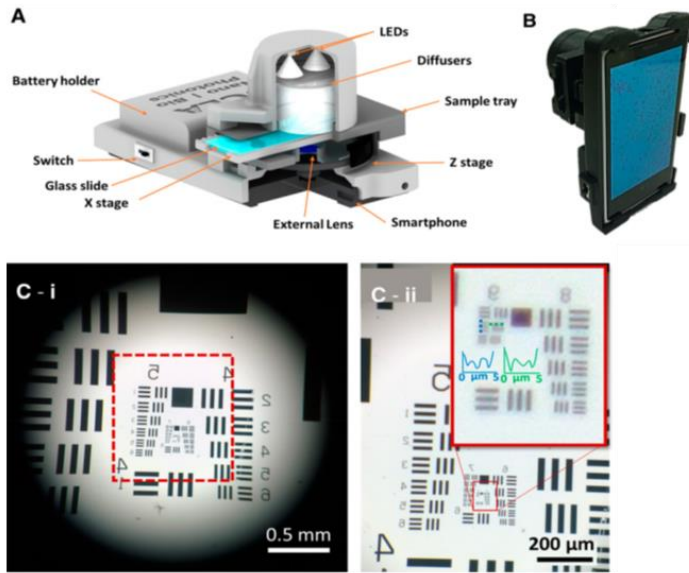
In addition to the lens-free imaging, origami-based paper microscope (Cybulski, Clements et al. 2014) and smartphone-based microscope (Dong, Guo et al. 2014) (Bogoch, Koydemir et al. 2017) are good examples of lens-based portable microscopes (refer Fig. 3-3). Even though the origami-based paper microscope is an ultra-low-cost portable microscope with bright-field, dark-field, and fluorescence imaging capabilities, it does not have a digital recording facility and it is useful only for specific applications. The smartphone-based microscope utilizes the lens of a smartphone camera in a reverse manner or an extra condenser lens to magnify the object; however, the use of lens of a smartphone in a reverse manner requires complex image processing computations to obtain a clear magnified image of an object. On the other hand, a portable microscope (Bogoch, Koydemir et al. 2017) having an extra condenser lens was suitable only for the samples on a glass slide and the full-pitch spatial resolution was limited close to two μm .

In this study, we demonstrate a novel simple technique for a cost-effective compact portable customizable submicron-resolution inverted light microscope and its applications in various field. Moreover, our technique does not require complex computations to obtain the final image of an object. In the proposed technique, we directly use a commercial microscope objective lens close to an image sensor for compactness of the microscope. The use of few optical components reduces the optical attenuation and imperfection in the

image formation owing to inaccurate optical systems, which helps to obtain a sharp image of an object. In addition, this technique can be customized for specific applications such as high-speed imaging, live cell monitoring inside an incubator, real-time monitoring of the effect of physical forces on a sample in a large apparatus, micro-to-nanoscale measurement and inspection of a sample at industrial processes, etc.

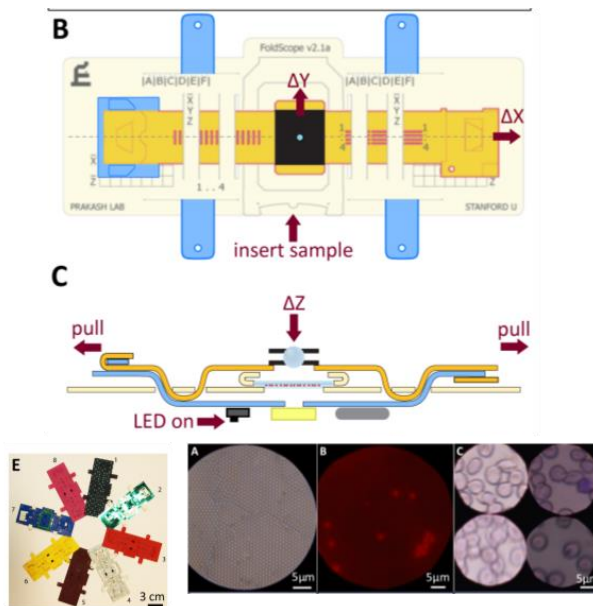
Lens-based portable microscopy

Smartphone-based-microscope



Isaac I. Bogoch et. al, Am. J. Trop. Med. Hyg., 2017

Foldscope



James S. Cybulski et. al, PLOS one, 2014

Fig. 3-3. Lens-based portable microscopes

Table 3-1 Comparison of portable inverted microscopes

Methods	Microscopic technique	Resolution	Image reconstruction	Cost	Field of view Compared to the standard microscope	Sample type
Lens-free imaging	Digital in-line holography microscopy	400-500 nm	Required	High	Depend upon the sensor size	Microscope slide (stationary)
Lens-free imaging	Contact lens-free imaging microscopy	400-500 nm	Required	Low	Depend upon the sensor size	Microscope slide (stationary)
Lens-free imaging	Optofluidic microscopy	490 nm	Required	High	Depend upon the fabrication	Movable sample
Lens-based imaging	Smartphone-based microscope	870 nm	Required	Low	Moderate	Microscope slide (stationary and movable)
Lens-based imaging	Foldscope	1380 nm	Not required	Very low	Low	Microscope slide
Lens-based imaging	Our method	488 nm	Not Required	Low	Moderate	All samples

3.3 Portable transmitted microscope

3.3.1 Design and development

A schematic and experimental setup of the novel high-resolution microscopic technique are shown in Fig. 3-4. Microscope consists of a commercial microscope finite objective lens, image sensor, and light-emitting diode (LED) based light source. The image sensor is placed close to the microscope lens for compactness of the microscopic setup. In order to optically align the light source, lens, and image sensor, the lens is placed at the center of the image sensor and the light source is mounted on the lens using three-dimensional (3D) printed structures (Fig. 3-4). The light source consists of a 460-nm surface-mounted LED and two aspherical condenser lenses with and without a diffuser surface (\O : 25 mm, focal length: 20 mm, numerical aperture (NA): 0.6). Two microscope finite objective lenses (Bimeince Korea) with 20 \times (NA: 0.4) and 40 \times (NA: 0.6) optical magnification (OM) and four images sensors with specifications presented in Table 3-2 were used. NA value of condenser lens was equal or more than of NA value of used objective lens. Objective lenses with OM below 20 \times magnification were unable to provide a high resolution, though they were suitable to simultaneously observe multiple large objects. The objective lenses with OM above 40 \times provided less sharp images (60 \times objective lens) or required an oil immersion (100 \times objective lens) for microscopy, which limits them for industrial applications. The image sensors

were selected based on the pixel size (for resolution), image sensor size (for FOV), and capability for a high-speed imaging as mentioned in table 2-1. Image sensors are denoted as sensor ‘1’, sensor ‘2’, sensor ‘3’, and sensor ‘4’ in this study.

Table 3-2. Specifications of image sensors used in experiment

Sensor	Type	Size	Pixels	Pixel size
Sensor ‘1’	1/4 inch	2.87 mm × 2.15 mm	2048 × 1536	1.4 μm × 1.4 μm
Sensor ‘2’	1/2.3 inch	6.47 mm × 4.62 mm	3872 × 2764	1.67 μm × 1.67 μm
Sensor ‘3’	1/3 inch	4.80 mm × 3.60 mm	1600 × 1200	3 μm × 3 μm
Sensor ‘4’*	4/3 inch	17.60 mm × 13.20 mm	800 × 600	22 μm × 22 μm

* High-speed camera image sensor (Phantom Miro eX4).

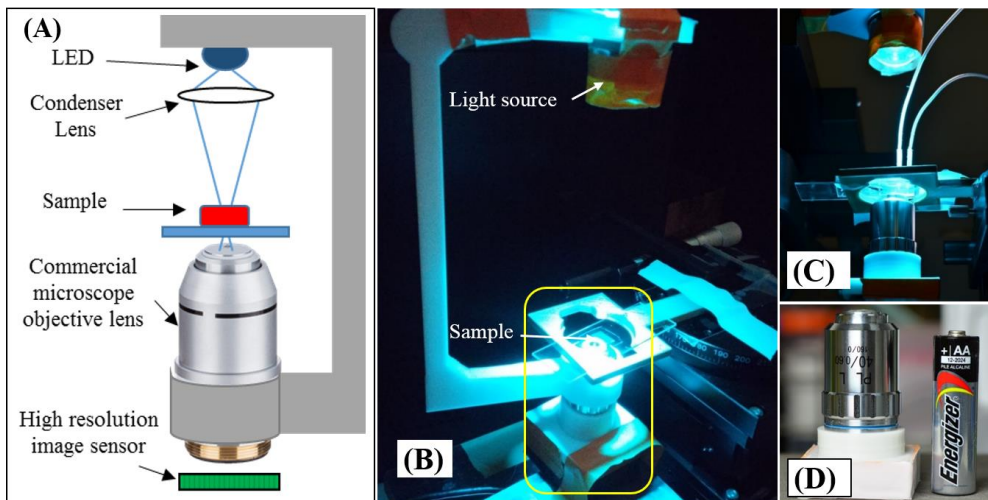


Fig. 3-4. Schematic, experimental setup, and dimension comparison of portable transmitted microscope. (A) Schematic of the portable customizable high-resolution

microscope. (B) LED-based light source fitted on the lens and optically aligned with the lens and image sensor. Yellow colour rectangle shows the total size of the microscope without the light source (C) Microfluidic application: imaging of a high-speed water droplet generation in oil. (D) Size comparison between our microscope (without any light source) and AA size battery.

3.3.2 Optical resolution (OR)

Optical resolution (OR, lateral resolution) describes the distance between two distinguishable radiating points. Theoretically, the OR for an objective lens is given by

$$OR = \lambda / (2NA)$$

Where λ is the wavelength of the light and NA is the numerical aperture of the objective lens (Akin, Li et al. 2004, Wang and Chang 2011). For example, a theoretical value of optical resolution for a microscope using 40× objective lens having NA 0.6 should be 467 nm when 460 nm blue colour light source is used. Increase in λ value in case of white light source, decreased the OR. Although image sensor with small size pixel provides the better OR, yet OR was limited due to theoretical limit and diffraction of the light source.

An extreme 1951 USAF microscope resolution target (Amazon.com) with a smallest half-pitch spatial resolution (HSR) of 0.137 μm was used to measure the optical resolution (OR) in terms of full-pitch spatial resolution

(FSR) and HSR of our microscopic setup under blue (460 nm) and white light source (Fig. 3-5). Resolution target contains 100 nm thick three equidistant vertical and horizontal direction chrome bars of different HSR values increasing in width by ~12.4 % of the previous value (HSR value: 0.137 μm to 31.250 μm) plated on quartz background.

Sensor '1' (pixel size 1.4 $\mu\text{m} \times 1.4 \mu\text{m}$) and sensor '3' (pixel size 3 $\mu\text{m} \times 3 \mu\text{m}$) provided the FSR value of 0.976 μm (HSR: 0.488 μm , FOV 425 $\mu\text{m} \times 318 \mu\text{m}$) and 1.23 μm (HSR: 0.615 μm , FOV 632 $\mu\text{m} \times 474 \mu\text{m}$) respectively when the resolution target was illuminated by blue light source with 40 \times objective lens (NA 0.6). However, under white light source (~380 nm-750nm spectrum) FSR value was limited to 1.55 (HSR: 0.775 μm , FOV 425 $\mu\text{m} \times 318 \mu\text{m}$) and 1.382 μm (HSR: 0.691 μm , FOV 632 $\mu\text{m} \times 474 \mu\text{m}$) for sensor '1' and '3' respectively. The values of HSR, FSR and FOV for sensor '1' and '3' with 40 \times (NA 0.6) and 20 \times (NA 0.4) objective lens when resolution target was illuminated with blue and white colour light source is mentioned in table 3-3. The light intensity on sensor '1' was not uniform due to the transparent glue, used at two different sides of the image sensor to protect the wired connections between image sensor and surrounding circuit.

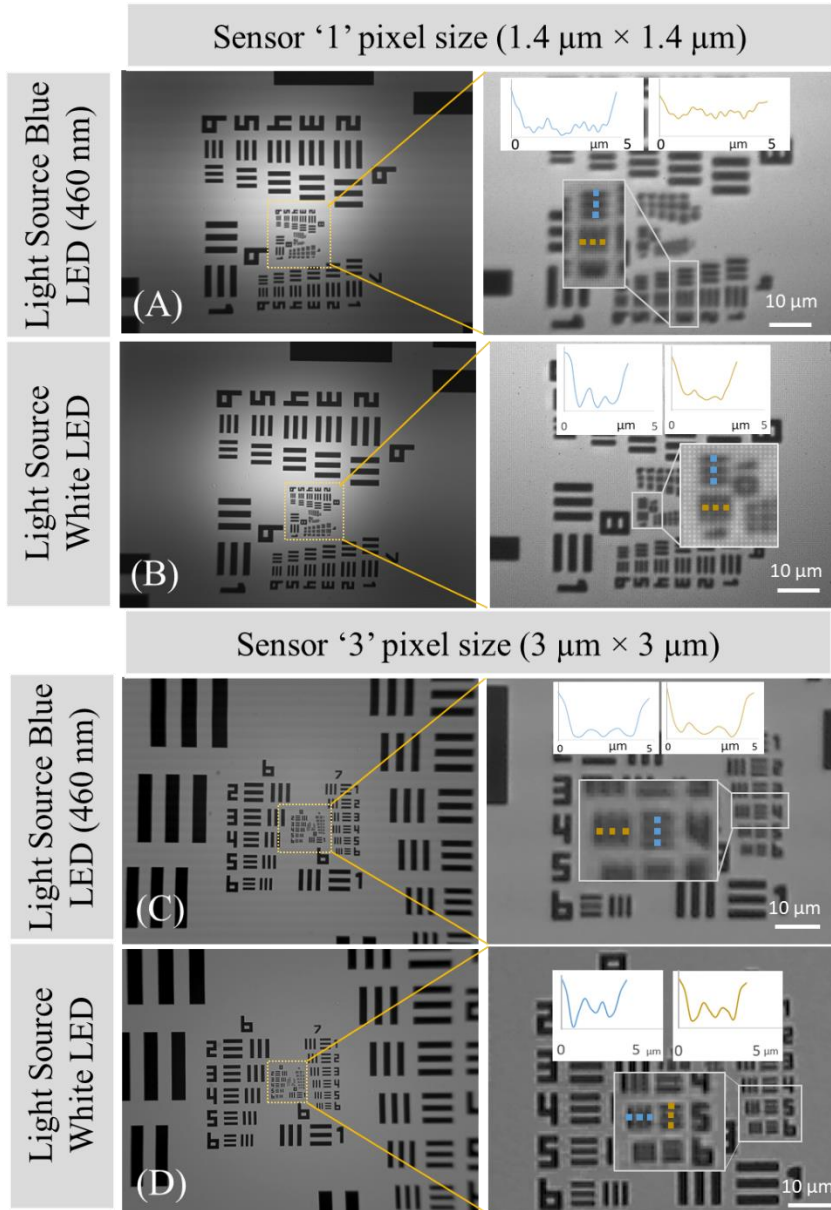


Fig. 3-5. Measurement of optical resolution and field of view (FOV) values for the microscopic setups. (A) Sensor '1' with 40 \times objective lens and blue LED based light source (460 nm); FSR 976 nm (HSR 488 nm), FOV 425 $\mu\text{m} \times$ 318 μm (B) Sensor '1' with 40 \times commercial objective lens and white LED based light source; FSR 1.550 μm (HSR 775 nm), FOV 425 $\mu\text{m} \times$ 318 μm (C) Sensor '3' with 40 \times objective lens and blue LED based light source (460 nm); FSR 1.23 μm (HSR 615 nm), FOV 632

$\mu\text{m} \times 474 \mu\text{m}$ (D) Sensor ‘3’ with 40 \times objective lens and white LED based light source; FSR 1.382 μm (HSR 691 nm), FOV 632 $\mu\text{m} \times 474 \mu\text{m}$.

Table 3-3. Half-pitch spatial resolution (HSR), full-pitch spatial resolution (FSR) and field of view (FOV) of microscopic setup observed under various combinations of the image sensors, objective lens and light sources

Objective Lens	Sensor (pixel size)	Light Source	HSR	FSR	FOV
40x	‘1’ (1.4 $\mu\text{m} \times 1.4 \mu\text{m}$)	Blue colour LED	0.488 μm	0.976 μm	425 $\mu\text{m} \times 318 \mu\text{m}$ (0.139 mm ²)
40x	‘1’ (1.4 $\mu\text{m} \times 1.4 \mu\text{m}$)	White colour LED	0.775 μm	1.550 μm	425 $\mu\text{m} \times 318 \mu\text{m}$ (0.139 mm ²)
40x	‘3’ (3.0 $\mu\text{m} \times 3.0 \mu\text{m}$)	Blue colour LED	0.615 μm	1.230 μm	632 $\mu\text{m} \times 474 \mu\text{m}$ (0.3 mm ²)
40x	‘3’ (3.0 $\mu\text{m} \times 3.0 \mu\text{m}$)	White colour LED	0.691 μm	1.382 μm	632 $\mu\text{m} \times 474 \mu\text{m}$ (0.3 mm ²)
20x	‘1’ (1.4 $\mu\text{m} \times 1.4 \mu\text{m}$)	Blue colour LED	1.096 μm	2.192 μm	1059 $\mu\text{m} \times 794 \mu\text{m}$ (0.84 mm ²)
20x	‘1’ (1.4 $\mu\text{m} \times 1.4 \mu\text{m}$)	White colour LED	1.380 μm	2.760 μm	1059 $\mu\text{m} \times 794 \mu\text{m}$ (0.84 mm ²)

20x	'3' (3.0 μm \times 3.0 μm)	Blue colour LED	1.380 μm	2.760 μm	1552 μm \times 1164 μm (1.8 mm ²)
20x	'3' (3.0 μm \times 3.0 μm)	White colour LED	1.550 μm	3.100 μm	1552 μm \times 1164 μm (1.8 mm ²)

3.3.3 Imaging of a micrometer object and image enhancement

The imaging of PDMS rectangular grid patterns (50 μm \times 20 μm) attached to a thin glass slide and image enhancement are shown in Fig. 3-6. The sensor '3' with a 40 \times objective lens was used for the imaging, as this combination provides a similar FOV (\sim 700 μm \times 525 μm) as that of a Nikon microscope (589 μm \times 471 μm) at a 200 \times magnification for a comparison of the image quality. The image quality obtained by our technique is comparable to that of the Nikon microscope. However, owing to the proximity of the image sensor to the lens, the edges of the image were less sharp for a focusing at the center. Two methodologies were applied to obtain a single sharp image.

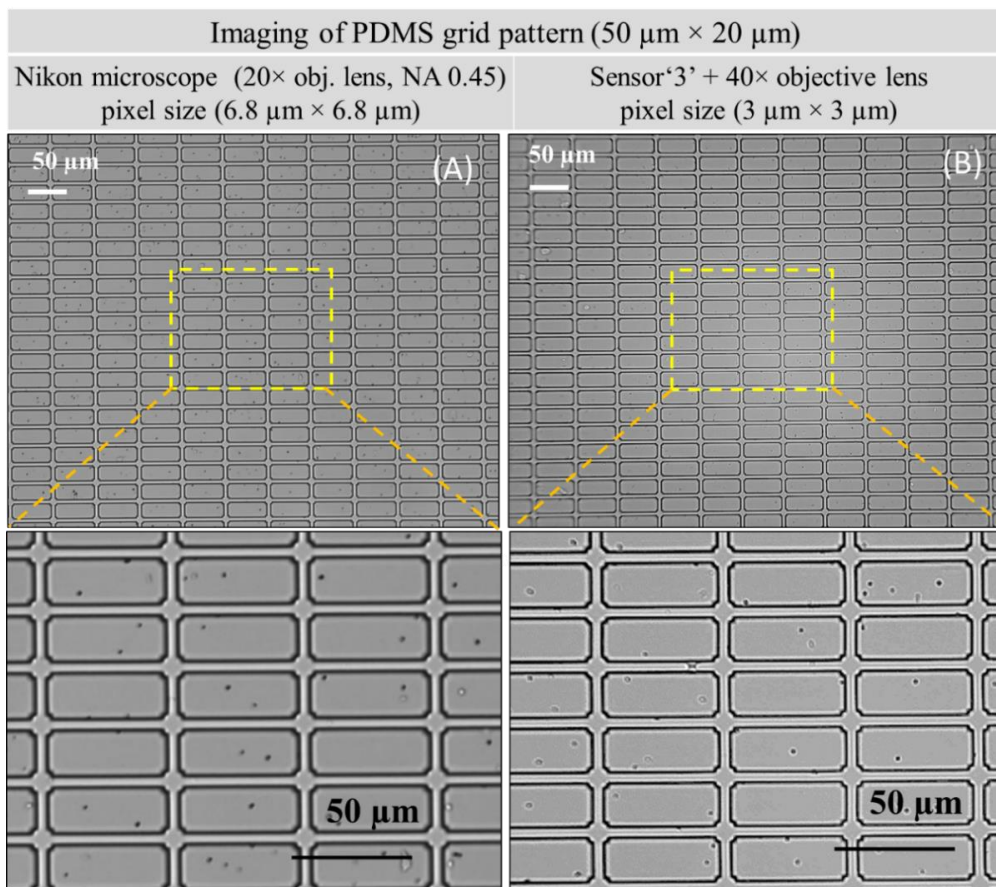


Fig. 3-6. Imaging of a microscale grid pattern. Comparison of the image qualities with a similar FOV for a (A) Nikon microscope ($20\times$ objective lens, NA0.45), FOV: $589\ \mu\text{m} \times 471\ \mu\text{m}$ and (B) sensor '3' with a $40\times$ objective lens, FOV: $\sim 700\ \mu\text{m} \times 525\ \mu\text{m}$.

Fabrication of PDMS rectangular patterns

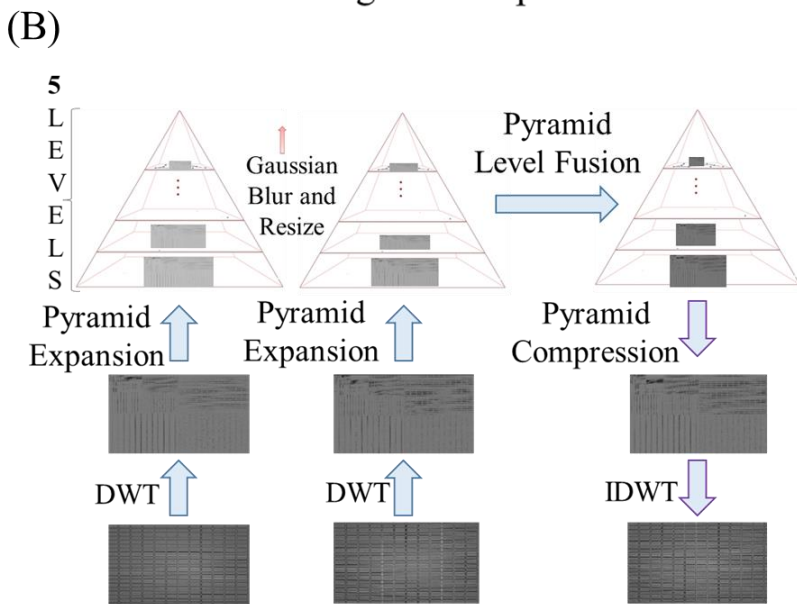
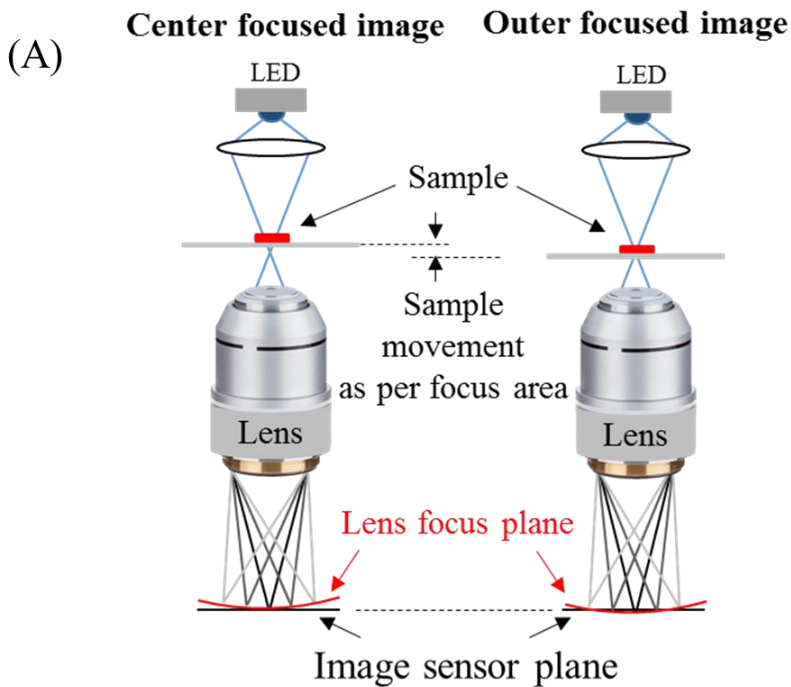
Polydimethylsiloxane (PDMS, Sylgard 184 Dow Corning USA) rectangular grid patterns were fabricated by a single-mask soft lithography process. A negative photoresist SU-8 (Microchem USA) was spin-coated on a 4-inch clean silicon wafer, followed by a standard lithography process to pattern a

mold. The degassed PDMS mixed at a ratio of 10:1 of monomer and curing agent was poured on the SU-8 mold wafer and cured at 70 °C for 2 h. Prior to the PDMS pouring, the SU-8 mold wafer was exposed to a silanizing agent (tridecafluoro-1,1,2,2-tetrahydrooctyl trichlorosilane) to aid the release of PDMS from the SU-8 mold wafer.

Multiple-images-fusion-based image enhancement

A single sharp image can be obtained by fusing multiple images at various foci. A merging of two images was sufficient to obtain a clear focused image. Two images of grid patterns, one focused at the center and the other one focused on the background (outward focus) were fused in the frequency domain using discrete wavelet transform (DWT) in a hierarchical manner (Laplacian pyramid), as shown in Fig. 3-7 (Wang and Chang 2011). Wavelets are very effective to represent isolated sharp objects such as microscale structures. The Laplacian pyramid utilized the global and local information of the scene. First, both images were decomposed into the discrete wavelet space of the Laplacian pyramid and then each pyramid level was fused in the wavelet domain. The fused pyramid was assembled back to the single transformed image, whose inverse DWT provided the final sharp image.

Multiple images fusion based image enhancement



Center focused image Outer focused image Focused sharp image

DWT: discrete wavelet transform, IDWT: Inverse discrete wavelet transform

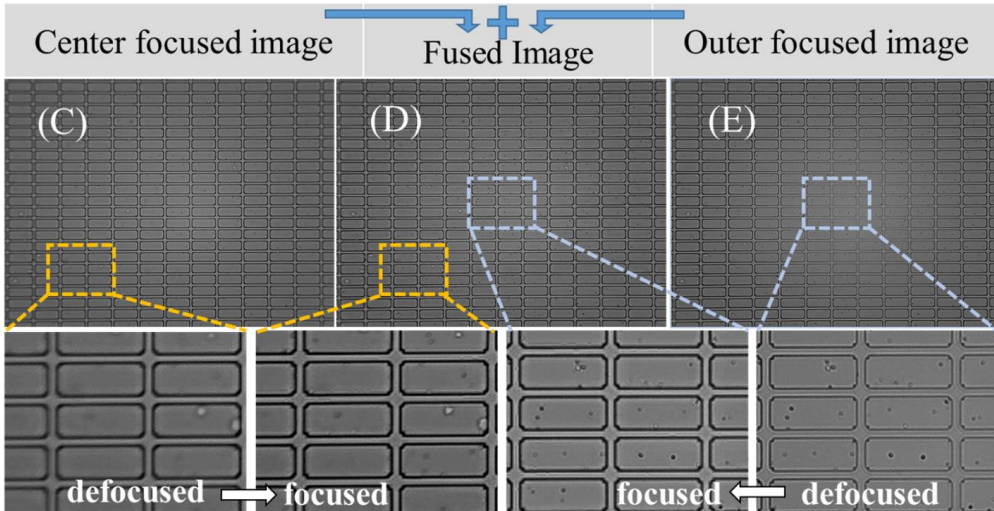


Fig. 3-7. Multiple-images-fusion-based image enhancement. (A) Schematic of the setup used to obtain the center- and outer-focused images. The sample is moved up and down to obtain an image focused at a particular area. (B) Block diagram of the DWT-based image enhancement. (C) Center- and (D) outer-focused images. (E) Image obtained after the fusion of the center- and outer-focused images.

Single-image-based enhancement

In observations of dynamic samples, it is challenging to record multiple images under the same conditions. Our microscopic system can precisely focus at the central part of the object; however, in such case, the boundary region of the image becomes out-of-focus. In general, the non-focused region, which is far away from the region of focus is not of significant interest. However, as the optical arrangement of our microscopic system is fixed, the blur pattern on the outer part of the image is also fixed. This boundary blur

can be removed through a post image processing. Therefore, for single image enhancement, a blind deblurring was performed in two steps: empirical estimation of the blur kernel and deconvolution of the estimated kernel with the input image as shown in Fig. 3-8 (Lai, Huang et al. 2016). The entire camera framework setting is fixed (e.g., the distance from the lens to the imaging plane and that from the object to the imaging plane are constant); therefore, once the blur kernel is estimated, only its variance is adjusted for each input image using the smoothness prior over the kernel. The kernel k is parameterized as a two-dimensional (2D) Gaussian function, with an assumed mean of zero and estimated variance; the kernel size is fixed to a 7×7 square. Therefore, the image Y is formed with an additive noise η as:

$$Y = k * X + \eta \quad (1)$$

$$k = \frac{1}{2\pi\sigma^2} \exp\left(-\frac{x^2+y^2}{2\sigma^2}\right) \quad (2)$$

where x and y are pixel indices in the kernel matrix k , $*$ is the convolution operator, and X is the underlying true high-quality image, which needs to be estimated using the empirically estimated kernel k in the presence of an unknown additive noise η . This deconvolution is an ill-posed problem; owing to its sensitivity to noise, there are many solutions that satisfy the above equation. This ill-posed problem has been solved in the literature using

additional image priors such as natural image statistics (Levin 2006), sparse image prior (Zhang, Wipf et al. 2013), Richardson–Lucy prior (Yongpan, Huajun et al. 2010), etc. We employed the sparse image prior in our study, as the microscopic images with a fixed background or substrate have sharp edges and piecewise constant regions. Therefore, the joint minimization problem (Cai, Hui et al. 2009) is formulated with smoothness and sparse regularizations on the blur kernel k and clear image X , respectively:

$$\underset{(X,k)}{\text{minimize}} \quad \|k * X - Y\|^2 + \lambda_1 \|k\|^2 + \lambda_2 |X| \quad (3)$$

where, $\|k * X - Y\|^2$ is the data fidelity term, $\lambda_1 \|k\|^2$ is the smoothness prior over the kernel, and $|X|$ is the sparse prior over the clear image; it is solved using iterative numerical methods (Fergus, Singh et al. 2006). The input image is already focused at the central region; therefore, in order to increase the speed and output-image quality, the refocusing optimization is applied only at the outer regions of the image. The image is chopped into m parts, each of them is enhanced using equation (3), and fused using the DWT-based Laplacian pyramid fusion technique (Wang and Chang 2011).

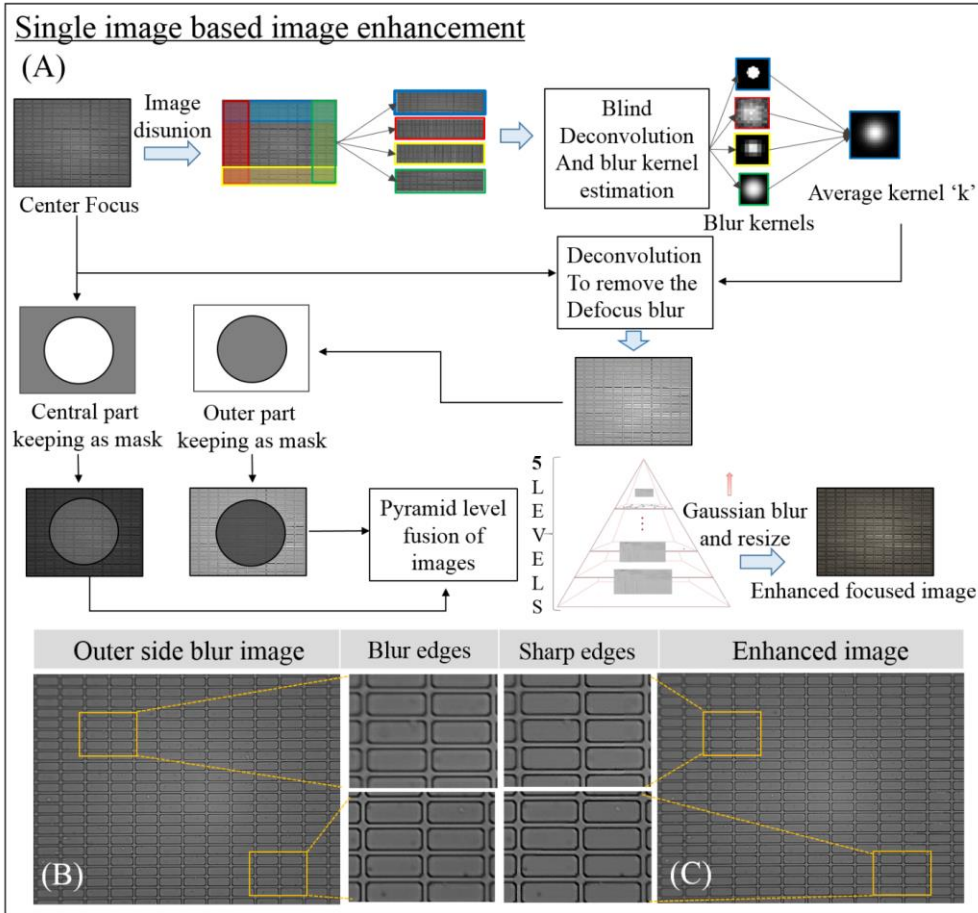


Fig. 3-8. Single-image-based image enhancement. (A) Block diagram of the kernel estimation and deconvolution-based image enhancement. (B) Center-focused image with an outer side blur. (C) Enhanced image with sharp edges at the outer side.

3.3.4 Effect of pixel size (of image sensor) on image quality and point spread function (PSF)

The point spread function (PSF) which describes the response of an imaging system (or, impulse response of a imaging system) to a point source or point object has been quantified for spherical shape 1 μm (in diameter) polystyrene beads as shown in Fig. 3-9. A schematic of star showing the effect of pixel size on image quality is shown. As the pixel size increases the information loss will increase and hence the image quality will decrease. As shown in Fig. 3-9, when the high-resolution image sensor (pixel size 1.4 $\mu\text{m} \times 1.4 \mu\text{m}$) has been used in our microscopic, the image quality of polystyrene has been improved. The similar results has been obtained when observed with the help of PSF.

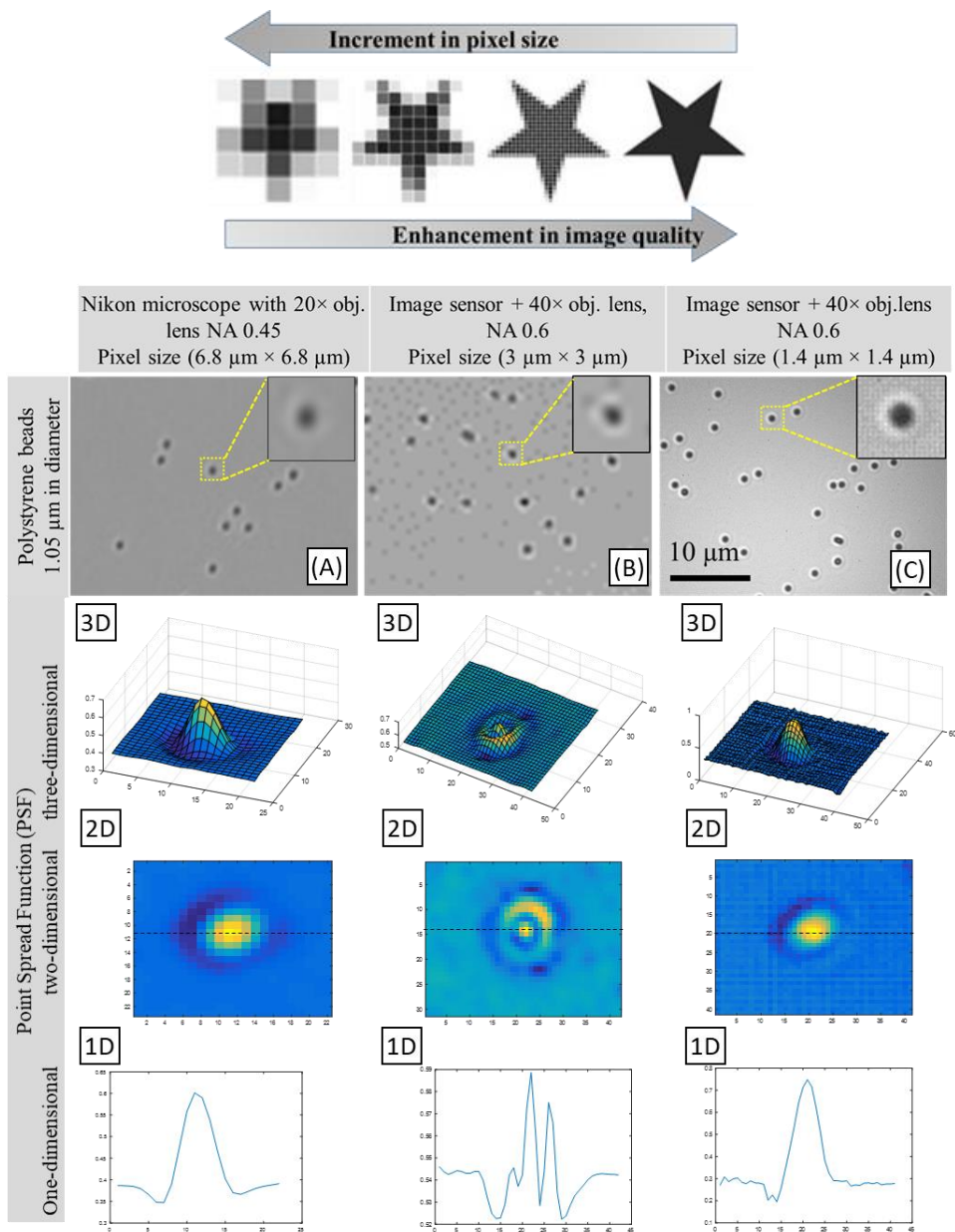


Fig. 3-9 Effect of pixel size and point spread function

3.4 Applications of portable transmitted microscope

3.4.1 Sub-micrometer scale imaging

Microscopic optical imaging at the sub micrometer scale requires a sophisticated expensive optical setup. Although the image resolution is limited by the diffraction limit of the light, optical imaging is cost-effective, fast, and convenient method compared to electron microscopy imaging. Further, we demonstrate the imaging of submicron sized spherical objects (PS beads), line pattern object (nanoscale grooves in polyethylene terephthalate film), and biological sample (monolayer grown bacteria). In order to obtain high resolution and quality of the image, the image sensor with the smallest pixel size (sensor '1', pixel size: $1.4\ \mu\text{m} \times 1.4\ \mu\text{m}$) was used with the $40\times$ objective lens (NA: 0.6).

Nano-meter sized polystyrene beads

PS beads with diameters of 920 nm, 460 nm, and 380 nm were observed by our setup (Fig. 3-10). In order to image the PS beads, beads were suspended in deionized water (DIW) and sandwiched between a glass slide (thickness 1 mm) and thin cover-glass (thickness 0.130 mm). Prior to the experiment, the shape and size of the beads were confirmed by SEM. As shown in Fig. 3-10, sharper images were obtained for the 920-nm and 460 nm beads. Moreover, it was possible to observe the 380-nm PS beads (smaller than the wavelength of

the light source) with a lower contrast than that of the 920 nm and 460 nm beads. In addition, the shape of the beads might be confirmed by our technique.

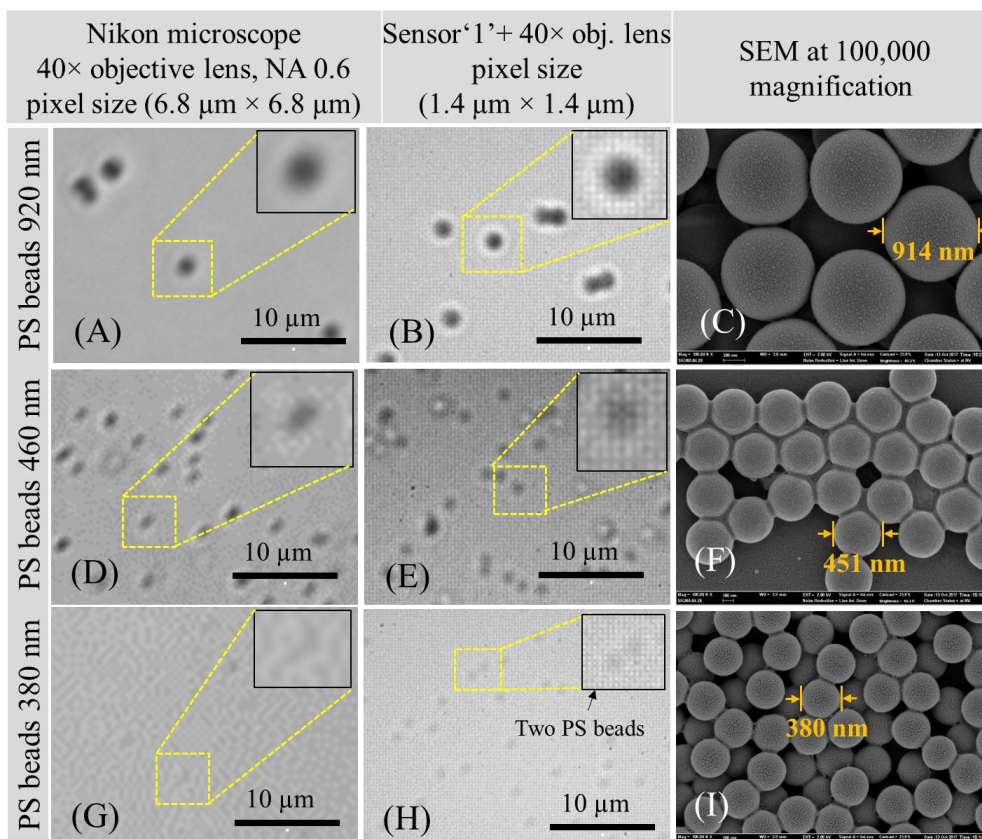


Fig. 3-10. Sub-micrometer scale imaging of polystyrene beads (920 nm, 460 nm and 380 nm) by portable microscope (A) Nikon microscope (objective lens 40× (NA 0.6)) (B) portable microscope; sensor '1' with the 40× objective lens (C) SEM at a magnification of 100,000. SEM imaging was used to confirm the size and shape of the beads. The shape and size information of the beads was possible to observe when imaged by our technique. Scale bar: 10μm

Nano-meter sized line pattern

Line patterns of sub micrometer grooves were observed (Fig. 3-11). The grooves were fabricated on a polyethylene terephthalate (PET) film using a silicon mold. The finger width and inter-finger spacing distance were 620 nm and 980 nm, respectively, confirmed by SEM (Fig. 3-11C). The elevated structures (fingers) were bright in the SEM image, while in the optical transmitted microscopy images they were dark, as the PET film was thick in this region. Similarly, the finger space was dark in the SEM images and bright in the optical transmitted microscopy images. The grooves were clearly distinguishable in the images obtained by our imaging setup. However, the edges are not very sharp owing to the limitation of the pixel size and diffraction of the light (wavelength: 460 nm) from the corners of the structure.

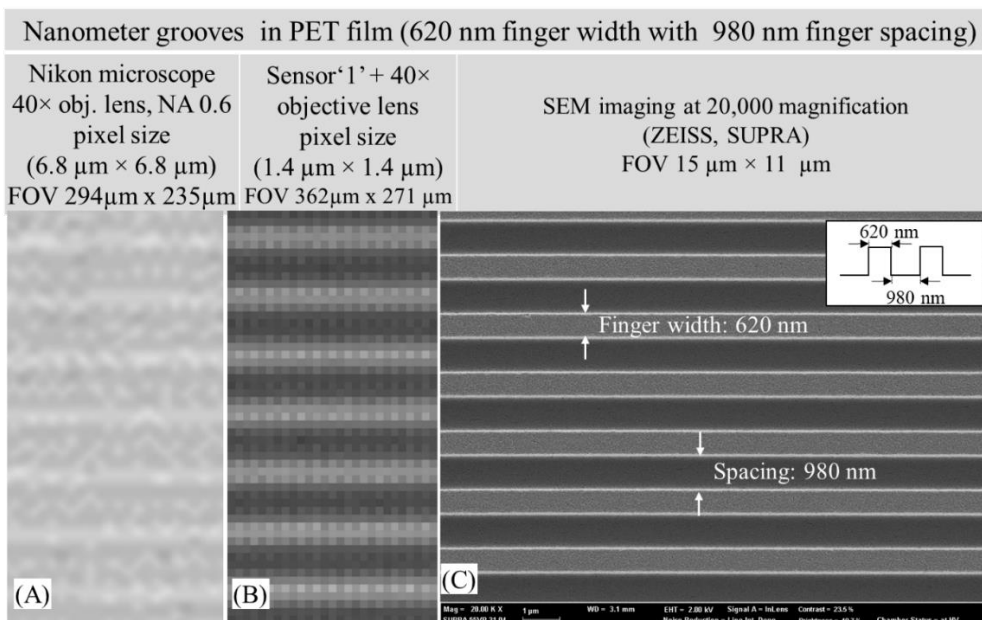


Fig. 3-11. Sub-micrometer scale imaging of nanoscale grooves on a PET film, performed by (A) Nikon microscope with 40× objective lens (NA 0.6) (B) sensor '1' with the 40× objective lens, and (C) SEM at a magnification of 20,000. The fingers (elevated parts) are imaged as dark in the optical microscopy images and light in the SEM images; the inter-finger space is imaged as light in the optical microscopy images and dark in the SEM images. Scale bar: 1 μm

Bacterial imaging

Further, an imaging of the 1-h-grown bacterial strain *E. coli* ATCC 25922 was performed and compared with that by the Nikon microscope as shown in Fig. 3-12. Bacterial strain *Escherichia coli* (*E. coli*) ATCC 25922 (KCTC, Korea) was grown in a monolayer form on 2.5% (w/v) low-gelling-temperature (LGT, Sigma-Aldrich USA) agarose in a 2.5% (w/v) Luria–Bertani (LB, Biosesang

Korea) medium at 37 °C for 1 h. For the monolayer bacterial growth, LB-rich melted LGT agarose was poured into a 3D-printed square chamber attached on a glass slide and closed by a clean cover glass. The agarose was allowed to cool for 30 min at room temperature in order to solidify. After the solidification, the cover glass was removed and 10 µl of the bacteria suspended in the LB medium were dropped on the agarose and dried. The chamber was sealed using a fresh cover glass and the sample was incubated for 1 h at 37 °C. Prior to use, the cover glass and glass slide were consecutively cleaned with 99% ethanol and distilled water (with each of them for 1 h) in a bath-type sonicator at 70 °C.

Since, *E. coli* ATCC 25922 divides at 20-min interval; a single bacterium should produce eight copies in 60 min through three successive divisions. The bacteria in each colony were distinguishable and countable when captured by our setup and Nikon microscope. However, the images of the bacterial colonies captured by the Nikon microscope had a better resolution. However, the cost-effectiveness and compactness of our device allows individual imaging setups to be used for observations of a particular bacterial strain. This could help restrict the possible interactions between different types of bacteria at the laboratory level.

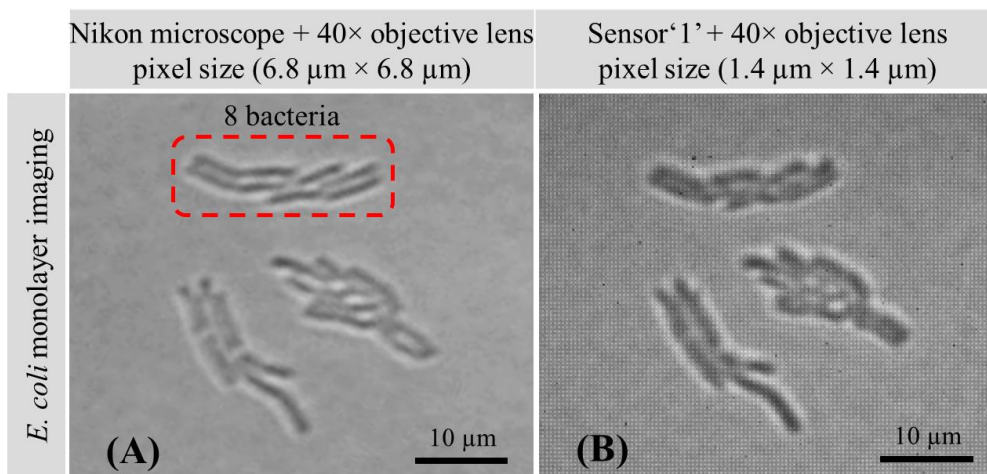


Fig. 3-12. Sub-micrometer scale imaging of monolayer bacterial colony grown for a hour by (A) Nikon microscope (B) sensor '1' with 40× objective lens. Scale bar: 10 μm.

3.4.2 High-speed microscopy: imaging of high-speed droplets generation

High-speed microscopy is an essential method for a better understanding of rapid physical phenomena at the micro- and nanoscale. A high-speed camera is used in bulky microscopes for a high-speed microscopy. In this study, we demonstrate the capability of our microscopic technique to observe fast-moving water droplets in a microfluidic channel.

Fabrication of PDMS microfluidic channel

Polydimethylsiloxane (PDMS, Sylgard 184 Dow Corning USA) microfluidic channel (height: 75 μm, width: 100 μm) was fabricated by a single-mask soft lithography process. A negative photoresist SU-8 (Microchem USA) was spin-coated on a 4-inch clean silicon wafer, followed by a standard lithography

process to pattern a mold. The degassed PDMS mixed at a ratio of 10:1 of monomer and curing agent was poured on the SU-8 mold wafer and cured at 70 °C for 2 h. Prior to the PDMS pouring, the SU-8 mold wafer was exposed to a silanizing agent (tridecafluoro-1,1,2,2-tetrahydrooctyl trichlorosilane) to aid the release of PDMS from the SU-8 mold wafer.

Droplet generation and high-speed microscopy

In order to generate water droplets in oil, the soybean oil (Sigma-Aldrich) flow rate was maintained either equal to or higher than that of the water. The droplet generation was monitored and recorded by the sensor '3' and sensor '4', as both sensors are suitable for a moderate-to-high-speed imaging. The objective lenses were selected according to the required FOV, image sensor size, and distance between the sensor and lens. The droplet generation was recorded at 20 frames/s and 2,252 frames/s by the sensor '3' and sensor '4', respectively (Fig. 3-13) (see supplementary video S1 and S2). It was possible to image the fast-moving droplets by placing the 40× objective lens directly at the high-speed camera sensor. Fig. 3-13C and Fig. 3-13D show the high-speed microscope setup without the light source, which was mounted on the objective lens. The proposed setup of high-speed microscopy is compact and portable, which makes it suitable for point-of-care devices. Moreover, the setup can be easily tuned for specific applications with desired FOV and resolution.

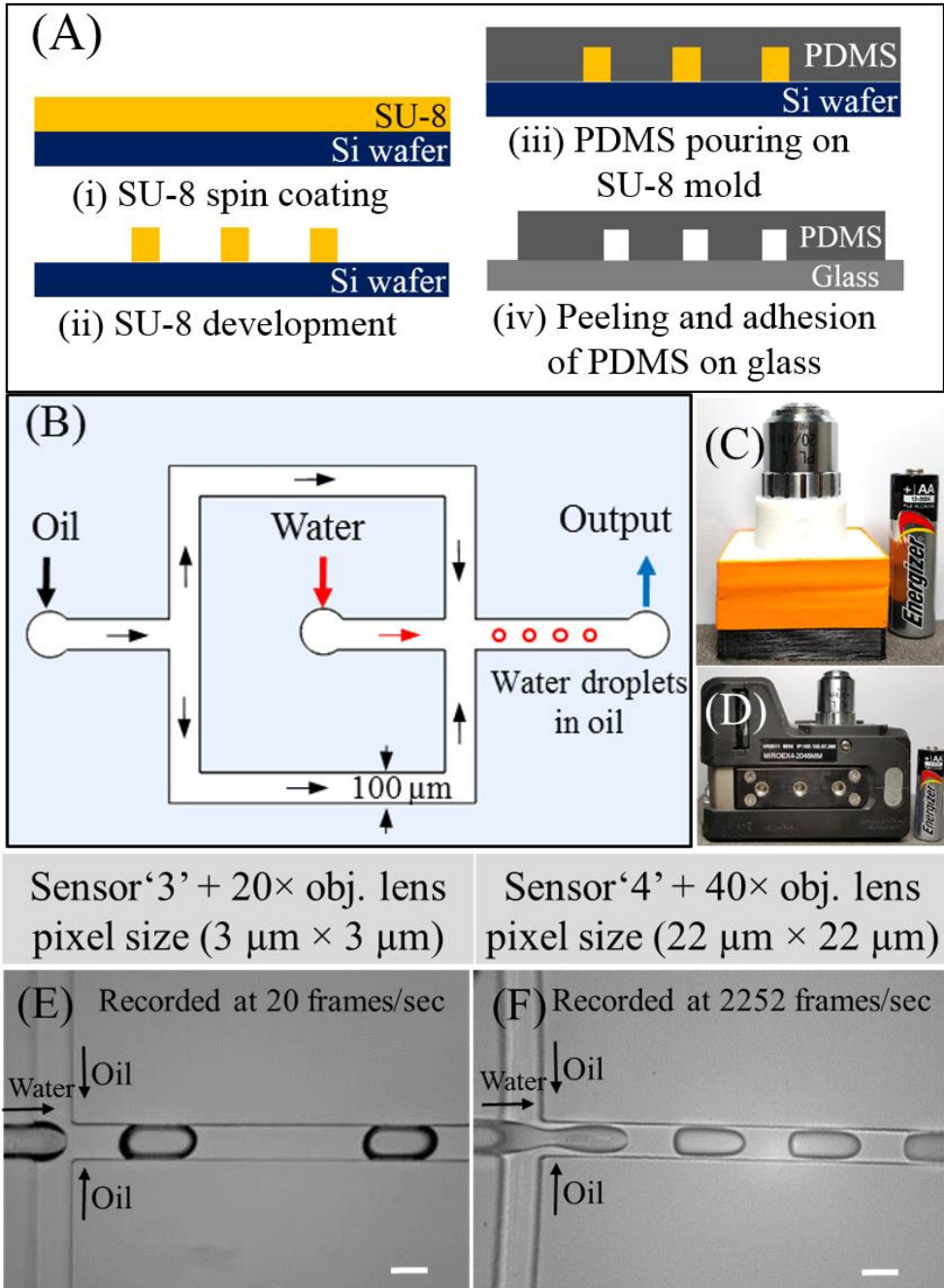


Fig. 3-13. High-speed microscopy. Microfluidic application: imaging of water droplet generation in oil. (A) Fabrication sequence for the PDMS microchannel. (B) Schematic of the oil flow, water flow, and water droplet generation in the

microchannel. Microscopic setups of the (C) sensor '3' with a 20× objective lens and (D) sensor '4' (high-speed camera) with a 40× objective lens (without the light source). Droplet observations by the (E) sensor '3' with a 20× objective lens at 20 frames/s, water flow rate of 0.25 $\mu\text{l}/\text{min}$, and soybean oil flow rate of 0.25 $\mu\text{l}/\text{min}$, Scale bar: 100 μm and (F) sensor '4' with a 40× objective lens, water flow rate of 1.5 $\mu\text{l}/\text{min}$, and soybean oil flow rate of 8.0 $\mu\text{l}/\text{min}$ at 2,252 frames/s. Scale bar: 100 μm .

3.4.3 Live imaging of eukaryotic cells

Owing to its small size and compactness, our imaging setup is suitable for a live cell imaging inside a large incubator. The large incubator provides a better environment compared to a small incubator used at the microscope stage for a live cell imaging. A live cell imaging of micrometer-sized NIH 3T3 fibroblast cells and zebrafish oocytes was performed as shown in Fig. 3-14.

Cell culture of NIH 3T3 fibroblast cells and zebrafish oocytes

NIH 3T3 fibroblast cells (KCLB Korea) were cultured in a Dulbecco's modified Eagle's medium (Thermo Scientific, USA) containing 10% fetal bovine serum (Thermo Scientific USA) and 3% penicillin–streptomycin (GIBCO, USA) at 37 °C and 5% CO₂ in a 1-mm-thick fibronectin-coated petri dish (\varnothing : 35 mm, SPL Life Science Korea) in an incubator (Thermo Fisher Scientific, USA) for 24 h prior to the imaging. Zebrafish oocytes were obtained by gently squeezing the belly of a mature female zebrafish (wild type). The obtained oocytes were dispersed in 1× *phosphate-buffered* saline in

a petri dish (\varnothing : 35 mm). The zebrafishes were purchased from a local fish dealer and maintained in 60-liter aquaria under a 14-h-light/10-h-dark condition at 28 °C.

Live cell imaging of NIH 3T3 fibroblast cells

A live cell imaging of micrometer-sized NIH 3T3 fibroblast cells was performed (Fig. 3-14C and 3-14 D). The sensor ‘2’ having a pixel size of 1.67 μm with 20 \times and 40 \times objective lenses were used to demonstrate a live cell imaging of NIH3T3 at low and high OMs. The complete imaging setup was placed inside an incubator (Thermoscientific USA); the data were recorded by a computer through a USB cable outside of the incubator. At a low OM, i.e., when the 20 \times objective lens was used, the FOV was 2,612 μm \times 1,868 μm . The cell morphology could be observed by magnifying the obtained image. At a high OM, i.e., when the 40 \times objective lens was used, the FOV was 1,195 μm \times 852 μm . Details of a single cell such as the nucleus and nucleus organelles could be observed.

Live cell imaging of zebrafish oocytes

The live cell imaging of the millimeter sized (in diameter) zebrafish oocytes was performed using the sensor ‘3’ inside a large incubator (Fig. 3-14E and Fig. 3-14F). As the zebrafish has a diameter of approximately 1 mm, the 20 \times objective lens was used. A FOV of 1,700 μm \times 1,275 μm was provided

by this combination. Further, the image quality of our setup was compared with that obtained by the Nikon microscope, as shown in Fig. 3-14E–F. Although the peripheral area of the image captured by our setup was less sharp, compared with the Nikon microscope image, the progress of the oocyte development could be tracked by our imaging setup.

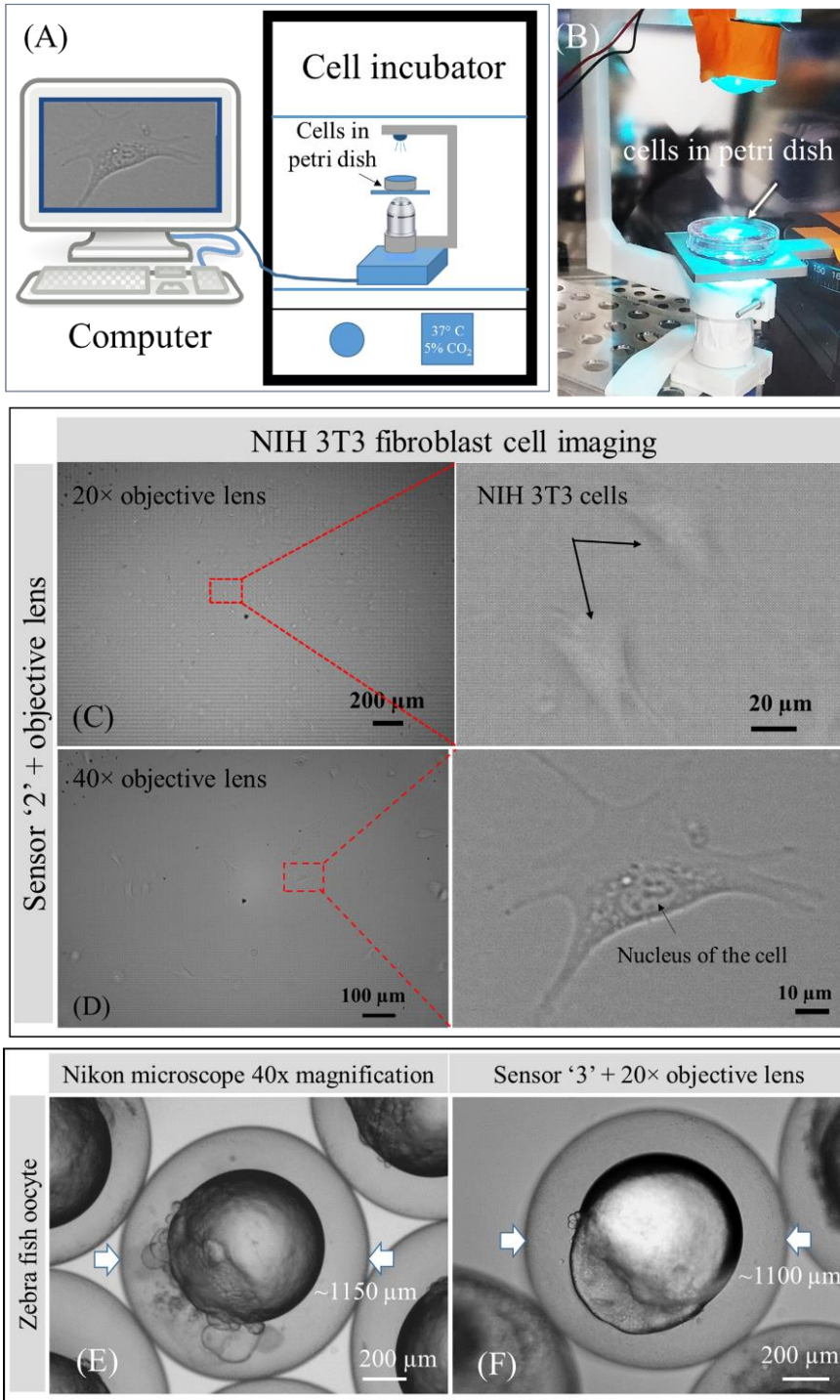


Fig. 3-14. Live cell imaging by portable microscope inside the incubator. (A) Schematic of the imaging setup. (B) Imaging setup inside the incubator. Live cell

imaging of microscale NIH3T3 cells by the (C) sensor '2' with a 20× objective lens, FOV: 2,612 μm \times 1,868 μm , and (D) sensor '2' with a 40× objective lens, FOV: 1,195 μm \times 852 μm . Live cell imaging of millimeter-sized zebrafish oocytes by the (E) Nikon microscope, FOV: 2,500 μm \times 1,875 μm and (F) sensor '3' with a 20× objective lens, FOV: 1,700 μm \times 1,275 μm .

3.4.4 Industrial applications: high-resolution real-time monitoring of a sample at a bulky apparatus

Microscopic monitoring of a sample at a bulky apparatus in an industrial environment is a challenging task. As our microscope is compact and portable, it is possible to install it at a bulky apparatus and monitor the physical changes of a sample at the microscale in real time. Crack propagations in the rGO-PDMS membrane, stretched by the MTS machine, were recorded by the image sensor '3' with the 20× objective lens (Fig. 3-15 and Fig. 3-16).

A submicrometer-thick reduced-graphene-oxide (rGO) film was coated on a 0.8-mm-thick PDMS by the drop-casting method (rGO-PDMS) (Saha, Baek et al. 2017). An rGO-PDMS sample with a length, width, and thickness of 35, 7, and 0.8 mm, respectively, was anchored in a material testing system (MTS) machine (MTS Criterion, model 4, USA) (refer Fig. 3-15). The sample was stretched up to 10% of the initial sample length, i.e., up to 3.5 mm. The crack propagation was observed by sensor '3' with a 20× objective lens having a FOV of 1552 μm \times 1164 μm . A quantitative analysis of the crack propagation was performed by processing the images in 'ImageJ' software.

A quantitative analysis of the crack formation was performed by analyzing the sample images recorded at 0.5-mm stretching intervals up to the total stretching length of 3.5 mm (10% of the initial length of 35 mm) as shown in Fig 3-16. Owing to the MTS and surrounding vibration, the total area of the cracks increased with the stretching of the sample. The total area of the cracks was 11.35% of the total area of the sample at the final stage.

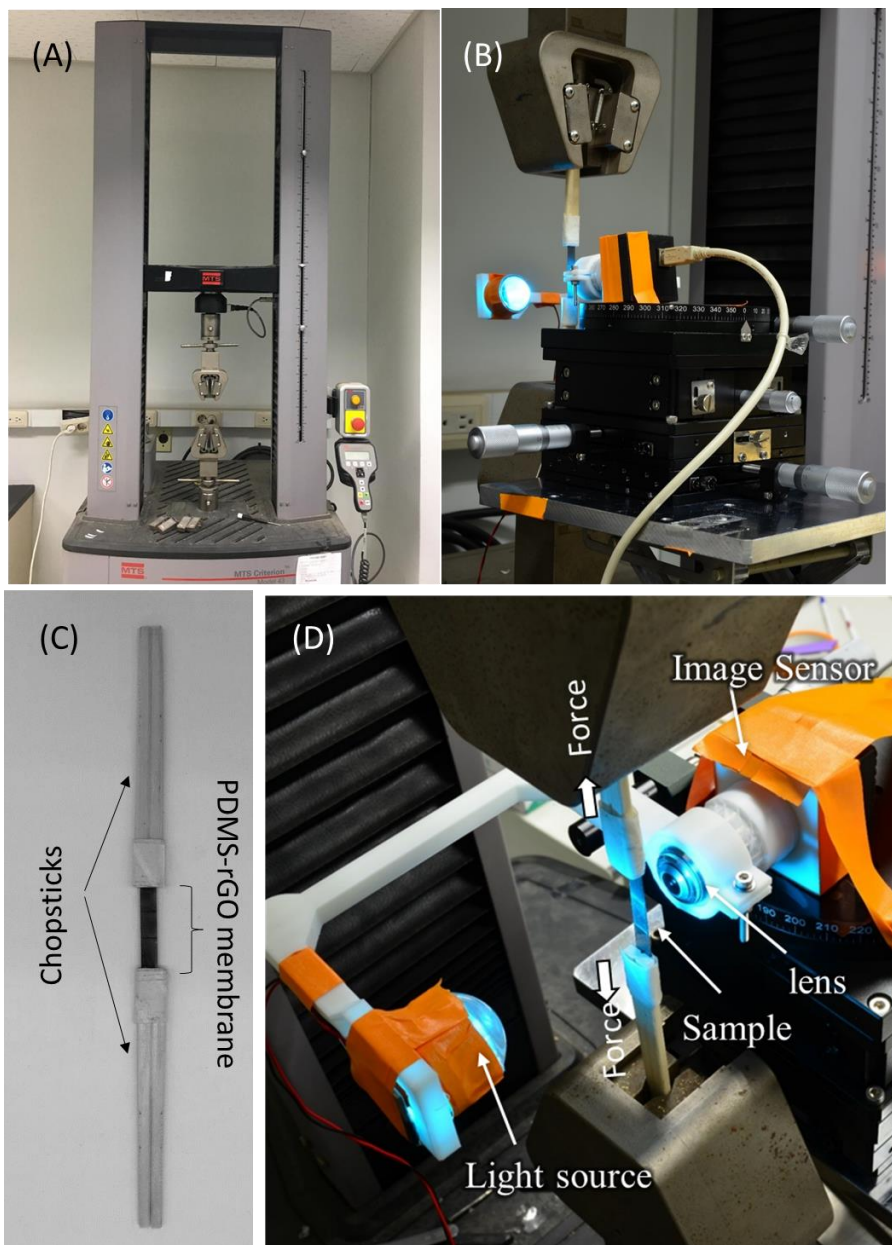


Fig. 3-15. Imaging of crack propagation in a sample on bulky apparatus by portable microscope. (A) Material testing system (MTS) machine (MTS Criterion, model 4, USA) (B) sample attached to MTS machine (C) Sample: rGO-PDMS membrane attached on chopsticks (D) Experimental setup: direct imaging of the crack propagation in the rGO film by stretching with the MTS machine. Light source wavelength 460 nm

(A) Increment in crack area due to elongation of a sample

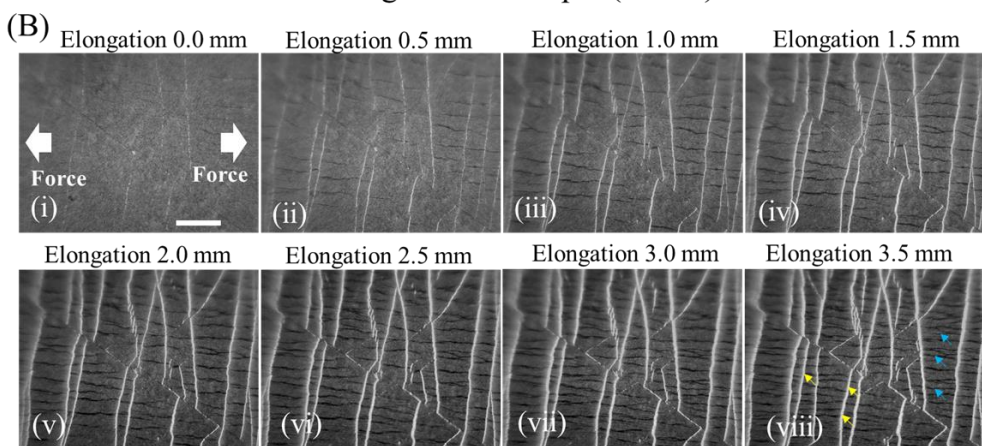
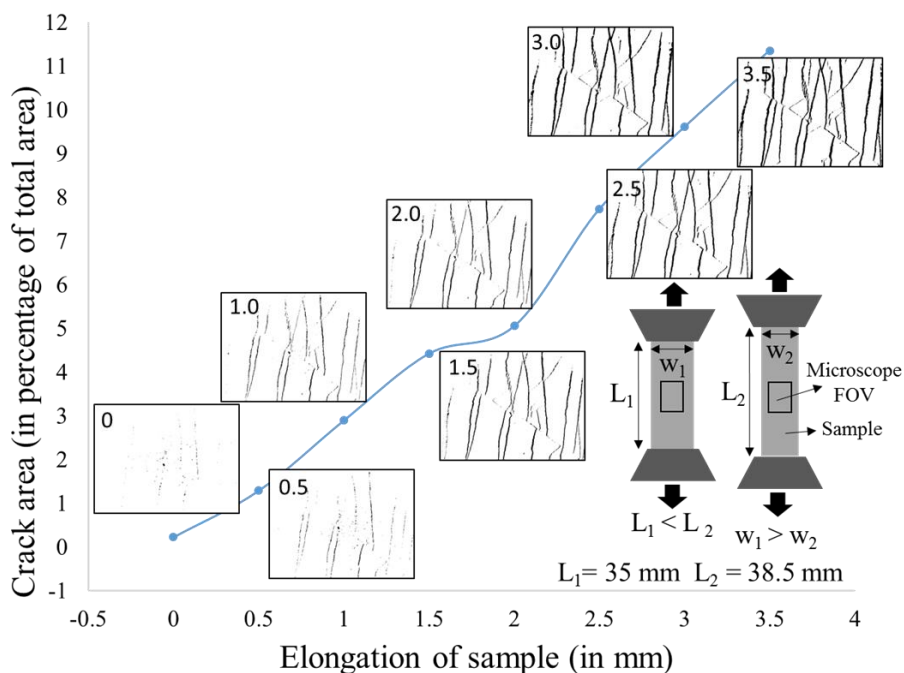


Fig. 3-16. Crack propagation analysis in the rGO film attached on PDMS. (A) Observation of the crack propagation (white) and compression (black) in the rGO thin film during the stretching at intervals of 0.5 mm. The yellow and blue arrows in Fig. 3-16B.viii indicate the cracks and folding of the rGO thin films on PDMS, respectively. Scale bar: 500 μm (B) Quantitative analysis of the crack propagation

after the image processing. The ratio between the total areas of the cracks and sample increased with the stretching of the sample in the length direction.

3.4.5 Industrial applications: optical inspection of micropatterns fabricated in a clean room

A visual inspection of two fabricated patterns was performed using our microscopic technique and compared with the images obtained by the high-performance Nikon microscope (Fig. 3-17). The edges of the two samples, over-etched indium tin oxide (ITO) on a glass wafer with PR AZ5214 as a mask and PDMS microchannel fabricated using the SU-8 mold on a silicon wafer, were studied. The edges of the first sample were observed by the sensor '2' with the 40× objective lens to demonstrate a large-FOV ($1,195 \mu\text{m} \times 852 \mu\text{m}$) inspection without losing the detailed information, compared to the small FOV ($294 \mu\text{m} \times 235 \mu\text{m}$) provided by the Nikon microscope. A close inspection of the side walls of the second sample at a high resolution was performed using the sensor '1' with the 40× objective lens, as the sensor '1' has pixels with a small size ($1.4 \mu\text{m} \times 1.4 \mu\text{m}$). As shown in Fig. 3-17A and Fig. 3-17B, our microscopic setup provides an approximately 14 times larger FOV, compared to that of the Nikon microscope; however, the image quality of the cracks on the edges are comparable. Therefore, an inspection at a large area can be achieved using our setup. In PDMS microchannel sample, the slope of the PDMS vertical walls is visualized (Fig. 3-17C and Fig. 3-17D).

Our technique provided the comparable quality of the image as that of the Nikon microscopy. Therefore, our microscopic technique is suitable for an optical inspection of samples, in particular, during a microfabrication process in a clean room.

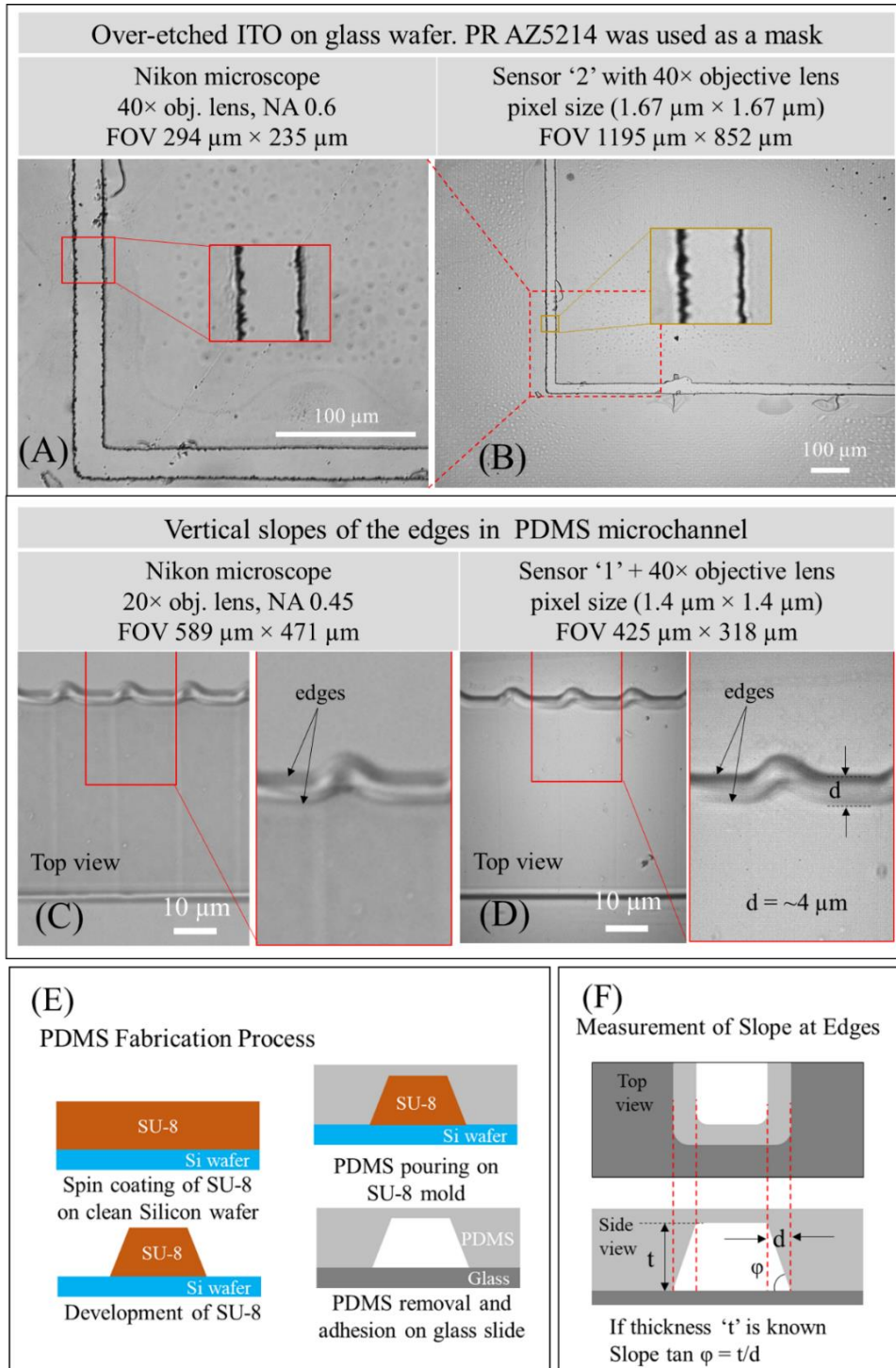


Fig. 3-17. Optical inspection of fabricated micro-patterns and slope measurement at edge by a portable microscope. Inspection of edges of the over-etched ITO on a glass

wafer with PR AZ5214 as a mask by the (A) Nikon microscope, and (B) sensor '2' with the 40× objective lens. Inspection of slopes at edges in the PDMS microfluidic channel by the (C) Nikon microscope, and (D) sensor '1' with the 40× objective lens. (E) PDMS fabrication process (F) measurement of slope at edges

Bibliography

Akin, D., H. Li and R. Bashir (2004). "Real-Time Virus Trapping and Fluorescent Imaging in Microfluidic Devices." Nano Letters **4**(2): 257-259.

Bogoch, I. I., H. C. Koydemir, D. Tseng, R. K. D. Ephraim, E. Duah, J. Tee, J. R. Andrews and A. Ozcan (2017). "Evaluation of a Mobile Phone-Based Microscope for Screening of Schistosoma haematobium Infection in Rural Ghana." The American journal of tropical medicine and hygiene **96**(6): 1468-1471.

Cai, J. F., J. Hui, L. Chaoqiang and Z. Shen (2009). Blind motion deblurring from a single image using sparse approximation. 2009 IEEE Conference on Computer Vision and Pattern Recognition.

Cybulski, J. S., J. Clements and M. Prakash (2014). "Foldscope: Origami-Based Paper Microscope." PLOS ONE **9**(6): e98781.

Dong, S., K. Guo, P. Nanda, R. Shiradkar and G. Zheng (2014). "FPscope: a field-portable high-resolution microscope using a cellphone lens." Biomedical Optics Express **5**(10): 3305-3310.

Fergus, R., B. Singh, A. Hertzmann, S. T. Roweis and W. T. Freeman (2006). Removing camera shake from a single photograph. ACM SIGGRAPH 2006 Papers. Boston, Massachusetts, ACM: 787-794.

Gabor, D. (1948). "A New Microscopic Principle." Nature **161**: 777.

Greenbaum, A., W. Luo, T.-W. Su, Z. Göröcs, L. Xue, S. O. Isikman, A. F. Coskun, O. Mudanyali and A. Ozcan (2012). "Imaging without lenses: achievements and remaining challenges of wide-field on-chip microscopy." Nature methods **9**(9): 889-895.

Heng, X., D. Erickson, L. R. Baugh, Z. Yaqoob, P. W. Sternberg, D. Psaltis and C. Yang (2006). "Optofluidic microscopy—a method for implementing a high resolution optical microscope on a chip." Lab on a Chip **6**(10): 1274-1276.

Kanka, M., R. Riesenberger, P. Petrucek and C. Graulig (2011). "High resolution (NA=0.8) in lensless in-line holographic microscopy with glass sample carriers." Optics Letters **36**(18): 3651-3653.

Kim, S. B., H. Bae, K.-i. Koo, M. R. Dokmeci, A. Ozcan and A. Khademhosseini (2012). "Lens-Free Imaging for Biological Applications." Journal of laboratory automation **17**(1): 43-49.

Lai, W. S., J. B. Huang, Z. Hu, N. Ahuja and M. H. Yang (2016). A Comparative Study for Single Image Blind Deblurring. 2016 IEEE Conference on Computer Vision and Pattern Recognition (CVPR).

Levin, A. (2006). Blind motion deblurring using image statistics. Proceedings of the 19th International Conference on Neural Information Processing Systems. Canada, MIT Press: 841-848.

Saha, B., S. Baek and J. Lee (2017). "Highly Sensitive Bendable and Foldable Paper Sensors Based on Reduced Graphene Oxide." ACS Applied Materials & Interfaces **9**(5): 4658-4666.

Thorn, K. (2016). "A quick guide to light microscopy in cell biology." Molecular Biology of the Cell **27**(2): 219-222.

Wang, W. and F. Chang (2011). "A Multi-focus Image Fusion Method Based on Laplacian Pyramid." Journal of Computers **6**(12): 2559-2566.

Xu, W., M. H. Jericho, I. A. Meinertzhagen and H. J. Kreuzer (2001). "Digital in-line holography for biological applications." Proceedings of the National Academy of Sciences **98**(20): 11301.

Yongpan, W., F. Huajun, X. Zhihai, L. Qi and D. Chaoyue (2010). "An improved Richardson–Lucy algorithm based on local prior." Optics & Laser Technology **42**(5): 845-849.

Zhang, H., D. Wipf and Y. Zhang (2013). Multi-image Blind Deblurring Using a Coupled Adaptive Sparse Prior. 2013 IEEE Conference on Computer Vision and Pattern Recognition.

Zheng, G., S. A. Lee, Y. Antebi, M. B. Elowitz and C. Yang (2011). "The ePetri dish, an on-chip cell imaging platform based on subpixel perspective sweeping microscopy (SPSM)." Proceedings of the National Academy of Sciences of the United States of America **108**(41): 16889-16894.

Chapter 4

Conclusion

In this study, we report a technique for novel compact portable cost-effective customizable submicron-resolution inverted (transmitted) and reflected optical microscopes. Our technique utilizes the proximity of the image sensor (high-resolution) to a commercial microscope objective lens and does not use tube lens. Removal of tube lens in both type of microscopes brings down the size, weight, optical components and cost of the microscope. Moreover, the reduction of optical components reduces the optical attenuation of light reaching to the image sensor, which results in to a bright and contrast image of an object. Further, our microscopic imaging technique is capable of imaging objects with sizes in the range of submicrometer to millimeter with a high resolution. Owing to its compactness, our microscope is suitable for a real-time monitoring of an object inside a controlled environment chamber such as live cell imaging inside cell culture incubator. Further, the microscopic setup can be customized for a specific application. It has a potential to be developed as a portable point-of-care device. The capability of submicron-level imaging, portability, and adaptability, make it promising for industrial applications where standard microscopes have limitations.

In addition, our reflected microscope having upward facing objective lens allows in-situ real-time field imaging and monitoring of abaxial stomatal opening under natural conditions without any physical or chemical manipulation of a leaf. Results establishes a direct relationship between the intensity of sunlight falling on the leaf and the area of the stomatal opening. Area of the stomatal opening increases with the increment in the sunlight intensity until maximum opening reaches and vice versa in well-watered plant. However, the age of leaf, location of the leaf, wind velocity, ambient temperature and other environmental factors may affect the concluded trend between stomatal opening area and intensity of sunlight at the leaf surface. In addition, stomatal density, changes in geometrical features of stomatal aperture (aspect ratio, circularity), changes in porosity of a leaf area as per intensity of sunlight has been quantified. Submicron meter spatial resolution (488 nm) along with the small depth of view ($\sim 1.3 \mu\text{m}$) provided by our portable microscope enabled us to observe the stomatal pores of a non-planar leaf surface from it early opening until the maximum possible opening even in presence of high-density hair like structures. Use of novel leaf holder allowed us to perform long-term monitoring of stomata closely to its natural conditions. Further, a stomatal imaging of plant leaves exposing to the different intensity of sunlight at a time provided the mapping of plant porosity (total area of stomatal opening/ leaf area) which changes continuously

throughout of the day according to the geographical location of the place in different weathers. We believe to be the first to demonstrate the real-time stomatal dynamics in intact plant leaf at the field. In future, field monitoring of stomata behavior considering other environmental factors and conditions will further increase our understanding of the plant parameter(s) connected with stomata dynamics.

Further, the use of a high magnification objective lens and small-wavelength (monochromatic) light source could improve the resolution of the current setup. Recently, the development of a highly curved image sensor demonstrated its significant optical and size benefits in camera applications (Rim, Catrysse et al. 2008, Guenter, Joshi et al. 2017). The use of a high-resolution curved image sensor in our technique can improve the illumination uniformity, resolution, light gathering, and focusing in a large FOV, while reducing the system size, cost, and complexity.

Table 4-1 Comparison of stomatal pore imaging and/or monitoring techniques

Methods to monitor the stomatal opening	Method type	Manipulation of a leaf	Real-time monitoring	Long-term monitoring	In-field imaging	Direct measurement of stomatal pore dynamics	Accuracy
Mold Impression method	Direct method	Physical & Chemical	×	×	×	×	Less accurate
Fluorimetric measurement of stomatal activity	Direct method	Chemical	○	○	×	○	Less accurate
Porometer	Indirect method	Not required	○	×	○	×	Less accurate
Electro-mechanical sensor	Indirect method	Physical & Chemical	○	○	Only for movable plants	×	Not possible
Infrared-thermography	Indirect	Not required	○	○	○	×	Less accurate
Portable microscope based method	Direct method	Not required	○	○	○	○	Highly accurate

‘○’ possible
‘×’ not possible

Table 4-2 Comparison of portable inverted microscope

Methods	Microscopic technique	Resolution	Image reconstruction	Cost	Field of view Compared to the standard microscope	Sample type
Lens-free imaging	Digital in-line holography microscopy	400-500 nm	Required	High	Depend upon the sensor size	Microscope slide (stationary)
Lens-free imaging	Contact lens-free imaging microscopy	400-500 nm	Required	Low	Depend upon the sensor size	Microscope slide (stationary)
Lens-free imaging	Optofluidic microscopy	490 nm	Required	High	Depend upon the fabrication	Movable sample
Lens-based imaging	Smartphone-based-microscope	870 nm	Required	Low	Moderate	Microscope slide (stationary and movable)
Lens-based imaging	Foldscope	1380 nm	Not required	Very low	Low	Microscope slide
Lens-based imaging	Our method	488 nm	Not Required	Low	Moderate	All samples

Bibliography

Guenter, B., N. Joshi, R. Stoakley, A. Keefe, K. Geary, R. Freeman, J. Hundley, P. Patterson, D. Hammon, G. Herrera, E. Sherman, A. Nowak, R. Schubert, P. Brewer, L. Yang, R. Mott and G. McKnight (2017). "Highly curved image sensors: a practical approach for improved optical performance." Optics Express **25**(12): 13010-13023.

Rim, S.-B., P. B. Catrysse, R. Dinyari, K. Huang and P. Peumans (2008). "The optical advantages of curved focal plane arrays." Optics Express **16**(7): 4965-4971.